LBNL-40364
UC-364

ERNEST ORLANDO LAWRENCE BERKELEY NATIONAL LABORATORY

Energy Coupling and Plume Dynamics During High Power Laser Heating of Metals

Sungho Jeong

Environmental Energy Technologies Division

May 1997

Ph.D. Thesis

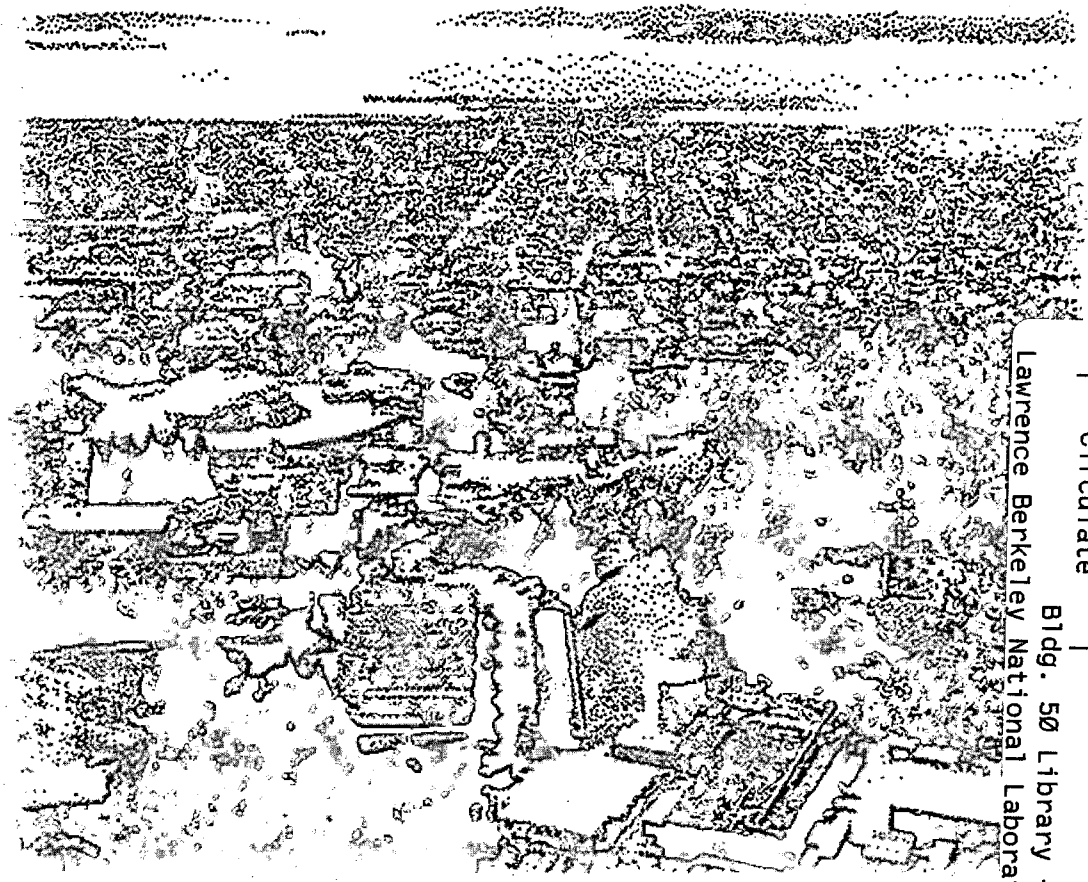

REFERENCE COPY
Does Not
Circulate
Bldg. 50 Library - Ref.
Lawrence Berkeley National Laboratory
Copy 1
LBNL-40364

DISCLAIMER

This document was prepared as an account of work sponsored by the United States Government. While this document is believed to contain correct information, neither the United States Government nor any agency thereof, nor the Regents of the University of California, nor any of their employees, makes any warranty, express or implied, or assumes any legal responsibility for the accuracy, completeness, or usefulness of any information, apparatus, product, or process disclosed, or represents that its use would not infringe privately owned rights. Reference herein to any specific commercial product, process, or service by its trade name, trademark, manufacturer, or otherwise, does not necessarily constitute or imply its endorsement, recommendation, or favoring by the United States Government or any agency thereof, or the Regents of the University of California. The views and opinions of authors expressed herein do not necessarily state or reflect those of the United States Government or any agency thereof or the Regents of the University of California.

LBNL-40364
UC-364

ENERGY COUPLING AND PLUME DYNAMICS DURING HIGH POWER LASER HEATING OF METALS

by

Sungho Jeong

Ph.D. Thesis

Department of Mechanical Engineering
University of California

and

Environmental Energy Technologies Division
Lawrence Berkeley National Laboratory
Berkeley, California 94720

May 1997

This work was supported by the Office of Basic Energy Sciences, Chemical Sciences Division, Processes and Techniques Branch of the U.S. Department of Energy under Contract No. DE-AC03-76SF00098.

Energy Coupling and Plume Dynamics During High Power Laser Heating of Metals

Copyright © 1997

by

Sungho Jeong

The U.S. Department of Energy has the right to use this document
for any purpose whatsoever including the right to reproduce
all or any part thereof

Abstract

Energy Coupling and Plume Dynamics during High Power Laser Heating of Metals

by

Sungho Jeong

Doctor of Philosophy in Mechanical Engineering

University of California, Berkeley

Professor Ralph Greif, Chair

High power laser heating of metals was studied utilizing experimental and numerical methods with an emphasis on the laser energy coupling with a target and on the dynamics of the laser generated vapor flow. Rigorous theoretical modeling of the heating, melting, and evaporation of metals due to laser radiation with a power density below the plasma shielding threshold was carried out. Experimentally, the probe beam deflection technique was utilized to measure the propagation of a laser induced shock wave.

The effects of a cylindrical cavity in a metal surface on the laser energy coupling with a solid were investigated utilizing photothermal deflection measurements. A numerical calculation of target temperature and photothermal deflection was performed to compare with the measured results. Reflection of the heating laser beam inside the cavity

was found to increase the photothermal deflection amplitude significantly and to enhance the overall energy coupling between a heating laser beam and a solid.

Next, unsteady vaporization of metals due to nanosecond pulsed laser heating with an ambient gas at finite pressure was analyzed with a one dimensional thermal evaporation model for target heating and one dimensional compressible flow equations for inviscid fluid for the vapor flow. Target surface conditions, vapor velocity at the Knudsen layer, and the gasdynamic flow characteristics of the vapor were investigated.

Lastly, the propagation of a shock wave during excimer laser heating of aluminum was measured with the probe beam deflection technique. The transit time of the shock wave was measured at the elevation of the probe beam above the target surface; these results were compared with the predicted behavior using ideal blast wave theory. The experimental conditions at which the propagation of the laser generated shock wave agrees with the prediction from ideal blast wave theory were obtained. The propagation of a gaseous material plume was also observed from the deflection of the probe beam at later times.

Ralph Greif

Chairman, Dissertation committee

To My Family

Table of Contents

DEDICATION iii

TABLE OF CONTENTS v

LIST OF FIGURES viii

LIST OF TABLES xv

ACKNOWLEDGMENTS xvi

1. INTRODUCTION 1

1.1 Laser ablation technology: overview 1

1.2 Scope of the present study 6

References 9

2. LASER HEATING OF A CAVITY VERSUS A PLANE SURFACE FOR METAL TARGETS: A STUDY OF ENERGY COUPLING 15

2.1 Introduction 15

2.2 Experimental system 17

2.3 Numerical modeling 21

2.4 Results and discussion 26

2.4.1 Experimental results 26

2.4.2 Numerical results 29

2.4.3 Discussion 34

2.5 Conclusion 40

References 40

3. NUMERICAL ANALYSIS OF THE PULSED LASER HEATING OF METALS 44

3.1 Introduction 44

3.2 Theoretical modeling 49

3.2.1 Solid heating 49

3.2.2 Gasdynamics of the vapor 53

3.3 Numerical Methods 54

3.3.1 Solid heating 54

3.3.2 Gasdynamics of the vapor 55

3.4 Results and discussion 58

3.5 Conclusion 89

References 90

4. MEASUREMENT OF THE PROPAGATION OF THE LASER INDUCED SHOCK WAVE AND MATERIAL PLUME UTILIZING THE PROBE BEAM DEFLECTION TECHNIQUE 97

4.1 Introduction 97

4.2 Experimental system 103

4.3 Blast wave theory 107

4.4 Results and discussion 109

4.4.1 Deflection of the probe beam for the early period ($0<t<10$ μs) 109

4.4.2 Deflection of the probe beam for the period $t>10$ μs 146

4.4.3 Target surface morphology 154

4.5 Conclusion 159

References 161

5. CONCLUSIONS AND DISCUSSION 167

APPENDIX 171

List of Figures

CHAPTER 2

Fig. 2.1 Schematic diagram of the experimental system

Fig. 2.2 Positioning of the probe beam for measurements of photothermal deflection (a) for cavity heating and (b) for plane surface heating

Fig. 2.3 Photothermal deflection amplitudes for a cavity heating and a plane surface heating for (a) copper, (b) lead, and (c) stainless steel (circle: cavity, square: plane surface)

Fig. 2.4 Photothermal deflection amplitudes from heating a cavity of aspect ratio of 0.89 and a plane surface for lead (circle: cavity, square: plane surface)

Fig. 2.5 Temperature distributions in the target and in the surrounding air for copper at $\tau=0.7\tau_0$ for (a) cavity heating and for (b) plane surface heating

Fig. 2.6 Temperature distributions in the target and in the surrounding air for lead at $\tau=0.7\tau_0$ for (a) cavity heating and for (b) plane surface heating

Fig. 2.7 Temperature distributions in the target and in the surrounding air for stainless steel at $\tau=0.7\tau_0$ for (a) cavity heating and for (b) plane surface heating

Fig. 2.8 Computed photothermal deflections for cavity heating and for plane surface heating for (a) copper, (b) lead, and (c) stainless steel ($z_0'=2.17$, solid line: for a cavity, dotted line: for a plane surface)

Fig. 2.9 Temperature distributions in the target and in the surrounding air for copper at $\tau=0.7\tau_0$ (a) with and (b) without the absorption of the reflected laser energy on the cavity wall

Fig. 2.10 Computed photothermal deflections for (a) copper, (b) lead, and (c) stainless steel when reflection of the heating laser beam is included ($z_0'=2.17$, solid line: for a cavity including reflection, dashed line: for a cavity without reflection, dotted line: for a plane surface)

CHAPTER 3

Fig. 3.1 Schematic diagram of the laser induced evaporation

Fig. 3.2 Schematic diagram of the solution of a Riemann problem ($p_l > p_r$ in this figure).

Fig. 3.3 Variation of the threshold laser fluence for evaporation with respect to the reflectivity of the (aluminum) target surface.

Fig. 3.4 Variation of the total momentum of the vapor leaving the Knudsen layer, $\boldsymbol{M}$ in Eq. (3.21), with respect to the Mach number of the vapor at the edge of the Knudsen layer, M_1. (Normalized by the saturation pressure of the vapor at the target surface)

Fig. 3.5 Variation of the maximum Mach number of the vapor at the edge of the Knudsen layer for different ambient pressures (vaporization started at t=10.72 ns; F=7.5 J/cm^2)

Fig. 3.6 (a) Density profiles in the gasdynamic regime near the edge of the Knudsen layer during the early period of evaporation (vaporization started at t=10.72 ns; p_b=0.4 atm, F=7.5 J/cm^2)

(b) Density profiles in the gasdynamic regime near the edge of the Knudsen layer during the early period of evaporation (vaporization started at t=10.72 ns; p_b=0.4 atm, F=7.5 J/cm^2) (continued)

Fig. 3.7 Variation of the maximum Mach number of the vapor and pressure during the early period of evaporation (vaporization started at t=10.72 ns; p_b=0.4 atm, F=7.5 J/cm^2)

Fig. 3.8 Delay times for $M_{1,max}$ to become unity and for the contact surface to appear in the gasdynamic regime with respect to the ambient pressure (circle: $M_{1,max}$, square: contact surface; F=7.5 J/cm^2)

Fig. 3.9 Maximum ambient pressure allowed for $M_{1,max}$ to be equal to unity from the beginning of the evaporation

Fig. 3.10 Variation of $M_{1,max}$ with time at different laser fluence. For F=6.5 J/cm^2 $M_{1,max}$ does not become unity during the evaporation.

Fig. 3.11 (a) Temporal variation of the target surface temperature and (b) the maximum values for different laser fluences

(c) Temporal variation of the saturation pressure at the target surface and (d) the maximum values for different laser fluences

(e) Temporal variation of the liquid-vapor interface velocity at the target surface and (f) the maximum values for different laser fluences

Fig. 3.12 Ablation depth for a single laser pulse with respect to the laser fluence

Fig. 3.13 Temperature distribution in the target with time (F=7 J/cm^2)

Fig. 3.14 (a) Temporal variation of the vapor velocity at the edge of the Knudsen layer and (b) the maximum values for different laser fluences

Fig. 3.15 (a) Distribution of density in the gasdynamic flow with time (F=7 J/cm^2, p_b=0.01 atm, vaporization started at t=11.68 ns and ceased at t=26.42 ns. Each region and the discontinuities are explained in the context.)

(b) Distribution of velocity in the gasdynamic flow with time (F=7 J/cm^2, p_b=0.01 atm, vaporization started at t=11.68 ns and ceased at t=26.42 ns. The maximum vapor velocity at the Knudsen layer is 1055 m/s.)

Fig. 3.16 Propagation of the shock wave (solid line) and the contact surface (dotted line) (F=7 J/cm^2, p_b=0.01 atm)

CHAPTER 4

Fig. 4.1 Schematic diagram of the laser induced gasdynamic flow and the deflection of the probe beam

Fig. 4.2 Schematic diagram of the experimental system

Fig. 4.3 A typical temporal profile of the excimer laser pulse

Fig. 4.4 Deflection time-response profiles measured in air for different normal offsets of the probe beam (E_p=7 mJ, P_p=2.0 x10^7 W/cm^2)

Fig. 4.5 Schematic diagram for the deflection of a single ray of light due to an ideal spherical blast wave

Fig. 4.6 Density distribution behind the shock for an intense spherical blast wave obtained by Sedov's similarity method [42] (γ=1.4)

Fig. 4.7 Computed deflection of a Gaussian beam due to an ideal spherical blast wave. Self-similar solution by Sedov [42] is used to calculate the density distribution.

Fig. 4.8 Computed deflection of a Gaussian beam with time. The results in Fig. 4.7 are reformed using Eq. (4.15) with E_0^*=5 mJ

Fig. 4.9 Computed deflection when the density decrease behind the shock wave is omitted

Fig. 4.10 Time-of-propagation, Δt_1, of the shock wave for measured deflection signals (the curves for Z_0=0.51 and 1.27 mm in Fig. 4.4 are reshown)

Fig. 4.11 Time-of-propagation of the shock wave with respect to the pulse energy of the heating laser (Z_0=2 mm)

Fig. 4.12 Time-of-propagation with respect to ambient pressure (E_p=10 mJ, Z_0=2 mm)

Fig. 4.13 Deflection time-response profiles at reduced ambient pressure for different values of Z_0 (p_∞=300 Torr, E_p=7 mJ, P_p=2.0x10^7 W/cm^2)

Fig. 4.14 Time-of-propagation of the shock wave for different ambient pressures, 300 and 760 torr. The velocity of the shock wave is computed from the derivative of the closest polynomial fit (Δt_1=a$_1x$+a$_2x^2$) to the time-of-propagation data. (circle: 760 Torr, square: 300 Torr)

Fig. 4.15 (a) Comparison of the time-of-propagation data for p_∞=300 Torr in Fig. 4.14 with the relationship predicted by the similarity solution for an ideal blast wave (b) Comparison of the time-of-propagation data for small Z_0 in Fig. 4.15(a) with the relationship predicted by the similarity solution for a plane and a spherical blast wave.

Fig. 4.16 Time-of-propagation of the shock wave for different laser spot sizes, 1.5 and 0.5 mm at atmospheric pressure. The velocity of the shock wave is computed from the derivative of the closest polynomial fit ($\Delta t_1=a_1x+a_2x^2$) to the time-of-propagation data. (circle: 1.5 mm, square: 0.5 mm)

Fig. 4.17 Time-of-propagation of the shock wave for different ambient pressures, 300 and 760 Torr as the laser spot size is kept to be small, 0.5 mm. (circle: 300 Torr, square: 760 Torr)

Fig. 4.18 Time-of-propagation of the shock wave over large propagation distances. Dashed lines represent the linear curve fitting of the data for large values of Z_0. (circle: d_s=2.1 mm, square: d_s=0.8 mm)

Fig. 4.19 Time-of-propagation of the shock wave with respect to the repetitive heating on the same spot

Fig. 4. 20 The energy contained in the laser induced blast wave estimated using the ideal strong blast wave solution. E_0^*=0.5 E_0 (E_0 is given by Eq. (4.12)). Data for p_∞= 300 Torr in Fig. 4.17 is used for the calculation.

Fig. 4.21 Deflection of the probe beam recorded over different intervals of time. All three signals are produced at the same experimental conditions. (E_p=7 mJ, Z_0=1.9 mm)

Fig. 4.22 Schematic representation of the density field for a plane wave that produces the deflection profile shown in the figure (The locations S, A, and B in both figure
correspond each other.)

Fig. 4.23 Schematic diagram for a small density field formed by the aluminum plume in the surrounding air.

Fig. 4.24 Deflection time-response profiles at later time for different ambient pressures (Z_0=1.27 mm).

Fig. 4.25 Scanning electron microscopy photographs of a mirror polished aluminum target heated by the excimer laser; pulse duration=21 ns, d_s=~0.5 mm, (a) 1 pulse (E_p=9.9 mJ), and (b) 5 pulses (average E_p=9.5 mJ) (c) 100 pulses (average E_p=9.3 mJ)

Fig. 4.26 Scanning electron microscopy photographs of a polished (with SiC paper #600) aluminum target heated by the excimer laser; pulse duration=21 ns, d_s=~0.7 mm, average E_p=11.0 mJ, (a) 20 pulses and (b) 100 pulses

List of Tables

Table 2.1 Thermal properties of the sample materials (at 293K)

Table 2.2 Depths (error : $\pm 20\mu m$) and aspect ratios of the cavities

Table 3.1. Thermophysical properties of Aluminum

Acknowledgments

I am indebted to my family who have been the source of help and encouragement throughout my education. Without my mother's sacrifice and unyielding courage against difficulties, it would never have been possible for me to become who I am. Also I heartily thank my wife Eun Young. I could concentrate on study only because she was willing to take all the pressure to take care of my son and to run the household.

I would like to thank my research adviser professor Ralph Greif of the Mechanical Engineering Department. With his help, I could find a research assistantship at the Lawrence Berkeley National Laboratory (LBNL) where I greatly enjoyed working on laser-material interactions studies. His detailed advice and review of my research materials greatly improved my ability to perform researches and to analyze the results. He has been the one whom I would consult with for any matter. I am deeply indebted to him.

I also would like to thank Dr. Richard E. Russo who is leading the laser-research group, '*Team Deastructo*', of the LBNL. I appreciate that he allowed me to join the group. His help and advice greatly helped me to develop experimental skills and to learn the way science is studied.

I thank my colleagues at LBNL who have helped me through my study. I thank Jonathan D. Spear for his help with the experimental system during the early period and Ronald P. Reade for his help with the excimer laser and Xianglei Mao for his help with experimental systems and discussion.

I also thank professor Mark A. Shannon at the University of Illinois at Urbana-Champaign for reviewing the numerical study and spending time to discuss the material. His advice was very helpful.

I am very grateful to Professor Per F. Peterson and Professor Costas P. Grigoropoulos for reviewing the dissertation and spending time to discuss subjects. Their advice greatly helped to improve the thesis.

Finally I would like to thank The Ministry of Education of Republic of Korea for its financial support during my study through Government fellowship.

This work was supported by the Office of Basic Energy Sciences, Chemical Sciences Division, Processes and Techniques Branch of the U.S. Department of Energy under Contract No. DE-AC03-76SF00098.

Chapter 1

Introduction

1.1 Laser ablation technology: overview

Since the laser was introduced as a new type of light source with unprecedented light characteristics in the early 1960s, the application of laser technology has received considerable attention in numerous areas such as manufacturing [1], materials processing [2], chemical analysis [3], high energy studies [4], optical communications [5], medical and biological applications [6], etc. Despite many useful applications of small power lasers (typically with a power of a few mili-Watts at most), the major interests through this thesis lies in the applications of high power lasers. High power continuous wave (CW) lasers produce laser light with a power of typically a few Watts for solid-state lasers and up to several kilo-Watts for carbon dioxide (CO_2) lasers. High power pulsed lasers, most commonly represented by excimer lasers and Nd-YAG (Neodymium-doped Yttrium Aluminum Garnet) lasers, produce laser pulses with pulse energy from several hundreds of mili-Joules to a few Joules. However, because the pulse duration of these lasers are on the order of nanoseconds or shorter, it is easy for these lasers to achieve the power densities of giga-Watts per square centimeters or higher. When a high power laser beam is incident onto a solid target, an immediate explosive material removal from the target occurs, which is termed 'laser ablation'. If the laser energy is properly selected,

laser ablation technology can be applied to virtually any materials for removal of mass. Among the high power pulsed lasers, excimer lasers are especially useful because of the short wavelength of the excimer laser light. The ultraviolet (UV) excimer laser light whose wavelength, λ, is typically in the range of 0.19-0.35 μm delivers to a target photons with at least 3-4 times higher energy than those from a Nd-YAG laser (λ=1.06 μm) and 30-40 times higher than a CO_2 laser (λ=10.6 μm). This high energy photons in the excimer laser light makes it easier to break the molecular structure of target materials. For CO_2 or Nd-YAG lasers more photons are required to do the same processing. Therefore, there may be less thermal loading on the target when using excimer lasers. A frequency quadrupled Nd-YAG laser (the wavelength of the light is reduced by one-quarter of the original 1.06 μm) can also produce UV laser light.

The advantage and importance of laser ablation technology, especially in science and engineering, may be better described from the following examples.

i) Laser processing in manufacturing

Until the excimer lasers or pulsed solid-state lasers became available, CO_2 lasers were the only high power lasers used in manufacturing processes for cutting, welding, and heat treatment. Since CO_2 lasers produce infrared (IR) light with a long wavelength (10.6 μm), metals having high reflectance at this wavelength are difficult to process. With the UV laser beam from an excimer laser or a frequency quadrupled Nd-YAG laser, these reflective metals and materials that are transparent to visible or IR lights, for example glasses, can be ablated easily. Due to the small thermal effect, UV laser ablation also

enables microscale processing of materials with suitably designed optical arrangements. The important applications of pulsed laser ablation in manufacturing include micromachining [7], microelectronics manufacturing [8], laser marking [9], laser surface cleaning [10], etc.

ii) Thin film processing

When a solid target is ablated by laser heating, the vapor or small particles can be collected on a nearby solid surface to make a thin film. The ability for making high temperature superconducting film by excimer laser ablation of bulk superconducting material greatly expedited researches of thin film deposition by pulsed laser ablation, often called pulsed laser deposition (PLD) [11,12]. The unique advantage of PLD is that the composition of complex multi-elementary materials can be closely reproduced in the thin film while conventional methods are more likely to render preferential vaporization [13]. Even though the principle of PLD process is relatively simple, the detailed processes including target ablation, vapor flow, and the deposition of vapor on the substrate are complex and not well understood. The formation of a plasma, clusters, and particles [14] at high laser power density (typically, > 1 GW/cm^2) and the gasdynamic characteristics of the expanding plume [15] need to be further studied to better utilize PLD. An increasing number of research papers related to PLD have been published over the past few years (for example, see [16,17,18,19,20]) and further active research in this area is expected to continue.

iii) Laser ablation sampling of solids for chemical analysis

Laser ablation of solids can be used as a powerful sampling technique for chemical analysis [3,21]. Laser ablation sampling can be applied to any solid material without time consuming and possibly contaminating sample preparation procedures. Also laser ablation sampling consumes only a small amount of sample material, typically in the range of ng or μg per pulse. Therefore personnel exposure, sample handling, and instrument contamination are minimized, which are especially important for toxic or radioactive samples. In conjunction with an analytical source, e.g. an inductively coupled plasma (ICP) [22,23], the laser sampling technique can be used for the analysis of virtually any sample. However, for all these laser-material interaction applications, the ablation mechanisms are not well established and only under ideal cases is stoichiometric sampling achieved. Further studies of the fundamental mechanisms describing laser-material interactions must be performed to advance this technology.

Owing to the usefulness of the laser ablation technology in diverse fields, there has been an explosive increase of research into ablation mechanisms since the 1980s and as a result, improvement in understanding the qualitative features of laser-material interactions. There also have been studies to quantitatively model the ablation mechanisms [24,25,26]. Even though applications of laser ablation technology have been improved greatly with advances in lasers and optics technology, understanding the principles of laser-material interactions has been elusive. High power pulsed laser heating of solid targets results in a extremely rapid melting, evaporation of the target, and often plasma formation. The interaction of the laser beam with the target can vary significantly

during these processes. For example, the reflectivity of the target surface changes with increasing temperature and melting of the target [27]. At high laser power density, the ionization of vapor becomes significant and plasma shielding may become important [28] Even a transformation of a metal target into a dielectric material can occur [29]. The primary mechanisms responsible for the material removal from the target during high power laser-solid interactions has not been elucidated. Even though thermal evaporation of the target material is common, the material removal mechanisms include thermal, electronic, collisional, thermo-mechanical, and a simultaneous combination of these mechanisms [30,31].

The difficulty of investigating the mechanisms described above become obvious when the time and length scales involved in laser-material interactions are considered. Due to the extremely short time scale during pulsed laser ablation processes (for example, tens of nanoseconds at most for excimer lasers) and to the small length scale of the heat affected zone in the target (tens of micrometers at most for the duration of a nanosecond laser pulse), the direct measurement of temperature or heat flux near the irradiated surface is virtually impossible. Instead the laser generated gasdynamic flow is most often studied. One of the widely employed methods is measurement of the propagation of laser induced shock wave and vapor. Several different techniques are available to measure the propagation of the laser induced gasdynamic flow. Probe beam deflection measurement [25,32], fast imaging [14], and fast photography [33,34] are most often used. For the probe beam deflection measurement, a probe laser beam is placed above the target and the bending of this probe beam is measured as it interacts with the flow field. When a

laser induced shock wave reaches the probe beam, the difference in density between the shock front and the ambient gas produces a refraction of the probe beam and results in a deflection of the probe beam from its original direction. The time it takes for the shock wave to reach the probe beam at different distances from the target surface is measured as the time-of-propagation data. By comparing the measured time-of-propagation data of a laser induced shock wave with blast wave theory the energy contained in the gasdynamic flow can be estimated. However, the characteristics of the laser induced gasdynamic flow are not exactly consistent with blast wave theory, which assumes one dimensional flow with negligible mass ablation from the target and a negligible ambient pressure. For example, Kelly [35] showed that a strong forward peaking of the particle velocity exists in the laser induced flow, which is different from the case of spherical expansion of the blast wave model. As a result, the energy conversion efficiency, defined by the ratio of the energy contained in the laser induced gasdynamic flow to the incident laser energy, is not always consistent among reported results. For better prediction of the laser energy coupling with solid targets by measuring the propagation of a laser induced shock wave, it is important to understand the effects of experimental parameters such as laser pulse energy, ambient pressure, and laser spot size on the propagation of a laser induced gasdynamic flow.

1.2 Scope of the present study

As stated above, laser energy coupling with the target is one of the most important subjects in high power laser heating of solids, although it is poorly understood. Good

theoretical analyses of the laser heating processes and systematic investigation of each parameter from the target, the heating laser, and the surrounding ambient are required. As the measurement of shock wave propagation is widely employed for the diagnosis of a laser induced gasdynamic flow, investigation of the shock wave velocity change with respect to experimental parameters is desirable. To challenge these problems, the following studies were carried out.

Through this dissertation the main focus of research remains on the high power laser heating of solids, especially metal targets. However, each chapter includes different studies to investigate the process. In chapter 2, phase changes of the target is not explicitly included even though material removal from the target is considered as a prerequisite to form the cavity studied in that chapter. Also the heating source used in this chapter is a CW laser while that in the following chapters is a pulsed laser. In chapters 3 and 4, the heating source, time scale, and length scales are the same in principle. The fundamental difference between these two chapters is that chapter 3 is a theoretical study while chapter 4 is an experimental work. Numerical simulation of the pulsed laser heating of metal targets is carried out in chapter 3 while the time-of-propagation measurement of laser induced flow with the probe beam deflection technique is the main subject of chapter 4. Therefore each chapter can be considered as a complete work by itself. The contents of each chapter is briefly outlined below.

In chapter 2, the effects of a cylindrical cavity in a metal surface on the energy coupling of a laser beam with the solid were investigated by using a photothermal deflection technique. The cavity was artificially drilled in the flat surface of a sample.

The photothermal deflection of a probe beam over the cavity was measured while the bottom of the cavity was heated with a CW Nd-YAG laser with a wavelength of 1064 nm. Cavities in three different materials and with two different aspect ratios were used for the experiments. Temperature distributions in the solid and the surrounding air were computed numerically and used to calculate photothermal deflections for cavity heating and for plane surface heating. The importance of multiple reflections of the heating laser beam inside the cavity was demonstrated. The overall energy coupling between a heating laser and a solid is enhanced by a cavity.

Chapter 3 presents a numerical model to analyze unsteady vaporization of a metal target due to nanosecond pulsed laser heating with an ambient gas of finite pressure. A one dimensional thermal evaporation model is employed for target heating with a detailed description of the vapor motion inside the Knudsen layer. For the gasdynamic flow of the vapor, the one dimensional compressible flow equations for an inviscid fluid are solved utilizing the reflection boundary condition. The effects of surface reflectivity on the overall laser energy coupling with the target and the effects of the ambient pressure on the velocity of the vapor leaving the Knudsen layer are investigated in detail. Results for target surface conditions and gasdynamic properties of the vapor for various laser fluences are obtained when the vapor velocity at the Knudsen layer is sonic.

Chapter 4 presents an experimental study on laser generated plume dynamics. The probe beam deflection technique was employed to determine the propagation of the shock wave through the surrounding air. The time-of-propagation of the shock wave was investigated with respect to important experimental parameters, i.e. laser pulse energy,

ambient pressure, and the propagation distance of the shock. Also the measured shock wave propagation was compared with blast wave theory. The experimental conditions for which the measured shock wave propagation agrees with blast wave theory were obtained. The propagation of gaseous target material is observed from the deflection at later time of the probe beam (after the shock wave has propagated a large distance).

Chapter 5 includes a summary of the preceding chapters and discussion.

References

[1] R. C. Crafer and P. J. Oakley, editors, *Laser processing in manufacturing*, 1993, Chapman and Hall

[2] E. Fogarassy and S. Lazare, editors, *Laser ablation of electronic materials; Basic mechanisms and applications*, 1992, North-Holland

[3] R. E. Russo, "Laser ablation", Applied Spectroscopy, Vol. 49, No. 9, 1995, pp. 14A-28A

[4] C. Yamanaka, *Introduction to laser fusion*, 1991, Harwood Academic Publishers, New York

[5] C. C. Eaglesfield, *Laser light; fundamentals and optical communications*, 1967, St. Martin's Press, London

[6] A. A. Oraevsky, R. O. Esenaliev, and V. S. Letokhov, "Pulsed laser ablation of biological tissue: Review of the mechanism", in *Laser ablation; mechanisms and applications*, edited by J. C. Miller and R. F. Haglund Jr., 1991, Springer, pp. 112-122

[7] E. K. Illy, A. C. J. Glover, M. J. Withford, and J. A. Piper, "High speed micro-machining with UV-copper vapor lasers", in *Lasers as tools for manufacturing of durable goods and microelectronics*, Proceedings of SPIE-The international society for optical engineering, Vol. 2703, 1996, pp. 432-441

[8] M. Rothschild, A. R. Forte, M. W. Horn, R. R. Kunz, S. C. Palmateer, and J. H. C. Sedlacek, "193-nm Lithography", in *Lasers as tools for manufacturing of durable goods and microelectronics*, Proceedings of SPIE-The international society for optical engineering, Vol. 2703, 1996, pp. 398-404

[9] A. B. May, "Continuous wave and Q-switched Nd:YAG lasers", in *Laser processing in manufacturing*, edited by R. C. Crafer and P. J. Oakley, 1993, Chapman and Hall, pp. 91-114

[10] C. Stauter, J. Fontaine, Th. Engel, and A. Biernaux, "Optical and acoustical techniques for the characterization of material ablation by Q-switched Nd:YAG and excimer radiation", in *Laser processing; Surface treatment and film deposition*, edited by J. Mazumder, O. Conde, R. Villar, and W. Steen, 1996, Kluwer Acamedic Publishers, pp. 881-892

[11] C. H. Chen, R. C. Phillips, P. W. Morrison, Jr., D. G. Hamblen, and P. R. Solomon, "In-situ monitoring of laser ablation of superconductors", in *Laser ablation; mechanisms and applications*, edited by J. C. Miller and R. F. Haglund, Jr., Springer, 1991, pp. 16-27

[12] D. B. Geohegan, "Spectroscopic and ion probe characterization of laser produced plasmas used for thin film growth", in *Laser ablation; mechanisms and applications*, edited by J. C. Miller and R. F. Haglund, Jr., Springer, 1991, pp. 28-37

[13] T. V. Venkatesan, "Pulsed-laser deposition of high-temperature superconducting thin films", in *Laser ablation; principles and applications*, edited by J. C. Miller, Springer, 1994, pp. 85-106

[14] D. B. Geohegan, "Imaging and blackbody emission spectra of hot particulates generated during laser ablation", in *Laser ablation; mechanisms and applications II*, edited by J. C. Miller and D. B. Geohegan, AIP Press, 1993, pp. 407-413

[15] A. Mele, A. Giardini Guidoni, R. Kelly, A. Miotello, S. Orlando, R. Teghil, and C. Flamin, "Angular distribution and expansion of laser ablation plumes measured by fast intensified charge coupled device photographs", Nuclear Instruments and Methods in Physics Research B 116, 1996, pp. 257-261

[16] R. P. Reade, X. L. Mao, and R. E. Russo, "Characterization of Y-Ba-Cu-O thin films and yttria-stablized zirconia intermediate layers on metal alloys grown by pulsed laser deposition", Appl. Phys. Lett., 59(6), 1991, pp. 739-741

[17] R. P. Reade, S. R. Church, and R. E. Russo, "Ion-assisted pulsed-laser deposition", Rev. Sci. Instrum., 66(6), 1995, pp. 3610-3614

[18] R. P. Reade and R. E. Russo, "Ion-assisted pulsed-laser deposition for the fabrication of Y-Ba-Cu-O multilayer structures using oriented intermediate layers of YSZ and CeO_2", Applied Surface Science, 96-98, 1996, pp. 726-730

[19] J. T. Cheung and H. Sankur, "Growth of thin films by laser-induced evaporation", CRC critical reviews in solid state and materials sciences, Vol. 15, Issue 1, 1988, pp. 63-109

[20] R. K. Singh and J. Narayan, "Pulsed-laser evaporation technique for deposition of thin films: Physics and theoretical model", Physical Review B, Vol. 41, No. 13, 1990, pp. 8843-8859

[21] M. Caetano, X. L. Mao, and R. E. Russo, "Laser ablation solid sampling: vertical spatial emission intensity profiles in inductively coupled plasma", Spectrochimica Acta Part B 51, 1996, pp. 1473-1485

[22] R. E. Russo, X. L. Mao, W. T. Chan, M. F. Bryant, and W. F. Kinard, "Laser ablation sampling with inductively coupled plasma atomic emission spectrometry for the analysis of protopical glasses", Journal of Analytical Atomic Spectroscopy, Vol. 10, 1995, pp. 295-301

[23] A. Fernandez, X. L. Mao, W. T. Chan, M. A. Shannon, and R. E. Russo, "Correlation of spectral emission intensity in the inductively coupled plasma and laser-induced plasma during laser ablation of solid samples", Analytical Chemistry, Vol. 67, No. 14, 1995, pp. 2444-2450

[24] S. Petzoldt, A. P. Elg, M. Reichling, J. Reif, and E. Matthias, "Surface laser damage thresholds determined by photoacoustic deflection", Appl. Phys. Lett., 53 (21) 1988, pp. 2005-2007

[25] J. A. Sell, D. M. Heffelfinger, P. Ventzek, and R. M. Gilgenbach, "Laser beam deflection as a probe of laser ablation of materials", Appl. Phys. Lett., 55(23) 1989, pp. 2435-2437

[26] E. Welsch, K. Ettrich, M. Peters, W. Ziegler, and H. Blaschke, "Application of photothermal probe beam deflection technique for ablation and damage measurements by using short UV laser pulses", Journal de Physique IV, Vol. 4, 1994, pp. 749-752

[27] A. M. Prokhorov, V. I. Konov, I. Ursu, and I. N. Mihailescu, *Laser heating of metals*, 1990, Adam Higler

[28] X. L. Mao and R. E. Russo, "Observation of plasma shielding by measuring transmitted and reflected laser pulse temporal profiles", Appl. Phys. A, Vol. 64 1997, pp. 1-6

[29] V. A. Batanov, F. V. Bunkin, A. M. Prokhorov, and V. B. Fedorov, "Evaporation of metallic targets caused by intense optical radiation", Soviet Physics JETP, Vol. 36, No. 2, 1973, pp. 311-322

[30] R. Kelly, A. Miotello, B. Braren, A. Gupta, and K. Casey, "Primary and secondary mechanisms in laser-pulse sputtering", Nuclear Instruments and Methods in Physics Research B 65, 1992, pp. 187-199

[31] R. W. Dreyfus, R. Kelly, and R. E. Walkup, "Laser-induced fluorescence studies of excimer laser ablation of Al_2O_3", Appl. Phys. Lett., 49(21), 1986, pp. 1478-1480

[32] J. Diaci and J. Mozina, "A study of energy conversion during Nd-YAG laser ablation of metal surfaces in air by means of a laser beam deflection probe", Journal De Physique IV, Vol. 4, 1994, pp. 737-743

[33] G. Callies, P. Berger, and H. Hugel, "Time-resolved observation of gas-dynamic discontinuities arising during excimer laser ablation and their interpretation", J. Phys. D: Appl. Phys., 28, 1995, pp. 794-806

[34] A. Gupta, B. Braren, K. G. Casey, B. W. Hussey, and R. Kelly, "Direct imaging of the fragments produced during excimer laser ablation of $YBa_2Cu_3O_{7-\delta}$", Appl. Phys. Lett., 59 (11), 1991, pp. 1302-1304

[35] R. Kelly and B. Braren, "On the direct observation of the gas-dynamics of laser-pulse sputtering of polymers", Appl. Phys. B 53, 1991, pp. 160-169

Chapter 2

Laser heating of a cavity versus a plane surface for metal targets; A study of energy coupling

2.1 Introduction

In this chapter, the effects of a cylindrical cavity in a metal surface on the energy coupling of a laser beam with the solid are investigated. For the study, cylindrical cavities are artificially drilled in metal targets and heated with a continuous wave Nd-YAG laser without melting or evaporation of the target material. The cylindrical cavities are assumed to simulate craters which are formed by evaporation or ablation of the target materials during laser processing of materials [1]. The presence of a crater in a solid surface during laser heating can change the rate of material removal and the mechanisms of laser energy transfer to the target. If a crater is developed by laser evaporation, e.g. during laser drilling, the interaction of the laser beam with the vapor and/or with the melt within the crater will be different from that which occurs when there is no crater. The energy coupling between a laser and a target when a crater exists has been investigated by many researchers. Dowden and co-workers [2,3] analyzed the energy transfer within a crater as an interaction of the laser beam with the vapor plasma while Trappe et al.[4] assumed that the laser energy is absorbed directly at crater surfaces and not by the vapor. Arata and Miyamoto [5] showed that the reflection loss of the laser energy is less for a

deeper crater. Kar et al. [6] showed that multiple reflections of the laser beam inside a crater lead to higher deposition of laser energy in the material.

Experimentally, the photothermal deflection measurement technique is utilized to investigate the change of the energy coupling between the laser beam and the solid due to the cavity. The photothermal deflection technique has been used for sensitive measurements of the thermal response of a heated solid surface since the early 1980s [7]. When a solid surface is heated periodically, the temperature of the surface changes periodically and so does the temperature of the ambient medium adjacent to the surface, resulting in a change of the refractive index of the medium. A probe laser beam passing parallel to the solid surface is deflected due to the refractive index change of the medium and this deflection is studied to investigate the thermal response of the solid. When the deflection of a probe laser beam is associated purely with the thermal gradient in the ambient medium, the deflection is called photothermal deflection. The photothermal or probe beam deflection technique has been utilized in various studies of laser-material interactions, e.g. heat transfer during the laser heating of solids [8], laser-induced melting of solid surfaces [9], laser ablation of materials [10], and laser-induced plasmas [11,12].

The photothermal deflection, $\vec{\phi}$, during laser heating of a solid surface can be determined by (see Appendix)

$$\vec{\phi} = \frac{1}{n}\frac{dn}{dT}\int_{path} \nabla_{\perp} T ds \qquad (2.1)$$

where n is the index of refraction of the surrounding air and $\nabla_{\perp} T$ is the gradient of temperature of the air perpendicular to the path of the probe beam, s. Analytical

expressions for the photothermal deflection can be found for the heating of a plane surface (with no cavity) [13,14]. For a plane surface the temperature field decreases exponentially normal to the surface with the highest temperature at the surface. Therefore if the surface temperature is increased, the temperature gradient above the surface also increases and so does the photothermal deflection amplitude. However, the photothermal deflection over a surface with a cavity is difficult to predict analytically because of the complexity of the temperature field.

In this chapter, the photothermal deflection of a probe beam during laser heating of metal surfaces with and without cylindrical cavities is investigated with experimental and numerical methods. The effects of a cavity on the energy coupling of the laser with a target and on the photothermal deflection response are investigated. Results for target materials with different thermal properties and cavities with different aspect ratios are discussed.

2.2 Experimental system

A schematic diagram of the experimental system is shown in Fig. 2.1. A CW Nd-YAG laser (Spectra-Physics 3000 series) with a wavelength of 1064 nm is used as the heating source. The laser beam is modulated with a mechanical chopper. A He-Ne laser (Electro-Optics) with a wavelength of 543.5 nm is used as the probe beam. The deflection of the probe beam is detected with a linear position detector (United Detector Technology, Model LSC-5D) and recorded with a lock-in amplifier (Stanford Research Systems, Model SR530) and a digital oscilloscope (Tektronix, Model DSA 602A).

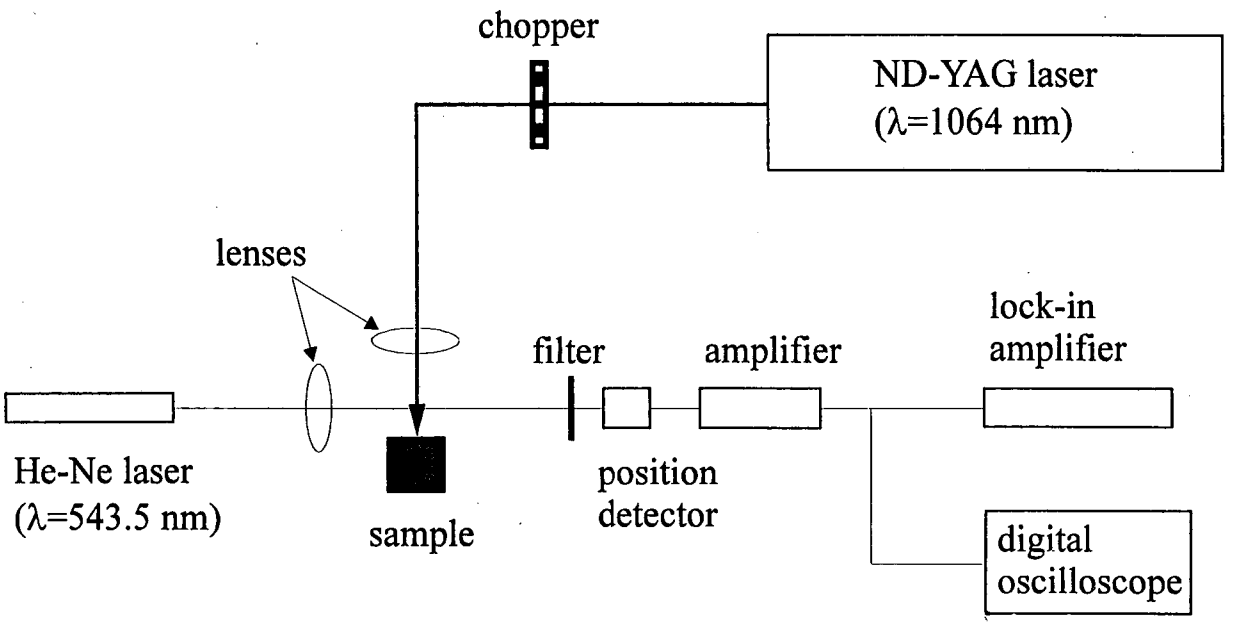

Fig. 2.1 Schematic diagram of the experimental system

Three materials, copper, lead, and stainless steel, were used in the experiments. The thermal diffusivities of copper, lead, and stainless steel are higher, about the same, and lower, respectively, than that of air; typical values at room temperature are given in Table 2.1 [15]. The exact composition of the stainless steel used in the experiment is unknown, and thus its thermal diffusivity can vary from 0.4 to 1.0×10^{-5} m^2/s [16]. However, the thermal diffusivity of the stainless steel is less than one-half of that of air.

The samples were machined into cubes with side-lengths of 1 cm. At the center of the top surface of each cube a cylindrical cavity is made using a drill. The diameter of all cavities are about 1 mm. Depths and aspect ratios of the cavities are shown in Table 2.2. The aspect ratios of these samples, defined by the depth of the cavity divided by the diameter, are 0.47 and 0.49 for copper and stainless steel samples, respectively, and 0.32

Table 2.1 Thermal properties of the sample materials (at 293K)

Sample	Thermal diffusivity(m^2/s)	Thermal conductivity(W/m K)
Copper	10.27×10^{-5}	386.0
Lead	2.06×10^{-5}	35.1
Stainless steel	0.44×10^{-5}	16.0
Air	2.10×10^{-5}	2.57×10^{-2}

Table 2.2 Depths (error : ±20μm) and aspect ratios of the cavities

Sample	Depth(μm)	Aspect Ratio
Copper	470	0.47
Lead	320	0.32
	890	0.89
Stainless Steel	490	0.49

and 0.89 for two lead samples. The top surface of each cube and the surfaces inside the cavity are polished to the same condition using silicon carbide powder. To minimize the deviation of the incident laser beam from the normal at the bottom surface of the cavity, the bottom surface of each cavity is made flat by polishing.

The probe beam, parallel to the sample surface, is focused and its diameter above the cavity location is about 110 μm at $1/e^2$ of its maximum intensity. The heating laser beam is assumed to have a Gaussian profile and focused on the sample surface. The $1/e^2$ diameter of the heating laser beam at the elevation of the center of the probe beam is about 710 μm and decreases to about 530 μm at a distance 1 mm below this location due to focusing. All laser beam diameters were measured using a 10 μm pinhole scanned across the beam with a photodiode. Total power of the heating laser beam is about 1.8 W.

Positioning of the probe beam for measurements of photothermal deflection for cavity heating and for plane surface heating is shown in Fig. 2.2. For cavity heating the probe beam is located 100 μm above the sample surface so that the distance from the bottom of the cavity to the probe beam is equal to the depth of the cavity plus 100 μm. The photothermal deflection response for plane surface heating is measured with the same normal offset of the probe beam, Z_0, as for cavity heating. To minimize alignment problems the photothermal deflection response for plane surface heating is measured after translating the sample with a cavity horizontally by 2 mm so that the heating laser beam is far from the cavity. The thermal diffusion length for the heating of plane surfaces, defined by $\sqrt{\alpha / \pi f_0}$, where α is thermal diffusivity and f_0 is the modulation frequency of the heating laser, is much smaller than the 2 mm distance between the heating laser beam and the cavity; thus the influence of the cavity on the temperature distribution and the photothermal deflection response for plane surface heating is negligible.

2.3 Numerical Modeling

The temperature field and the photothermal deflection response were computed numerically for conduction heat transfer in the solid and in the surrounding air for cavity heating and for plane surface heating. The equations solved are;

Gas temperature

$$\frac{1}{\alpha_g}\frac{\partial T_g(r,z,t)}{\partial t} = \frac{\partial^2 T_g(r,z,t)}{\partial r^2} + \frac{1}{r}\frac{\partial T_g(r,z,t)}{\partial r} + \frac{\partial^2 T_g(r,z,t)}{\partial z^2} \tag{2.2}$$

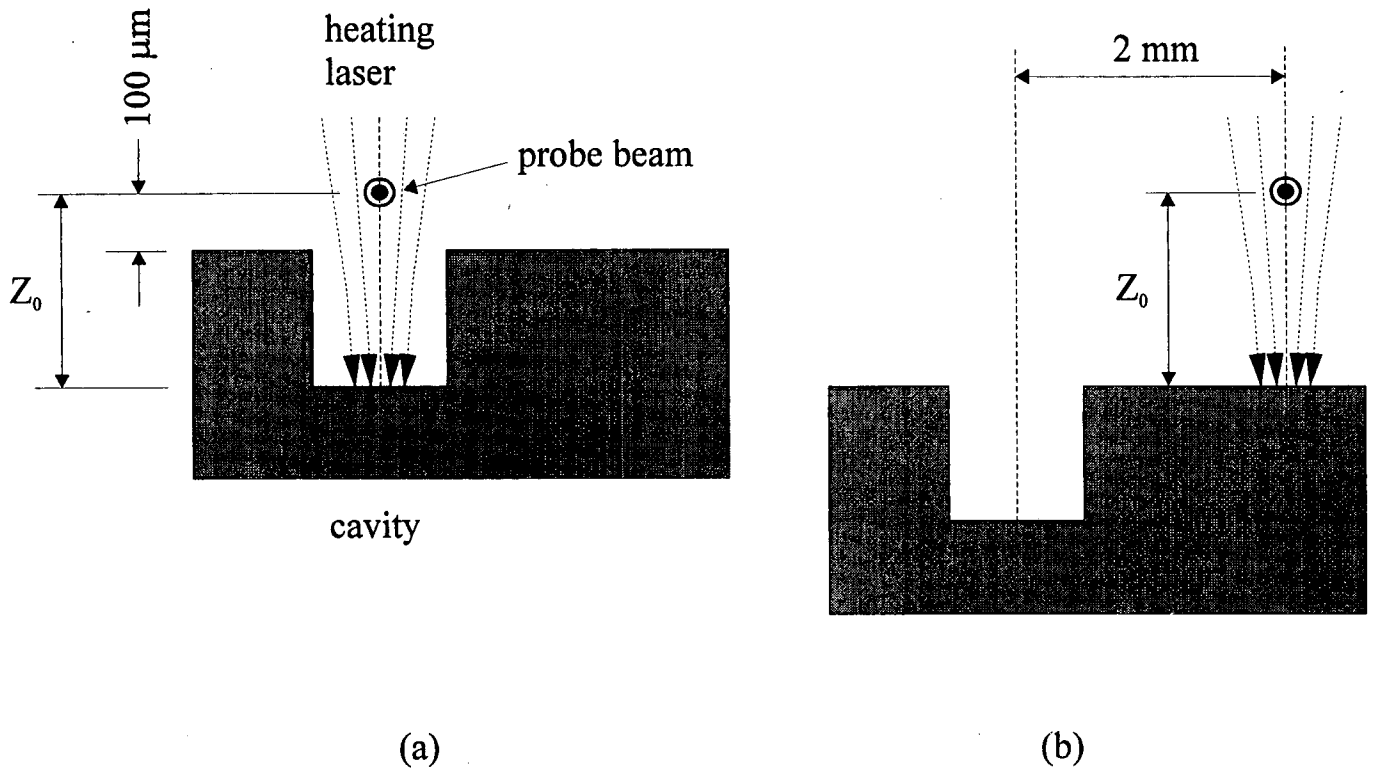

Fig. 2.2 Positioning of the probe beam for measurements of photothermal deflection (a) for cavity heating and (b) for plane surface heating

Solid temperature

$$\frac{1}{\alpha_s}\frac{\partial T_s(r,z,t)}{\partial t} = \frac{\partial^2 T_s(r,z,t)}{\partial r^2} + \frac{1}{r}\frac{\partial T_s(r,z,t)}{\partial r} + \frac{\partial^2 T_s(r,z,t)}{\partial z^2} + \frac{q(r,z,t)}{k_s} \tag{2.3}$$

Initial conditions

$$T_s(r,z,0) = T_\infty \text{ and } T_g(r,z,0) = T_\infty \tag{2.4a}$$

Boundary conditions

$$T_g(r, z \to \infty, t) = T_\infty \tag{2.4b}$$

$$T_s(r, z \to -\infty, t) = T_\infty \tag{2.4c}$$

$$T_g(r \to \infty, z, t) = T_\infty \text{ and } T_s(r \to \infty, z, t) = T_\infty \tag{2.4d}$$

$$T_s(r_i, z_i, t) = T_g(r_i, z_i, t) \text{ and } k_s \frac{\partial T_s(r_i, z_i, t)}{\partial n} = k_g \frac{\partial T_g(r_i, z_i, t)}{\partial n} \tag{2.4e}$$

where $T(r,z,t)$ is temperature, with r and z representing the radial and axial directions, and α and k are thermal diffusivity and thermal conductivity, respectively. The subscripts, s and g represent the solid and the surrounding air, respectively. Also the subscript i represents the interface between the solid and the air which is defined by z_i=0 for $0 \le r_i < \infty$ for a plane surface and z_i=0 for $0 \le r_i < R_c$, $r_i = R_c$ for $0 \le z_i < d_c$, and $z_i = d_c$ for $R_c < r_i$, for a cavity, where R_c and d_c represent the radius and the depth of the cavity, respectively. The coordinate n is normal to the interface between the solid and the air. The source term, $q(r,z,t)$, represents the laser energy absorbed by the solid and is expressed by

$$q(r,z,t) = A\,(1-R)\frac{P}{\pi a^2}\exp(-r^2/a^2)\exp(A\,z)f(t) \text{ for } 0 \le r < R_c \tag{2.5a}$$

$$q(r,z,t) = 0 \qquad \text{for } R_c \le r \tag{2.5b}$$

where A is the absorption coefficient of the solid at the wavelength of the heating laser beam (m^{-1}), R is the reflectivity of the solid surface, P is the total power of the Gaussian heating laser beam (W), a is the $1/e^2$ radius of the heating laser beam at the solid surface (m), and f(t) is the function for the temporal profile of the heating laser beam.

In section 2.4. C, reflection of the heating laser beam at the bottom of a cavity is discussed. When absorption of this reflected laser energy on the cavity wall is included, Eq. (2.4e) becomes

$$T_s(r_i,z_i,t) = T_g(r_i,z_i,t) \text{ and } k_s \frac{\partial T_s(r_i,z_i,t)}{\partial r} + q_r(z_i,t) = k_g \frac{\partial T_g(r_i,z_i,t)}{\partial r} \tag{2.6a}$$

for $r_i = R_c$ and $0 \le z_i < d_c$. The additional heat flux, $q_r(z_i,t)$, represents the reflected laser energy absorbed on the cavity wall, which is expressed by

$$q_r(z_i,t) = \frac{R(1-R)}{R_c dz_i} \frac{P}{\pi a^2} f(t) \int_0^{R_c} \exp(-r^2/a^2) dF_{dr \to dz_i, z_i} r dr \tag{2.6b}$$

where $dF_{dr \to dz_i, z_i}$ is the view factor between an element at the cavity bottom and an element on the cavity wall with a distance z_i.

The following variables are defined to normalize Eqs. (2.2)-(2.6).

$$\theta = \frac{T - T_\infty}{T_c}, \ \tau = t/t_c, \ r' = r/l_c, \ z' = z/l_c \tag{2.7}$$

where the characteristic quantities are $l_c = a$, $t_c = a^2/\alpha_s$, and $T_c = A(1-R)P/\pi k_s$. The dimensionless equations are as follows.

Gas temperature

$$\frac{\alpha_s}{\alpha_g}\frac{\partial\theta_g(r',z',\tau)}{\partial\tau}=\frac{\partial^2\theta_g(r',z',\tau)}{\partial r'^2}+\frac{1}{r'}\frac{\partial\theta_g(r',z',\tau)}{\partial r'}+\frac{\partial^2\theta_g(r',z',\tau)}{\partial z'^2} \tag{2.8}$$

Solid temperature

$$\frac{\partial\theta_s(r',z',\tau)}{\partial\tau}=\frac{\partial^2\theta_s(r',z',\tau)}{\partial r'^2}+\frac{1}{r'}\frac{\partial\theta_s(r',z',\tau)}{\partial r'}+\frac{\partial^2\theta_s(r',z',\tau)}{\partial z'^2}+q(r',z',\tau) \tag{2.9}$$

Initial conditions

$$\theta_s(r',z',0)=0 \text{ and } \theta_g(r',z',0)=0 \tag{2.10a}$$

Boundary conditions

$$\theta_g(r',z'\to\infty,\tau)=0 \tag{2.10b}$$

$$\theta_s(r',z'\to-\infty,\tau)=0 \tag{2.10c}$$

$$\theta_g(r'\to\infty,z',\tau)=0 \text{ and } \theta_s(r'\to\infty,z',\tau)=0 \tag{2.10d}$$

$$\theta_s(r_i',z_i',\tau)=\theta_g(r_i',z_i',\tau) \text{ and } k_s\frac{\partial\theta_s(r_i',z_i',\tau)}{\partial n'}=k_g\frac{\partial\theta_g(r_i',z_i',\tau)}{\partial n'} \tag{2.10e}$$

where

$$q(r',z',\tau)=\exp(-r'^2)\exp(A\,az')f(\tau) \qquad \text{for} \qquad 0\le r'<R_c' \tag{2.11a}$$

$$q(r',z',\tau)=0 \qquad \text{for} \qquad R_c'\le r' \tag{2.11b}$$

and

$$f(\tau)=1 \qquad \text{for} \qquad 0<\tau\le \tau_0/2 \tag{2.12a}$$

$$f(\tau)=0 \qquad \text{for} \qquad \tau_0/2<\tau\le\tau_0 \tag{2.12b}$$

where τ_0 is the period of the modulation. Eqs. (2.6a) and (2.6b) become in dimensionless form:

$$\theta_s(r_i', z_i', \tau) = \theta_g(r_i', z_i', \tau) \text{ and } \frac{\partial \theta_s(r_i', z_i', \tau)}{\partial r'} + q_r(z_i', \tau) = \frac{k_g}{k_s} \frac{\partial \theta_g(r_i', z_i', \tau)}{\partial r'} \quad (2.13a)$$

$$q_r(z_i', \tau) = \frac{(R/Aa)}{R_c' \, dz_i'} f(\tau) \int_0^{R_c'} \exp(-r'^2) dF_{dr' \to dz_i', z_i'} r' \, dr' \quad (2.13b)$$

2.4 Results and Discussion

2.4.1 Experimental results

Amplitudes of the photothermal deflection response, measured with the lock-in amplifier for laser heating of the cavity and the plane surface, are compared for the three materials. Cavities for these comparisons have aspect ratios of 0.47, 0.32, and 0.49 for copper, lead, and stainless steel, respectively. These data are shown in Fig. 2.3. For copper, the amplitude of the photothermal deflection response from heating the bottom of the cavity is 240-300% higher than for the plane surface over the frequency range of 97-300 Hz. For lead, the amplitude for the cavity is only about 20% higher than for the plane surface at low frequencies and the difference decreases at higher frequency over the frequency range of 97-900 Hz. For stainless steel, the amplitudes for both the cavity and the plane surface are similar over the frequency range of 97-600 Hz.

Amplitudes of the photothermal deflection response from samples with different aspect ratios were investigated with lead samples. The results for an aspect ratio of 0.32 are shown in Fig. 2.3(b) and for an aspect ratio of 0.89 in Fig. 2.4. For the latter, the amplitude from heating the cavity is about 20% higher than for the plane surface at low

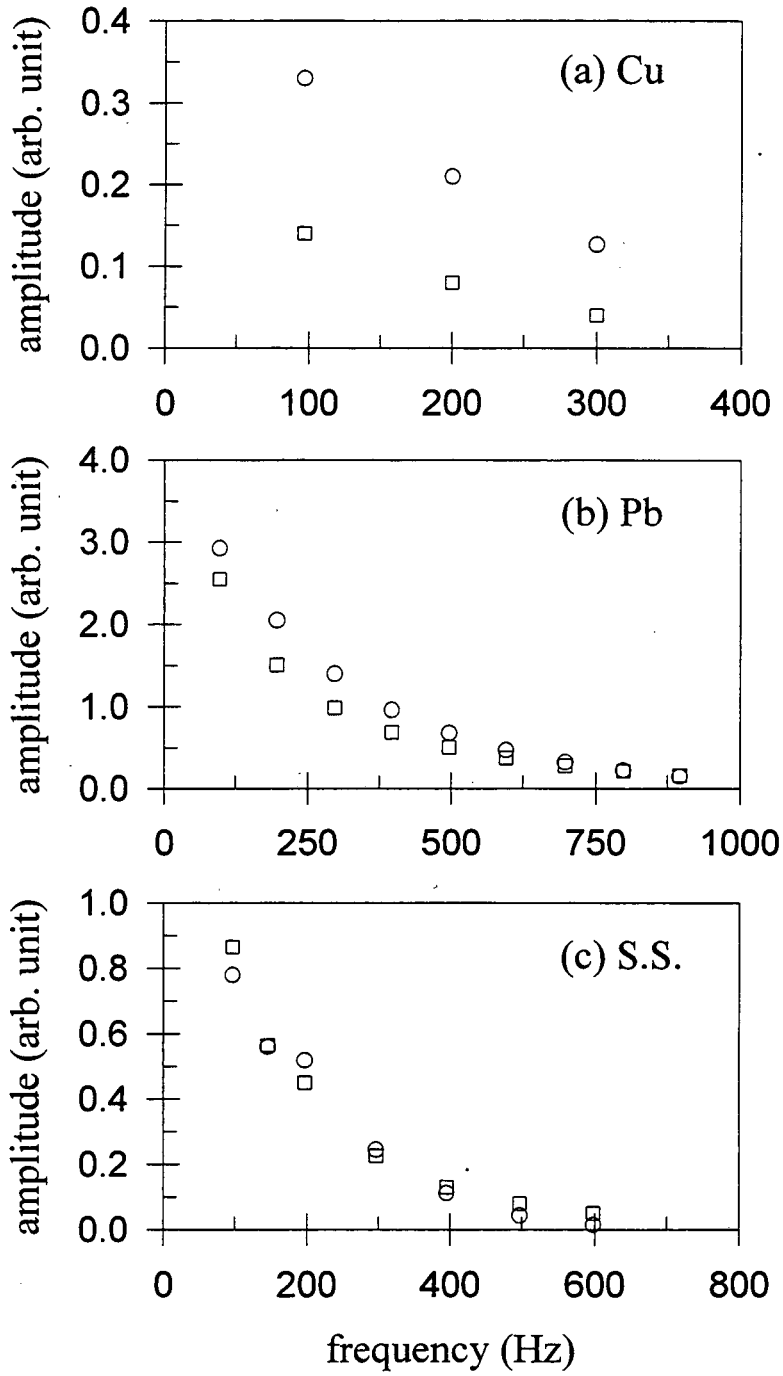

Fig. 2.3 Photothermal deflection amplitudes for a cavity heating and a plane surface heating for (a) copper, (b) lead, and (c) stainless steel (circle: cavity, square: plane surface)

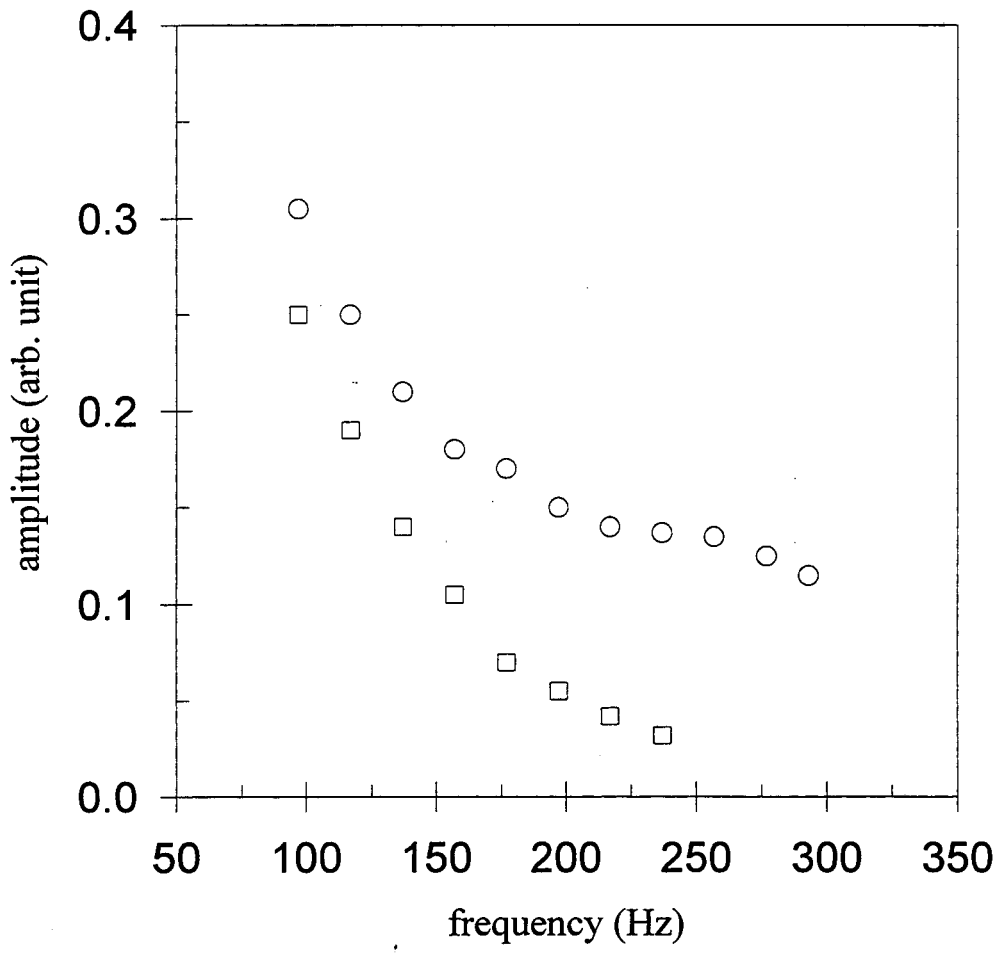

Fig. 2.4 Photothermal deflection amplitudes from heating a cavity of aspect ratio of 0.89 and a plane surface for lead (circle: cavity, square: plane surface)

frequencies and, in contrast to the sample of aspect ratio of 0.32, the difference of the amplitudes increases with frequency.

The time response of the photothermal deflection with respect to the laser heating is also examined by the signals obtained on the oscilloscope during the same measurements. Regardless of the material or the aspect ratio of the samples, cavities showed faster responses to the laser heating than plane surfaces for the same conditions.

2.4.2 Numerical results

The temperature distributions in the target and in the surrounding air were computed by using a finite difference method with Eqs. (2.8)-(2.12) for cavity heating and for plane surface heating. The data used for the computation are: modulation frequency of the heating laser, f_0=50 Hz (corresponds to τ_0=5.706, 1.144, and 0.244 for copper, lead, and stainless steel, respectively); radius of the heating laser, a=600 μm; dimensionless radius of the cavity, R_c'=1.67; absorption coefficient of metal surfaces [17] (assumed to be the same for all materials), $A=1.0\times 10^7$ m^{-1}. The same aspect ratio of the cavity, 0.5, was used for all materials in the computation.

Dimensionless isotherms at $\tau=0.7\tau_0$ for the cavity and the plane surface for the three materials are shown in Figs. 2.5-2.7. For copper, Fig. 2.5, the isotherms in the surrounding air at the elevation of the probe beam (z'=2.0) are very similar near the center of the heating laser beam (r'=0) for the cavity and the plane surface. However, away from the center of the heating laser beam (for example, r'=4.0) the isotherms for the cavity show higher air temperatures than for the plane surface at the same elevation.

At this location the dimensionless distance from the sample surface to the probe beam is only 0.33 for the cavity while it is 2.0 for the plane surface. Since the rate of conduction heat transfer is inversely proportional to the distance between two temperatures, the heat transfer rate between the sample surface and the air at the probe beam elevation for the cavity increases by a factor of 6 from that of the plane surface for $r' > R_c'$ due to the shorter distance. The dimensionless temperatures of the sample surfaces at r'=4.0 at the time τ=0.7τ_0 are 0.964×10^{-3} and 1.516×10^{-3} for the cavity and the plane surface, respectively. Even though the temperatures of the sample surfaces at r'=4.0 are different the dominant effect on the heat transfer at this location is still the smaller distance of 0.33 (for the cavity) which results in more heat transfer for the cavity. Therefore the higher temperatures of air at the probe beam elevation for $r' > R_c'$ for the cavity is mainly due to the short distance from the sample surface. For lead and stainless steel, Figs. 2.6 and 2.7, the isotherms for the cavity and for the plane surface at the probe beam elevation are similar in the region near the center of the heating laser beam as occurred for copper. However, the isotherms for these materials show smaller heat diffusion in air at the probe beam elevation for the cavity than for the plane surface. The isotherms for lead and stainless steel also show that little heat is transferred away from the heated region within the time period of 0.7τ_0 due to the smaller thermal diffusivities of lead and stainless steel as compared to copper. Thus the increase of heat transfer resulting from the short distance between the sample surface and the probe beam elevation for a cavity for $r' > R_c'$ is not present for these materials. The computed temperature gradients, $\partial\theta_g/\partial z'$, at the center

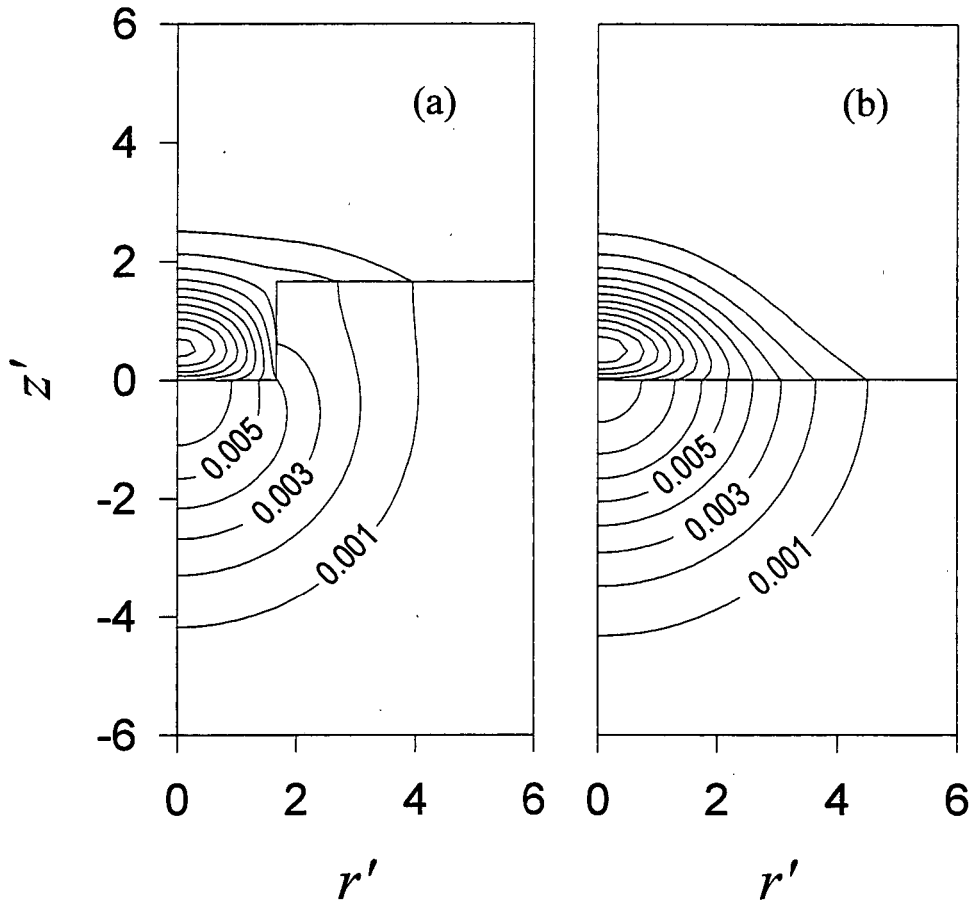

Fig. 2.5 Temperature distributions in the target and in the surrounding air for copper at $\tau=0.7\tau_0$ for (a) cavity heating and for (b) plane surface heating

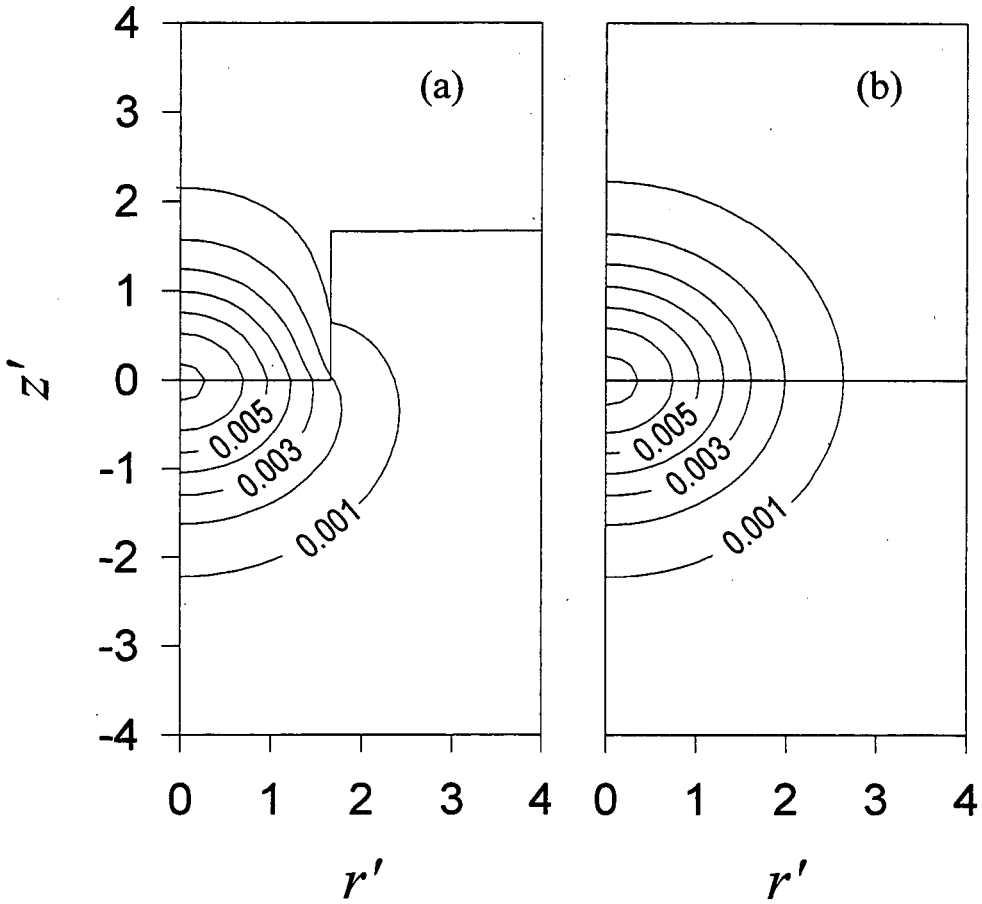

Fig. 2.6 Temperature distributions in the target and in the surrounding air for lead at $\tau=0.7\tau_0$ for (a) cavity heating and for (b) plane surface heating

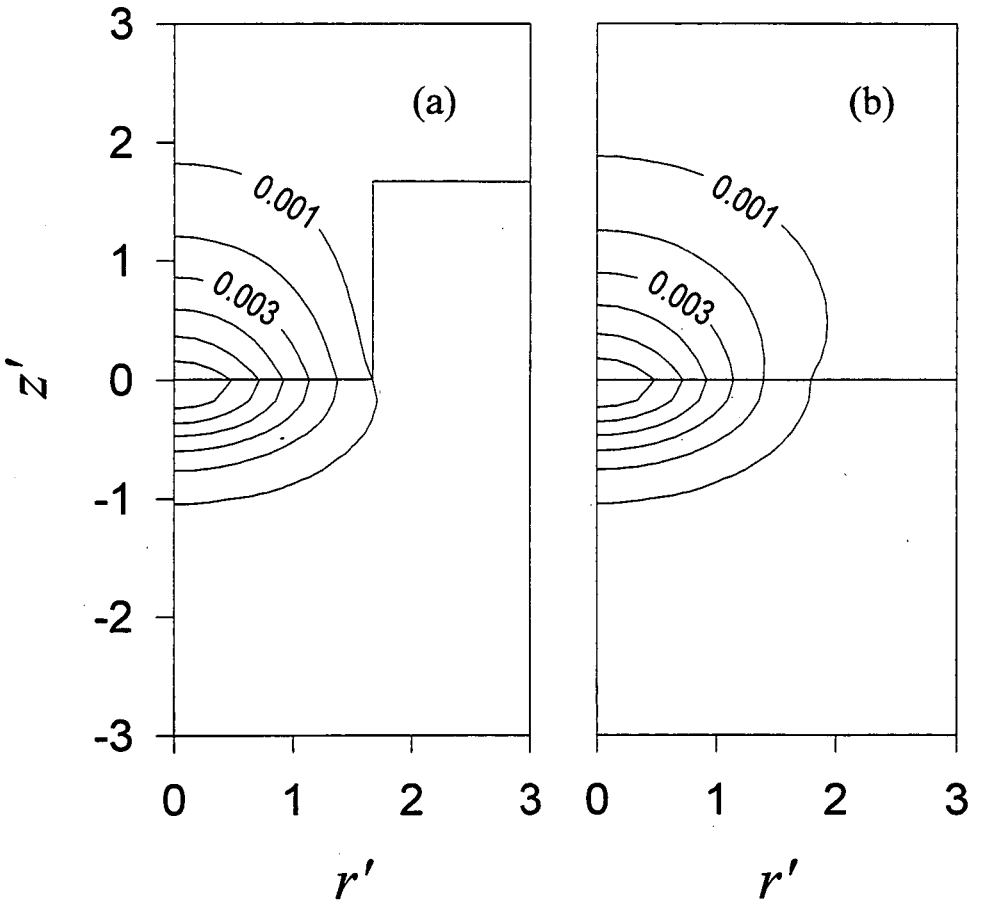

Fig. 2.7 Temperature distributions in the target and in the surrounding air for stainless steel at $\tau=0.7\tau_0$ for (a) cavity heating and for (b) plane surface heating

of the heating laser beam at different distances from the heated solid surface appear to be very close for the cavity and for the plane surface for the three materials. Accordingly, the smaller heat diffusion for the cavity for lead and stainless steel should yield a smaller photothermal deflection than for the plane surface (the photothermal deflection, Eq. (2.1), is proportional to the integral of the temperature gradient).

The normalized photothermal deflection is defined and computed using the temperature data as follows.

$$\phi'(z'_0,\tau) = \int_0^{r_s'} \frac{\partial\theta(r',z'_0,\tau)}{\partial z'} dr' \approx \sum_{i=1}^{NR} \frac{\theta(i,j_0+1)-\theta(i,j_0-1)}{2\Delta z'} \cdot \Delta r' \qquad (2.14)$$

where r_s' is the upper limit of the computation domain in the r-direction and z'_0 is the elevation of the probe laser beam above the surface (j_0 is the corresponding grid point in the same direction). Photothermal deflections computed using Eq. (2.14) for copper, lead, and stainless steel are shown in Fig. 2.8. For copper, the maximum amplitude of the computed photothermal deflection for the cavity is about 28% higher than for the plane surface. The computed photothermal deflection for the cavity also shows a faster time response than the plane surface. In contrast, the results for lead and stainless steel show that the maximum amplitudes of the computed photothermal deflection for the cavity are about 30% and 37% less, respectively, than for the plane surface and time responses are slower for the cavity.

2.4.3 Discussion

The computed photothermal deflections show major differences from the

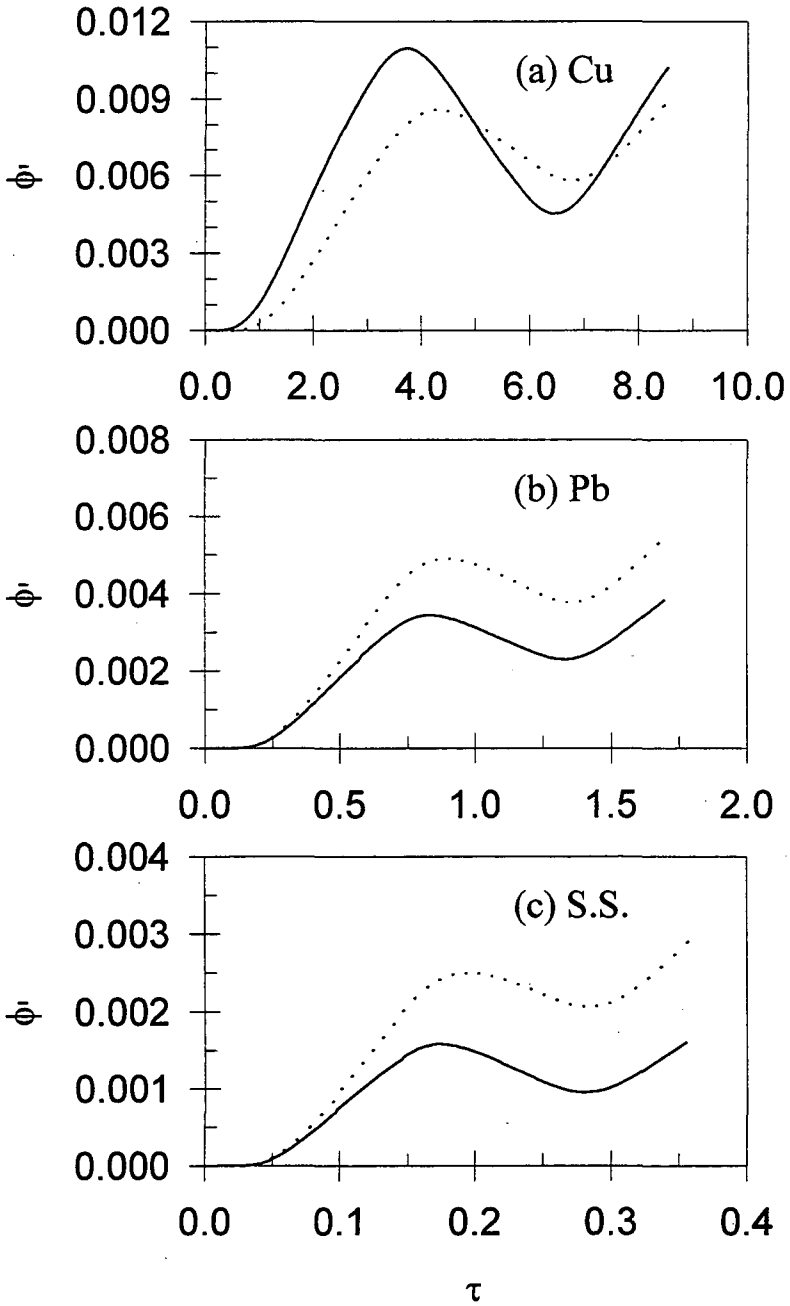

Fig. 2.8 Computed photothermal deflections for cavity heating and for plane surface heating for (a) copper, (b) lead, and (c) stainless steel (z_0'=2.17, solid line: for a cavity, dotted line: for a plane surface)

measured photothermal deflection responses. In particular, the ratio of the computed photothermal deflection amplitudes for cavity heating to plane surface heating is much smaller than that from the experiment. Also the computed photothermal deflections for cavity heating show a slower time response than for plane surface heating for lead and stainless steel, while the experimental results show the reverse of this behavior. The numerical model only considers conduction of heat in the solid and in the surrounding air resulting from heating at the bottom of the cavity, but other important energy transfer mechanisms may also be present. Multiple reflections and absorption of the heating laser beam inside the cavity may be important. Diffuse view factors between the bottom surface and the opening of the cavity [18] are 0.38 and 0.17 for cavities of aspect ratio of 0.5 and 1.0, respectively. Assuming that reflection of the heating laser beam at the bottom surface of the cavity is diffuse, this means that more than 60% of the reflected heating laser beam is irradiated onto the cavity wall for a cavity of aspect ratio 0.5 and over 80% for an aspect ratio of 1.0. To estimate the effect of the reflection of the heating laser beam on the energy transfer, the determination of the temperature of the solid and the surrounding air was made including irradiation of the reflected heating laser beam on the cavity wall. For this condition Eqs. (2.13a) and (2.13b) are used as the boundary condition at the cavity wall. Only the reflection of the primary heating laser beam at the bottom surface of the cavity is included in this computation with the assumption of diffuse reflection. Multiple reflections of the laser beam on the cavity wall are excluded. Reflectivities of the materials are assumed to be 0.9, 0.8, and 0.9 for copper, lead, and stainless steel, respectively [19]. The dimensionless isotherms computed with and

without absorption of the reflected laser energy on the cavity wall are shown in Fig. 2.9 for copper. The isotherms show larger heat diffusion in the solid and in the air when the absorption of the reflected laser energy is included. The computed photothermal deflections with reflection of the heating laser energy included are shown in Fig. 2.10. These data show larger computed photothermal deflection amplitudes compared to those omitting reflection of the heating laser beam. When reflection of the heating laser beam is included, the maximum amplitude of the computed photothermal deflection for cavity heating becomes 250% higher than for plane surface heating for copper and about 55% and 35% higher for lead and stainless steel, respectively. These results are more consistent with the experimental data although the computed photothermal deflection amplitudes for lead and stainless steel are slightly larger than the experimental data. For lead, this difference may be due to the difference of the aspect ratio of the cavity used in the computation, 0.5, and of the sample in the experiment, 0.32. For stainless steel, the difference may be related to the unknown thermophysical properties of the experimental sample. Irradiation of the reflected heating laser beam onto the cavity wall may also be the reason for the slow decrease of the photothermal deflection amplitude of the lead sample with an aspect ratio of 0.89 in Fig. 2.4. Because the amplitude of the photothermal deflection response for a plane surface decreases exponentially with distance from the surface and with the modulation frequency, it decreases very fast as shown in the figure. The photothermal deflection amplitude for a cavity, however, drops less sharply possibly because of the enhanced effect of the reflected heating laser beam.

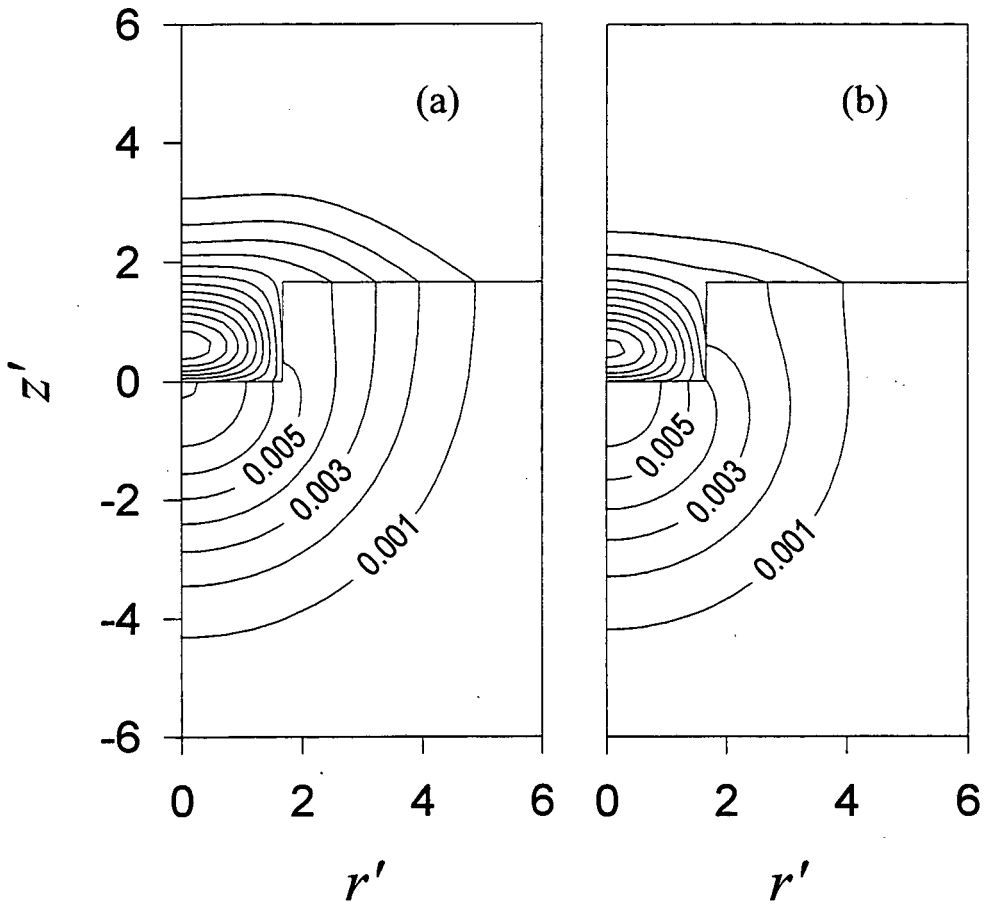

Fig. 2.9 Temperature distributions in the target and in the surrounding air for copper at $\tau=0.7\tau_0$ (a) with and (b) without the absorption of the reflected laser energy on the cavity wall

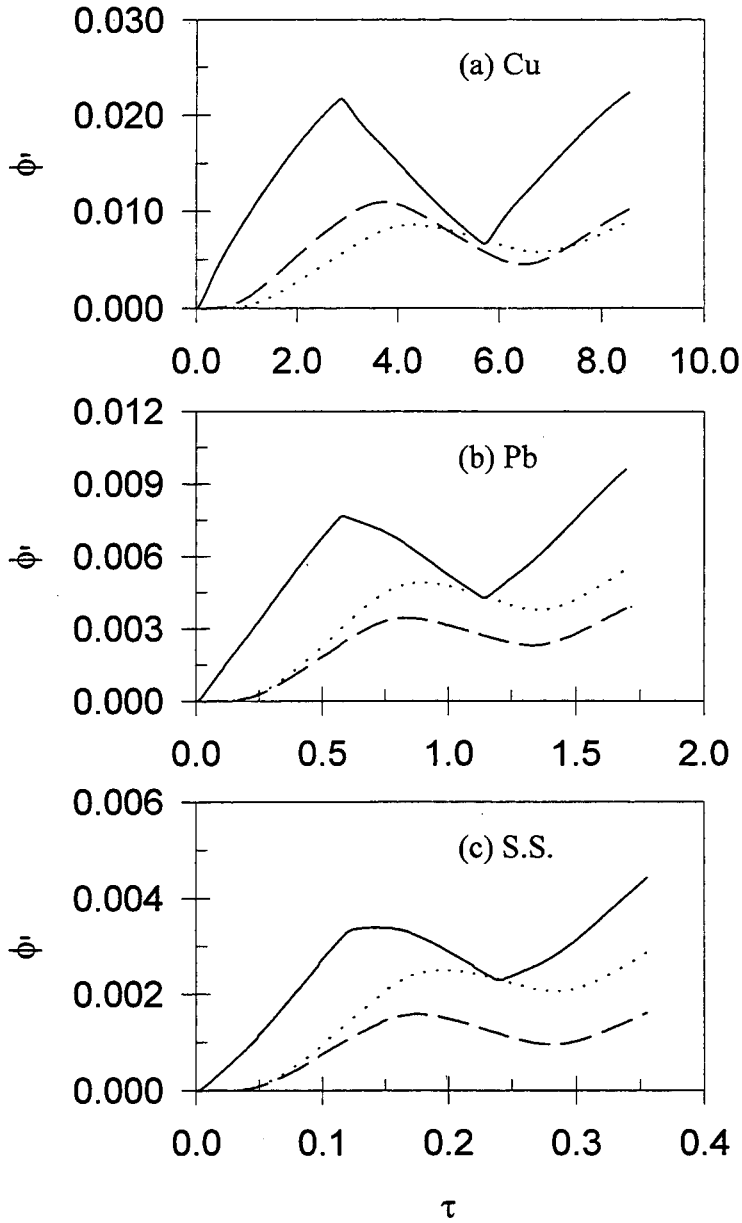

Fig. 2.10 Computed photothermal deflections for (a) copper, (b) lead, and (c) stainless steel when reflection of the heating laser beam is included (z_0'=2.17, solid line: for a cavity including reflection, dashed line: for a cavity without reflection, dotted line: for a plane surface)

From the above results, it appears that reflection of the heating laser beam inside the cavity is important in determining the energy transfer and the photothermal deflection response. A large amount of the reflected heating laser beam is absorbed by the cavity surface, which would be scattered away if there is no cavity. Thus we conclude that a cavity in a solid surface enhances the energy coupling between a laser beam and a solid.

2.5 Conclusion

Using the photothermal deflection technique, the effects of a cylindrical cavity in a metal surface on the energy coupling of a laser beam with a solid during laser heating were investigated. The amplitude and time response of the measured and computed photothermal deflection responses were examined for copper, lead, and stainless steel, and for cavities with different aspect ratios. Reflection of the heating laser beam inside the cavity is found to increase the photothermal deflection amplitude significantly and the increase becomes larger when the thermal diffusivity of the solid is larger. Also the numerical model which was used to compute temperature and photothermal deflection predicted the experimental results more closely when reflection of the heating laser beam inside the cavity was included. The overall energy coupling between a heating laser beam and a solid is enhanced by a cavity.

References

[1] E. N. Sobol, *Phase transformations and ablation in laser-treated solids,* (Wiley, New York, 1995)

[2] J. Dowden, N. Postacioglu, M. Davis, and P. Kapadia, "A Keyhole model in penetration welding with a laser", J. Phys. D: Appl. Phys. Vol. 20, 1987, pp. 36-44

[3] J. Dowden, P. Kapadia, and N. Postacioglu, "An analysis of the laser-plasma interaction in laser keyhole welding", J. Phys. D: Appl. Phys. Vol. 22, 1989, pp.741-749

[4] J. Trappe, J. Kroos, C. Tix, and G. Simon, "On the shape and location of the keyhole in penetration laser welding", J. Phys. D: Appl. Phys.Vol. 27, 1994, pp. 2152-2154

[5] Y. Arata and I. Miyamoto, "Laser welding", Technocrat, Vol. 11, No. 5, 1978, pp.33-42

[6] A. Kar, T. Rockstroh, and J. Mazumder, "Two-dimensional model for laser-induced materials damage: Effects of assist gas and multiple reflections inside the cavity", J. Appl. Phys. 71 (6), 1992, pp. 2560-2569

[7] A. C. Boccara, D. Fournier, and J. Badoz, "Thermo-optical spectroscopy:Detection by the "mirage effect", Appl. Phys. Lett. 36 (2), 1980, pp. 130-132

[8] M. A. Shannon, A. A. Rostami, R. E. Russo, "Photothermal deflection measurements for monitoring heat transfer during modulated laser heating of solids", J. Appl. Phys. 71 (1), 1992, pp. 53-63

[9] M. A. Shannon, B. Rubinsky, R. E. Russo, "Detecting laser-induced phase chage at the surface of solids via latent heat of melting with a photothermal deflection technique" J. Appl. Phys. 75 (3), 1994, pp. 1473-1485

[10] J. A. Sell, D. M. Heffelfinger, P. Ventzek, and R. M. Gilgenbach, "Laser beam deflection as a probe of laser ablation of materials", Appl. Phys. Lett. 55 (23), 1989, pp. 2435-2437

[11] E. Heidecker, J. H. Schafer, J. Uhlenbusch, and W. Viol, "Time-resolved study of a laser-induced plasma by means of a beam-deflection technique", J. Appl. Phys. 64 (5), 1988, pp. 2291-2297

[12] C. L. Enloe, R. M. Gilgenbach, and J. S. Meachum, "Fast, sensitive laser deflection system suitable for transient plasma analysis", Rev. Instrum. 58 (9), 1987, pp. 1597-1600

[13] W. B. Jackson, N. M. Amer, A. C. Boccara, and D. Fournier, "Photothermal deflection spectroscopy and detection", Applied Optics, Vol. 20, No. 8, 1981, pp. 1333-1344

[14] A. Salazar, A. Sanchez-Lavega, and J. Fernandez, "Theory of thermal diffusivity determination by the mirage technique in solids", J. Appl. Phys. 65 (11), 1989, pp. 4150-4156

[15] J. R. Welty, C. E. Wicks, and R. E. Wilson, *Fundamentals of momentum, heat, and mass transfer*, 2nd ed. (Wiley, New York, 1976)

[16] *Thermophysical properties of matter*, Vol. 10, edited by Y. S. Touloukian (Plenum, New York, 1970)

[17] J. F. Eloy, in *Laser ablation of electronic materials*, edited by E. Fogarassy and S. Lazare, North-Holland, 1992, pp. 3-18

[18] R. Siegel and J. R. Howell, *Thermal radiation heat transfer*, 2nd ed. (McGraw-Hill, New York, 1981)

[19] *Thermophysical properties of matter*, Vol. 7, edited by Y. S. Touloukian and D. P. Dewitt, (Plenum, New York, 1970)

Chapter 3

Numerical analysis of the pulsed laser heating of metals

3.1 Introduction

The increasing importance of laser ablation technology in numerous applications have prompted extensive theoretical and experimental study of the phenomena. While experimental measurements can provide the most direct information that possibly reveal the actual phenomena, it is possible that the measurement of physical quantities during the extremely rapid laser ablation process maybe either impossible or severely limited by experimental conditions. On the other hand, a numerical simulation with rigorous mathematical modeling of the actual process can be very useful to investigate both the quantitative and qualitative features of the process with great flexibility in simulation conditions. With a well established numerical model, a systematic approach for time or space resolved parameters is readily available. A mathematical model based on reasonable assumptions can provide useful information about the fundamental behavior and qualitative features of the laser ablation process. Therefore, numerical studies have been an important method for investigating the laser ablation process. However, a complete mathematical representation of the laser ablation process, which is fully nonlinear, has not been developed, hence a numerical modeling also has its limitations and requires further improvement.

In this chapter, pulsed laser heating of metal targets is studied numerically. Because of the inherent complexity of the rapid laser heating problems, analytical modeling of laser heating of solids is mostly limited to predictions of temperature rise of the target for simple geometries [1-4]. Therefore numerical modeling is more often employed for most of the transient, multidimensional, phase change, and/or variable property problems [5-7]. Theoretical studies of pulsed laser heating of solids are mostly interested either in the basic processes of material removal from the target or in the characteristics of the laser induced gasdynamic flow of the vapor. Possible mechanisms of material removal during laser heating of solids include thermal evaporation, electronic excitation, or thermomechanical expulsion of droplets or large particles [8]. Understanding the dynamics of laser induced vapor flow has been one of the key issues in laser-matter interaction studies [9-13]. For example, the time-of-flight of individual species in the laser generated vapor or the propagation of a laser induced shock wave is a direct consequence of the gasdynamic flow. The correct understanding of the characteristics of the gasdynamic flow is critical for the interpretation of the experimental data [8]. While laser heating of metal targets under vacuum or gaseous environments is equally important, theoretical work which includes the effects of the ambient gas on the vaporization process are limited. Knight [11] developed an approximate one dimensional model for laser-induced evaporation of a metal surface with ambient pressures ranging from vacuum to 1 atm. He showed that the flow and target conditions during laser evaporation can be described as a function of metal vapor velocity for a steady constant material removal from the surface. Transient evaporation with temporally non-uniform

laser energy was qualitatively described. Igoshin and Kurochkin [14] investigated the influence of ambient pressures ranging from 1-125 atm on the vapor properties for laser evaporation. Aden et al. [15] presented a one dimensional model that treated the expansion of the vapor into the surrounding gas as a Riemann problem. A threshold laser intensity was defined where the evaporation process is independent of the ambient pressure. Ho et al. [16] made a detailed study of target phase change and vapor expansion into an ambient gas for pressures from 10^{-4} to 1 atm. In subsequent work, Ho et al. [17] solved the equation of radiative transfer coupled to the equations of gasdynamic flow. The formation of a thin vapor layer above the target surface and the importance of thermal radiation for plume cooling were demonstrated. Kelly and co-workers performed extensive studies of the laser induced gasdynamic flow in vacuum and in gaseous environment [13,18-22]. In their studies, the gasdynamic flow is described by three possible models, i.e. effusion model, recondensation model, and outflow model [19]. Their results emphasize the importance of the gasdynamic flow in the interpretation of the measured data, such as time-of-flight or the angular distribution of particles.

In the present work, the main features of unsteady vaporization of a metal target and the subsequent motion of the vapor are investigated. The effect of the ambient gas pressure on these processes is addressed. A one dimensional numerical analysis of the heating of the target and the motion of the vapor is carried out. For short laser pulses with laser spot sizes of the order of a few mm, thermal penetration into the target is much smaller than the laser heated region on the surface, which is consistent with the one dimensional analysis for the uniform target heating of the present study. The effect of the

ambient pressure on the velocity of the vapor leaving the non-equilibrium regime close to the target surface, the Knudsen layer, is studied. Conditions are obtained when the velocity of the vapor leaving the Knudsen layer is equal to the sound velocity. The vapor and the surrounding gas are assumed to be transparent to the incoming laser radiation, which is valid for low laser power densities. For high laser power densities, vapor from the target interacts with the laser radiation and plasma shielding becomes important [23-25]. Mao and Russo [25] showed that the power density at which plasma shielding begins is about 0.3 GW/cm^2. The present study is for laser power densities below this value and thus the vapor is assumed to be transparent to the incoming laser light.

A schematic diagram for laser induced evaporation is shown in Fig. 3.1. All of the vapor molecules leaving the liquid-vapor interface during laser evaporation have velocity components away from the surface at the interface and develop an equilibrium normal velocity distribution as they move away. The distance over which the normal velocity distribution of the vapor molecules transforms from a non-equilibrium to an equilibrium distribution is called the Knudsen layer. A Knudsen layer forms in a laser induced gasdynamic flow regardless whether the evaporation is into a vacuum or into a gaseous environment. The importance of the Knudsen layer is well described by Kelly [13]. The vapor flow above the Knudsen layer is considered to be a gasdynamic flow where the continuum approximation can be made. The Knudsen layer is treated as a discontinuity for the gasdynamic flow and provides boundary conditions for the gasdynamic flow. Note that the relative scale of the Knudsen layer in Fig. 3.1 is extremely exaggerated. The shock wave and the contact surface propagate to the right in Fig. 3.1.

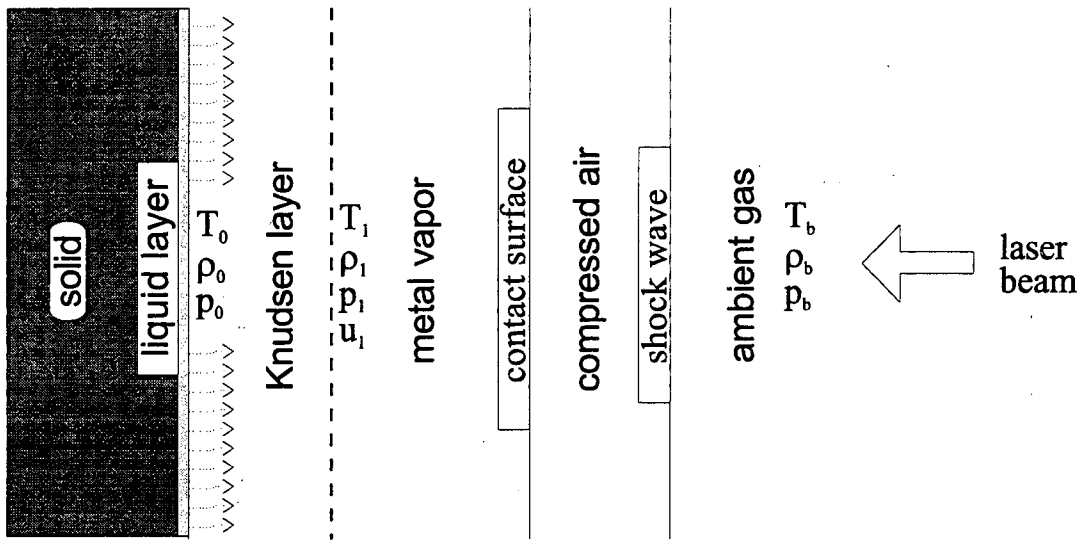

Fig. 3.1 Schematic diagram of the laser induced evaporation

3.2 Theoretical Modeling

3.2.1 Solid Heating

A thermal evaporation model is used for the present study as the primary mechanism of material removal from the target. Droplets or bulk material are not assumed to leave the target surface. For metal targets, the absorption length of the laser light is on the order of 10^{-6} cm [26] and thus it is assumed that the laser light is absorbed completely at the target surface. The one dimensional form of the energy equation, Eq.(3.1), is solved for the target temperature. The detailed progress of melting and the temperature distribution within the melt regime are not explicitly solved. The thermal conductivity and the thermal diffusivity are functions of temperature in Eqs. (3.1) and (3.2) but other properties are considered to be independent of temperature.

The energy equation for the target is;

$$\frac{\partial T(x,t)}{\partial t} - v_p \frac{\partial T(x,t)}{\partial x} = \frac{\partial}{\partial x}\left(\alpha(T)\frac{\partial\ T(x,t)}{\partial x}\right) \qquad (3.1)$$

And the boundary condition at the target surface becomes;

$$k(T)\frac{\partial T(0,t)}{\partial x} = \rho_l L_{ev} v_p - (1-\mathcal{R})I(t) \qquad (3.2)$$

where $T(x,t)$ is the temperature of the target, $\alpha(T)$ is thermal diffusivity, $k(T)$ is thermal conductivity, ρ is density of the liquid, L_{ev} is the sum of the heat of fusion and the heat of vaporization, and $\mathcal{R}$ is the reflectivity of the target surface at the wavelength of the laser light. Also $x=z-v_p t$ is the moving coordinate relative to the phase interface, t is time, and

v_p is the velocity of the liquid-vapor phase interface. The laser energy incident on the target surface, $I(t)$, is assumed to have a temporally changing profile.

In order to determine the velocity of the liquid-vapor phase interface, the vapor flow inside the Knudsen layer should be considered. A simple expression for the mass flux of vapor leaving the surface in thermal equilibrium [27,28,29] is the Hertz-Knudsen formula [30];

$$\dot{m}_{+,0} = p_0(T_0)\left(\frac{m_a}{2\pi k_B T_0}\right)^{\frac{1}{2}} \tag{3.3}$$

where m_a is the atomic mass of the target material, k_B is the Boltzmann constant, T_0 is the temperature of the target surface, and $P_0(T_0)$ is the saturation pressure of the vapor at the temperature T_0. The saturation pressure of the vapor, $P_0(T_0)$, is obtained from the Clausius-Clapeyron equation;

$$P_0(T_0) = P_\infty \exp\left[\frac{H_{ev}}{R_v T_{ev,\infty}}\left(1-\frac{T_{ev,\infty}}{T_0}\right)\right] \tag{3.4}$$

where P_∞ is the atmospheric pressure, R_v is the gas constant of the vapor, $T_{ev,\infty}$ is the vaporization temperature of the target material at P_∞, and H_{ev} is the heat of vaporization.

The velocity distribution function of the vapor molecules leaving the liquid-vapor phase interface can be assumed to be half-Maxwellian if the liquid is near thermodynamic equilibrium and transforms into a Maxwellian distribution at the edge of the Knudsen layer due to collisions [13,18]. Since the molecules scattered back by collisions are returning to the interface, not all of the vapor molecules given by Eq. (3.3) leave the surface. The mass flux of the back scattered molecules is obtained by solving

conservation equations for the Knudsen layer with a properly selected velocity distribution functions. The following method was originally employed by Anisimov [31] and also used by Knight [11] and Ytrehus [32]. The conservation of mass, momentum, and energy within the Knudsen layer can be written as;

$$\begin{aligned} \int \xi f dV &= \text{mass flux} \\ \int \xi^2 f dV &= \text{momentum flux} \\ \int \tfrac{1}{2}(\xi^2+\eta^2+\zeta^2)\xi f dV &= \text{energy flux} \end{aligned} \tag{3.5}$$

where ξ, η, and ζ represent the velocity components of the vapor particles with ξ equal to the velocity component normal to the vaporizing surface and $dV=d\xi d\eta d\zeta$, the volume element in velocity space. The Maxwellian velocity distribution at the outer edge of the Knudsen layer where local equilibrium is assumed to be established is written as

$$f_1 = \rho_1 (2\pi R_v T_1)^{-3/2} \exp\left[-\frac{(\xi-u_1)^2+\eta^2+\zeta^2}{2R_v T_1}\right] \tag{3.6}$$

where ρ_1, u_1, and T_1 are the local density, velocity, and temperature, respectively. The subscript 1 denotes the outer edge of the Knudsen layer. At the liquid-vapor phase interface, denoted by the subscript 0, the distribution function is assumed to have the following form:

$$f_0 = \begin{cases} \rho_0 (2\pi R_v T_0)^{-3/2} \exp\left[-\dfrac{\xi^2+\eta^2+\zeta^2}{2R_v T_0}\right] , & \xi > 0 \\ \beta f_1 , & \xi < 0 \end{cases} \tag{3.7}$$

In the second expression of Eq. (3.7), the velocity distribution function of the particles scattered toward the phase interface is assumed to be proportional to that at the outer boundary. By solving Eq. (3.5) with Eqs. (3.6) and (3.7), the mass flux of the back scattered vapor molecules to the interface is given by

$$\dot{m}_{-,0} = \beta\rho_1\sqrt{\frac{R_v T_1}{2\pi}}[e^{-m^2} - \sqrt{\pi}\, m erfc(m)] \tag{3.8}$$

where $m=(\gamma_v/2)^{1/2}M_1$, $erfc(m) = (2/\sqrt{\pi})\int_m^{\infty} e^{-s^2} ds$ is the complementary error function, and γ_v is the specific heat ratio of the vapor. The Mach number of the vapor at the edge of the Knudsen layer is

$$M_1 = \frac{u_1}{\sqrt{\gamma_v R_v T_1}} \tag{3.9}$$

With Eqs. (3.3) and (3.8), the velocity of the phase interface can be expressed as

$$v_p = \frac{(\dot{m}_{+,0} - \dot{m}_{-,0})}{\rho_l} \tag{3.10}$$

where $\rho_l = \rho_{m.p.} - \Lambda(T_0 - T_{m.p.})$ is the density of the liquid at the surface. In the expression for ρ_l, Λ is a constant and the subscript *m.p.* denotes the melting point.

In the conservation equations, Eq. (3.5), there are four unknowns, ρ_1, u_1, T_1, and β, with three equations. To obtain an additional condition, Anisimov [31] assumed that u_1 is equal to the local speed of sound. On the other hand, Knight [11] and Ytrehus [32] selected one variable as a parameter and solved the equations in terms of the selected parameter. Knight treated M_1 as the free parameter while Ytrehus chose the pressure ratio defined by p_1/p_0 as the variable parameter. The solution for Knudsen layer obtained by

Knight [11, Eq. (6)] is adopted in this study. These equations are rewritten below without the derivation;

$$\frac{T_1}{T_0}=\left[\sqrt{1+\pi\left(\frac{\gamma-1}{\gamma+1}\frac{m}{2}\right)^2}-\sqrt{\pi}\frac{\gamma-1}{\gamma+1}\frac{m}{2}\right]^2$$

$$\frac{\rho_1}{\rho_0}=\sqrt{\frac{T_0}{T_1}}\left[\left(m^2+\frac{1}{2}\right)\exp(m^2)erfc(m)-\frac{m}{\sqrt{\pi}}\right]$$
$$+\frac{1}{2}\frac{T_0}{T_1}\left[1-\sqrt{\pi}m\exp(m^2)erfc(m)\right] \qquad (3.11)$$

$$\frac{p_1}{p_0}=\frac{\rho_1 T_1}{\rho_0 T_0}$$

$$\beta=\left[(2m^2+1)-m\sqrt{\frac{\pi T_0}{T_1}}\right]\exp(m^2)\frac{\rho_0}{\rho_1}\sqrt{\frac{T_0}{T_1}}$$

3.2.2 Gasdynamics of the Vapor

The major properties of interests in laser induced gasdynamic flow are the density, velocity, temperature, and pressure of the vapor. The variation of these properties are obtained by solving the one dimensional compressible flow equations for an inviscid fluid, the Euler equations [33];

$$\frac{\partial\rho}{\partial t}+\frac{\partial(\rho u)}{\partial x}=0$$

$$\frac{\partial(\rho u)}{\partial t}+\frac{\partial(\rho u^2+p)}{\partial x}=0 \qquad (3.12)$$

$$\frac{\partial E}{\partial t}+\frac{\partial[(E+p)u]}{\partial x}=0$$

where ρ and u are the density and the velocity of the vapor in the direction normal to the target surface, respectively. E is the total energy per unit volume described by

$$E = \rho e + \tfrac{1}{2}\rho u^2 \tag{3.13}$$

where e is the internal energy per unit mass. The vapor and the ambient gas are assumed to be polytropic gases and hence the pressure term can be written as

$$p = (\gamma - 1)\rho e \tag{3.14}$$

Eq. (3.12) can be rewritten in vector form as

$$\frac{\partial \boldsymbol{U}}{\partial t} + \frac{\partial \boldsymbol{F}(\boldsymbol{U})}{\partial x} = 0 \tag{3.15}$$

where

$$\boldsymbol{U} = \begin{pmatrix} \rho \\ \rho u \\ E \end{pmatrix}, \qquad \boldsymbol{F}(\boldsymbol{U}) = \begin{pmatrix} \rho u \\ \rho u^2 + p \\ (E + p)u \end{pmatrix}$$

The boundary conditions at x=0 while evaporation of the target material continues are taken from the solutions of the solid heating and Knudsen layer analysis. When vaporization ceases, the reflecting wall conditions [16,22] are applied at the solid boundary, i.e. $\partial\rho/\partial x = \partial p/\partial x = 0$ and u=0. The gasdynamic flow described in this section is in principle similar to the effusion model of Kelly and Braren [19].

3.3 Numerical Methods

3.3.1 Solid Heating

Eq. (3.1) is solved for the target temperature utilizing a finite difference method

with non-uniform grids. For the region where temperature is over the melting temperature, thermophysical properties for the melt are used without explicitly solving equations for the melt region. The velocity of the liquid-vapor phase interface in Eq. (3.2), v_p, remains zero until the surface temperature of the target reaches its vaporization temperature. When the temperature of the target surface rises above the vaporization temperature of the material, equations (3.1), (3.2), and (3.10) are solved iteratively. The additional condition to solve the conservation equations for the Knudsen layer, Eq. (3.5), is found for the Mach number of the vapor at the edge of the Knudsen layer, M_1. As the surface temperature, T_0, drops below the vaporization temperature, v_p is again set to zero.

3.3.2 Gasdynamics of the Vapor

Eq. (3.12) (or equivalently Eq. (3.15)) represents a set of nonlinear hyperbolic equations and the solution of these equations contains discontinuities, such as shock waves and contact surfaces. An effective numerical technique to solve these types of equations is Glimm's method [34].

In order to use Glimm's method, a numerical technique for solving a Riemann problem is necessary [35,36,37]. Riemann problem is a simplest type of initial value problem for which a discontinuity appears and can be described for $\boldsymbol{U}(x,t)$ in Eq. (3.15) as;

$$\boldsymbol{U}(x,0) = \begin{cases} S_l = (\rho_l, u_l, p_l) & , \quad x < 0 \\ S_r = (\rho_r, u_r, p_r) & , \quad x \geq 0 \end{cases} \tag{3.16}$$

A schematic diagram of the solution of Eq. (3.16) is represented in Fig. 3.2, where ℓ_1 is a shock wave and the region between $\ell_{2,f}$ and $\ell_{2,b}$ is a centered rarefaction wave. S^* which extends from ℓ_1 to $\ell_{2,f}$ is a steady state region. The contact discontinuity $dx/dt=u^*$ separates the state S^* into two parts with possibly different values of ρ^*, but equal values of u^* and p^*. With the Riemann problem solver, Eq. (3.15) can be solved by Glimm's method as follows. Let the time and space increments be Δt and Δx. We assume that at time $n\Delta t$, $n \geq 0$, the approximate solution is constant on intervals of Δx and is denoted by

$$\begin{aligned} U(x, n\Delta t) &= w_{i+1}^n, \qquad x \geq (i+\tfrac{1}{2})\Delta x \\ &= w_i^n, \qquad x < (i+\tfrac{1}{2})\Delta x \end{aligned} \tag{3.17}$$

The solution at time step $(n+1)\Delta t$, $U(x,(n+1)\Delta t)=w_i^{n+1}$, is obtained by solving a succession of Riemann problems represented by Eq. (3.17). If the time step Δt is sufficiently small the waves (see Fig. 3.2) generated from adjacent Riemann problems will not intersect. The maximum time step satisfying this condition is determined by the Courant-Friedrichs-Lewy condition [34,35];

$$\Delta t \leq \frac{\Delta x}{2(\max|u_i| + a_i)} \tag{3.18}$$

where a_i is the local speed of sound at the location x_i. When the solutions of the Riemann problems along the whole x coordinate are combined, they form an exact solution for the initial data given by Eq. (3.17) within the time interval Δt. Denoting this exact solution to be $v(x,t)$, Glimm's method defines the solution at $(n+1)\Delta t$ to be

$$w_i^{n+1} = v((i-\tfrac{1}{2}+b^{n+1})\Delta x, (n+1)\Delta t) \tag{3.19}$$

where the coefficient b^{n+1} lies in the interval [0,1) [34].

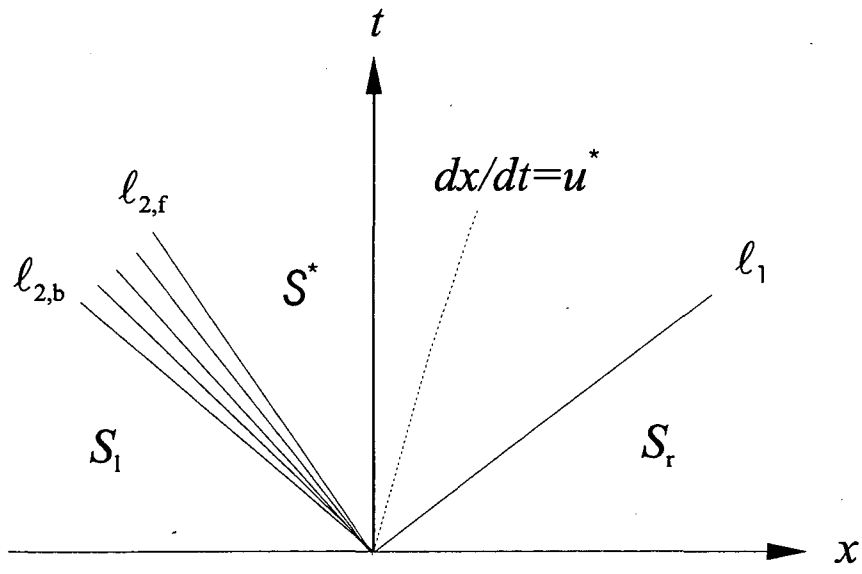

Fig. 3.2 Schematic diagram of the solution of a Riemann problem ($p_l > p_r$ in this figure).

3.4 Results and discussion

Aluminum is selected as the sample material for the calculation. Thermal properties of aluminum are given in Table 1 [38,39,40]. The constant, Λ, in the equation for the density of liquid aluminum is 0.35 [41]. The specific heat ratios of aluminum vapor which is assumed to be a monatomic gas and the ambient gas, air, are taken to be

Table 3.1. Thermophysical properties of Aluminum

Property	Unit	
density (Solid)	kg/m^3	2700.0
density (Melt)	kg/m^3	2370.0
thermal conductivity (Solid)	W/m K	$258.8-4.9\times10^{-2}T$
thermal conductivity (Melt)	W/m K	$56.96+4.98\times10^{-2}T-1.25\times10^{-5}T^2$ $+7.03\times10^{-10}T^3$
thermal diffusivity (Solid)	m^2/s	$1.12\times10^{-4}-4.72\times10^{-8}T$
thermal diffusivity (Melt)	m^2/s	$1.53\times10^{-5}+2.65\times10^{-8}T-5.63\times10^{-12}T^2$ $+3.18\times10^{-16}T^3$
enthalpy of melting	J/kg	396.30×10^3
enthalpy of vaporization	J/kg	10.52×10^6
melting temperature	K	933.0
boiling temperature (1 atm)	K	2793.0
atomic mass	kg/molecule	4.483×10^{-25}

5/3 [11,27] and 1.4, respectively. The initial temperature of the target is 300 K. The determination of the reflectivity requires careful consideration. First of all, the reflectivity of a metal surface during laser heating, in which the surface temperature varies easily over 3000 K, is not temperature independent. The reflectivity of metal surfaces is considered to decrease with temperature, especially at temperatures high enough to induce melting or evaporation [27,42]. The reflectivity of an aluminum surface at high temperature is not readily available. The values at low temperatures vary from 0.92 to 0.98 for laser beam wavelengths from 0.25 to 10.6 μm, respectively [43]. In this study the reflectivity of an aluminum surface is assumed to be equal to 0.9.

The sample surface is assumed to be heated by a single laser pulse of triangular shape [16,27]. The laser pulse duration, t_l, and the time at which the laser fluence reaches its maximum are assumed to be 30 and 10 ns, respectively. The corresponding laser power density, $I(t)$, can be represented by the following equation

$$I(t) = \begin{cases} \dfrac{2Ft}{t_l t_m} & 0 < t < t_m \\ \dfrac{2F(t_l - t)}{t_l(t_l - t_m)} & t_m < t < t_l \\ 0 & t_l < t \end{cases} \tag{3.20}$$

where F is the laser fluence ranging from 6.5 to 8.5 J/cm^2. The area of the laser heated region on the target surface is 1 mm^2. For the selected ranges of laser fluence, the laser power density becomes 2.2-2.8×10^8 W/cm^2, which is below the threshold power density for plasma shielding, 3×10^8 W/cm^2, reported by Mao and Russo [25].

For the present calculations, laser fluence of 6.1 J/cm^2 and a corresponding laser power density of 2×10^8 W/cm^2 appears to be the threshold for evaporation of the target. The threshold laser fluence calculated by Peterlongo et al. [27] and Ho et al.[16] for an aluminum targets was about 3.2 J/cm^2 for 30 ns laser pulse and 10 J/cm^2 for 26 ns pulse, respectively. In those studies, Peterlongo et al. used a constant reflectivity value of 0.79 while Ho et al. used also a constant value of 0.92. It can be shown that the difference among the calculated threshold values for evaporation is largely attributed to the reflectivity values selected for the computation. The variation of the threshold laser fluence for evaporation with respect to the surface reflectivity is shown in Fig. 3.3. Since the laser energy absorbed by the target is represented by $(1-\mathcal{R})I(t)$ in Eq. (3.2), the computed threshold fluence changes by a factor of 3 for the increase of surface reflectivity from 0.79 to 0.93. When the reflectivity is 0.79, the threshold fluence from the current model becomes 2.8 J/cm^2, which is close to the result by Peterlongo et al [27], i.e. 3.2 J/cm^2. Therefore it is confirmed that the threshold fluence for evaporation during laser heating of metal targets is strongly dependent upon the surface reflectivity, especially when the reflectivity is high. On the other hand, experimental results showed that the evaporation of aluminum target was observed for laser fluences much smaller than the above numerical values. As will be discussed in Chapter 4, the evaporation of aluminum targets was experimentally observed for laser fluence of about 2 J/cm^2 for excimer laser heating with pulse duration of about 30 ns. Evaporation of aluminum targets at this laser energy or lower was also reported by other researches [44,45]. Two possible reasons for the difference between the numerical and the experimental results

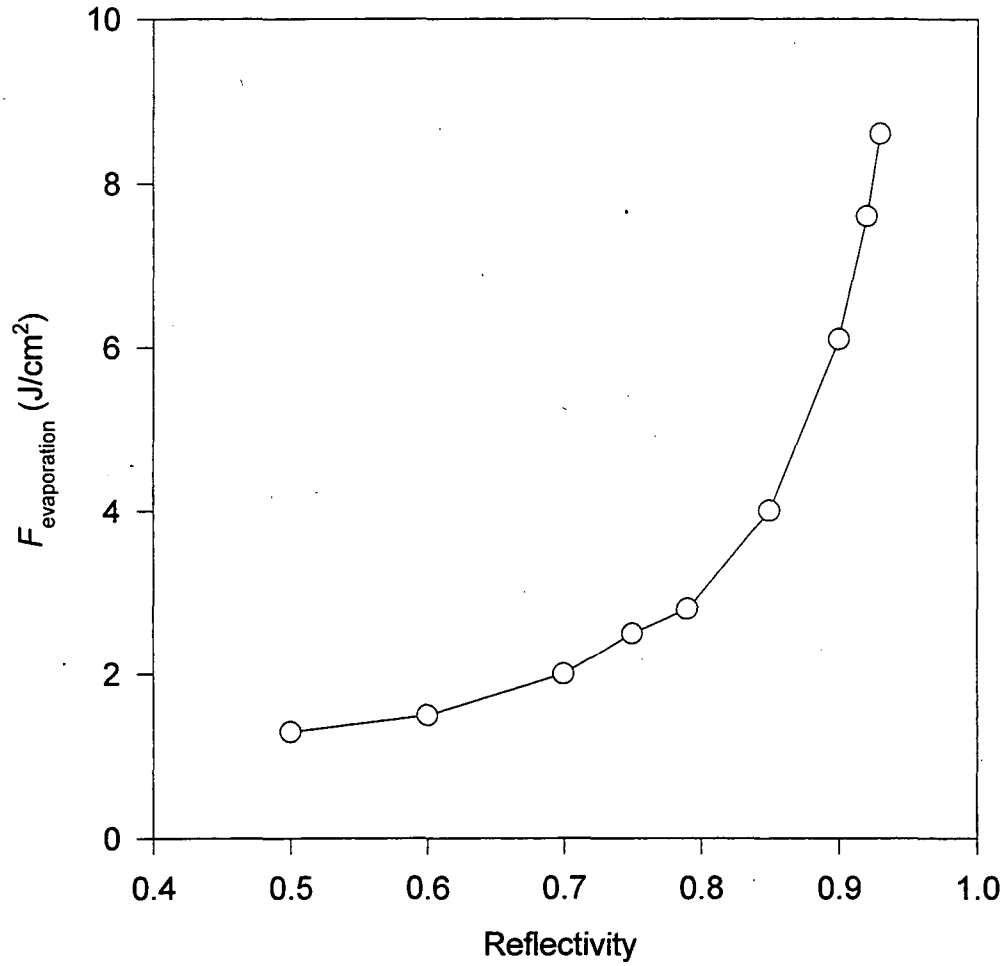

Fig. 3.3 Variation of the threshold laser fluence for evaporation with respect to the reflectivity of the (aluminum) target surface.

are postulated. First, the surface of aluminum targets used in experiments may have decreased reflectivity compared to pure aluminum. Surface oxidation or melting of the target may results in a decrease of reflectivity. Another possibility is the limitation of the thermal model to describe the real phenomena of laser evaporation. Nonthermal mechanisms of laser evaporation processes such as electronic excitation [46] may results in the enhancement of laser energy coupling. (All the numerical models mentioned above consider the thermal mechanism only.)

As mentioned earlier, the state of the vapor leaving the Knudsen layer can not be fully determined from the conservation equations in the Knudsen layer alone. The additional condition is obtained by considering the effect of the ambient pressure. On the other hand, Knight [11] and Aden et al. [15] showed that the velocity of the vapor leaving the Knudsen layer can not exceed the local sound velocity if the flow is one dimensional. Therefore M_1 varies between 0 and 1 in the following calculations.

When the vapor expands into a vacuum or the pressure of the vapor is significantly larger than the ambient pressure, the ambient pressure has little effect on the resulting vapor flow. For this condition, it is possible to assume that the velocity of the vapor at the edge of the Knudsen layer is sonic, i.e. M_1=1. Since the pressure perturbation outside of the Knudsen layer can not penetrate into the Knudsen layer when M_1 is equal to 1, the solid heating problem can be decoupled from the gasdynamic flow above the Knudsen layer. However, if the pressure of the vapor leaving the Knudsen layer is not large enough and is comparable to the ambient pressure, it is possible that the vapor can not develop a sonic velocity in the Knudsen layer; for this condition, the gasdynamic field

must be computed simultaneously with target heating. This situation can occur at the beginning of the evaporation process, when the saturation pressure of the vapor is not significantly larger than the ambient pressure.

Because of the complexity of these processes, an approximate procedure is utilized to determine the effects of the ambient pressure on the vapor velocity. The following assumptions are made: i) the flow above the Knudsen layer remains the same while the conditions in the target and the vapor within the Knudsen layer are computed for a short time period Δt^*, ii) the boundary conditions determined from the Knudsen layer analysis remain constant while the gasdynamic flow outside the Knudsen layer is calculated, iii) the vapor leaving the Knudsen layer is affected only by the pressure immediately outside the Knudsen layer, denoted by p_{g0}. Assumptions i) and ii) decouple the equations for target heating and the Knudsen layer from the equations for the gasdynamic flow for a short time period Δt^*. If the vapor velocity at the Knudsen layer is subsonic, information from the gasdynamic regime is carried to the Knudsen layer along the characteristic line, $dx/dt=u-a$, where u and a are the local flow and sound velocity, respectively. Assumption iii) excludes the influence of this information on the vapor exiting the Knudsen layer. When assumption iii) is made, the vapor leaving the Knudsen layer is affected only by the pressure p_{g0} and the velocity of the vapor is limited only by this pressure. The total momentum of the vapor exiting the Knudsen layer, denoted by $\boldsymbol{M}$, can be written as

$$\begin{aligned} \boldsymbol{M} &= \rho_1 u_1^2 + p_1 \\ &= p_0(\gamma_v M_1^2 + 1)[f_1(M_1) f_2(M_1)] \end{aligned} \tag{3.21}$$

where f_1 and f_2 are T_1/T_0 and ρ_1/ρ_0 which are given in Eq. (3.11), respectively. The total momentum $\boldsymbol{M}$ decreases with Mach number M_1, see Fig. 3.4. The vapor can expand out of the Knudsen layer only when $\boldsymbol{M}>p_{g0}$ is satisfied and this is achieved when $u_1<u_{1,max}$, where

$$u_{1,\max} = \sqrt{(p_{g0} - p_1) / \rho_1} \tag{3.22}$$

The relationship between the maximum Mach number, $M_{1,max}=u_{1,max}/a_1$ and the pressure p_{g0} is obtained by solving iteratively the equations for target heating and the Knudsen layer and those for the gasdynamic flow. Specifically, when the target surface reaches the boiling temperature: 1) solve the equations for the heating of the target and Knudsen layer to find new states satisfying the equation for $u_{1,max}$ for a given p_{g0}. The value of p_{g0} is first assumed to be the ambient pressure, p_b. 2) solve the gasdynamic equations using the new states obtained from step 1) as the boundary conditions to find a new value of p_{g0} after Δt^*.

The variation of $M_{1,max}$ from the beginning of evaporation to the time when $M_{1,max}$ becomes 1 is shown in Fig. 3.5 for different ambient pressure, p_b, where F is equal to 7.5 J/cm^2. For this laser fluence, target surface reached the vaporization temperature after 10.72 ns after the beginning of the laser irradiation. When the ambient pressure is sufficiently small, 0.1 atm in this case, $M_{1,max}$ becomes equal to 1 from the beginning of the evaporation; consistent with the previous discussion that M_1 can be set equal to unity for evaporation into a vacuum or into a small ambient pressure. When p_b is large, 1 atm in this case, $M_{1,max}$ increases with time until it reaches unity. For intermediate values of the

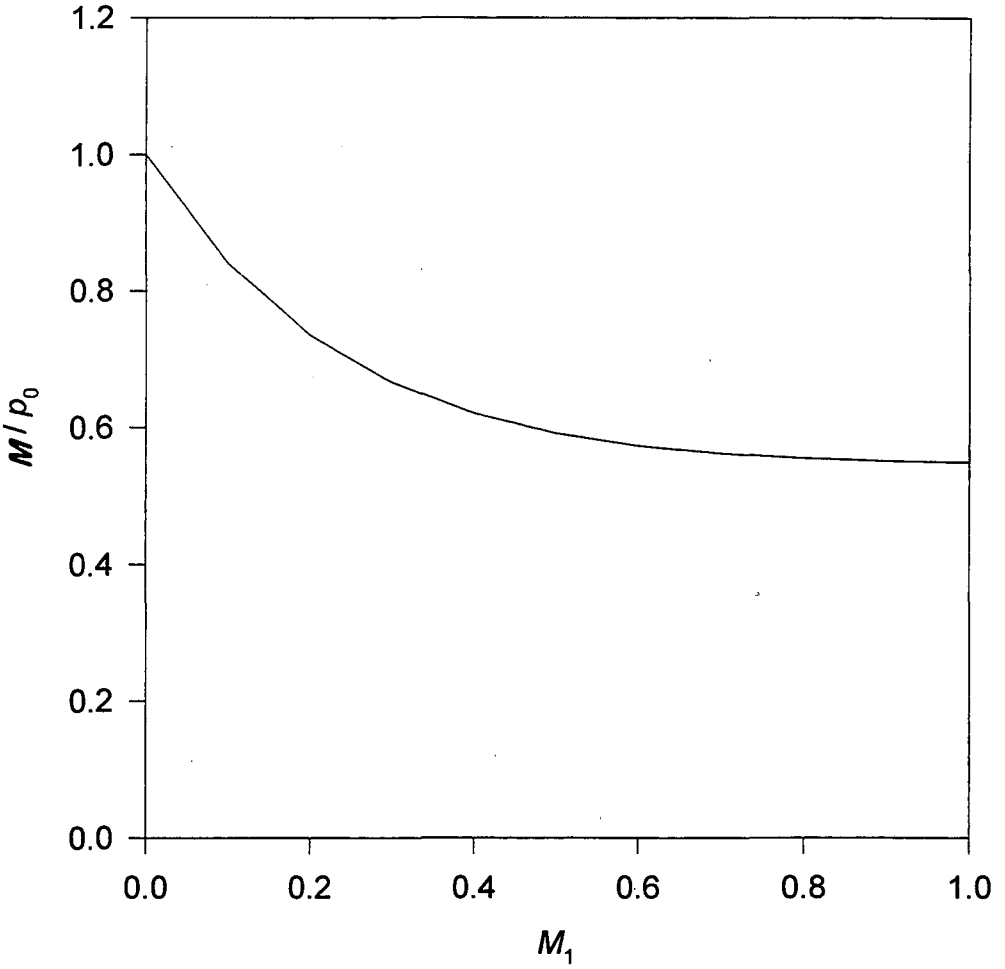

Fig. 3.4 Variation of the total momentum of the vapor leaving the Knudsen layer, $\boldsymbol{M}$ in Eq. (3.21), with respect to the Mach number of the vapor at the edge of the Knudsen layer, M_1. (Normalized by the saturation pressure of the vapor at the target surface)

ambient pressure, the variation of $M_{1,max}$ with time is divided into three regimes; a sharp decrease in the very beginning of evaporation, then a linear increase to about 0.3 which is followed by a rapid increase to 1. The sharp decrease of Mach number at the beginning of evaporation is the result of the sudden increase of the pressure in the gasdynamic regime just outside the Knudsen layer due to compression of the ambient gas and to the accumulation of the vapor from the target. Fig. 3.6(a) shows the density distribution in the gasdynamic regime very close to the edge of the Knudsen layer. The density profiles are propagating to the right with time in Fig. 3.6(a); the ambient pressure is 0.4 atm. Until t=11.2 ns the density profiles show the same pattern, i.e. a sharp increase in density at the propagating front and then a linear increase to the boundary. The propagating front where the sharp density increase occurs is the location of the shock wave. The following linear increase is attributed to the increased pressure of the vapor from the target. At t=11.2 ns, another discontinuity appears, i.e., a sharp decrease of density at the boundary (cf. Figs. 3.6(a) and (b)). It is believed that this second discontinuity is the contact surface that separates the ambient gas and the vapor from the target. Figs. 3.6(a) and (b) imply that the vapor expansion at the very early stage is hindered by the ambient gas of large pressure and the flow of the vapor into the gasdynamic region is delayed until the vapor acquires a sufficient pressure. After the vapor starts to flow into the ambient gas region, the rate of the pressure increase at the boundary of the gasdynamic regime, p_{g0}, decreases slightly while the saturation pressure of the vapor at the target surface continues to rise at the same rate (Fig. 3.7). This increased pressure difference enables the vapor to overcome the pressure outside the Knudsen layer with less decrease of its velocity. Note that $M_{1,max}$

increases rapidly with time after the appearance of the contact surface (Fig. 3.5). The times for the contact surface to appear in the gasdynamic regime and for $M_{1,max}$ to reach unity are shown in Fig. 3.8. For both cases the times increase almost linearly with increasing p_b, which is consistent with the above result that the vapor flow is hindered by the ambient gas. For a larger ambient pressure a longer time is expected for the vapor to develop a sufficient pressure.

The maximum ambient pressure that is allowed to keep $M_{1,max}$ equal to unity from the beginning of the evaporation, denoted by $p_{b,max}$, is shown in Fig. 3.9. For ambient pressures smaller than $p_{b,max}$, $M_{1,max}$ is always equal to 1 during the evaporation for the corresponding laser fluence. It appears that $p_{b,max}$ is not changing very much with laser fluence.

For most of the vapor flow analyses including the Knudsen layer, for example, the prediction of target surface temperature using the vapor velocity at the Knudsen layer, it is generally assumed that the Knudsen layer forms in zero time from the beginning of evaporation and the velocity of the vapor at the Knudsen layer is equal to the local sound velocity [11,19]. From the above results, it is found that this assumption is valid only when the ambient pressure is sufficiently small.

On the other hand, the temporal variation of $M_{1,max}$ for various laser fluences showed that $M_{1,max}$ does not increase to unity after the initial decrease when the laser energy is too small. An example is shown in Fig. 3.10 for which p_b is equal to 0.5 atm. The variation of $M_{1,max}$ for F=6.5 J/cm^2 shows that the Mach number of the vapor leaving the Knudsen layer does not increase to unity during the evaporation. It is often assumed

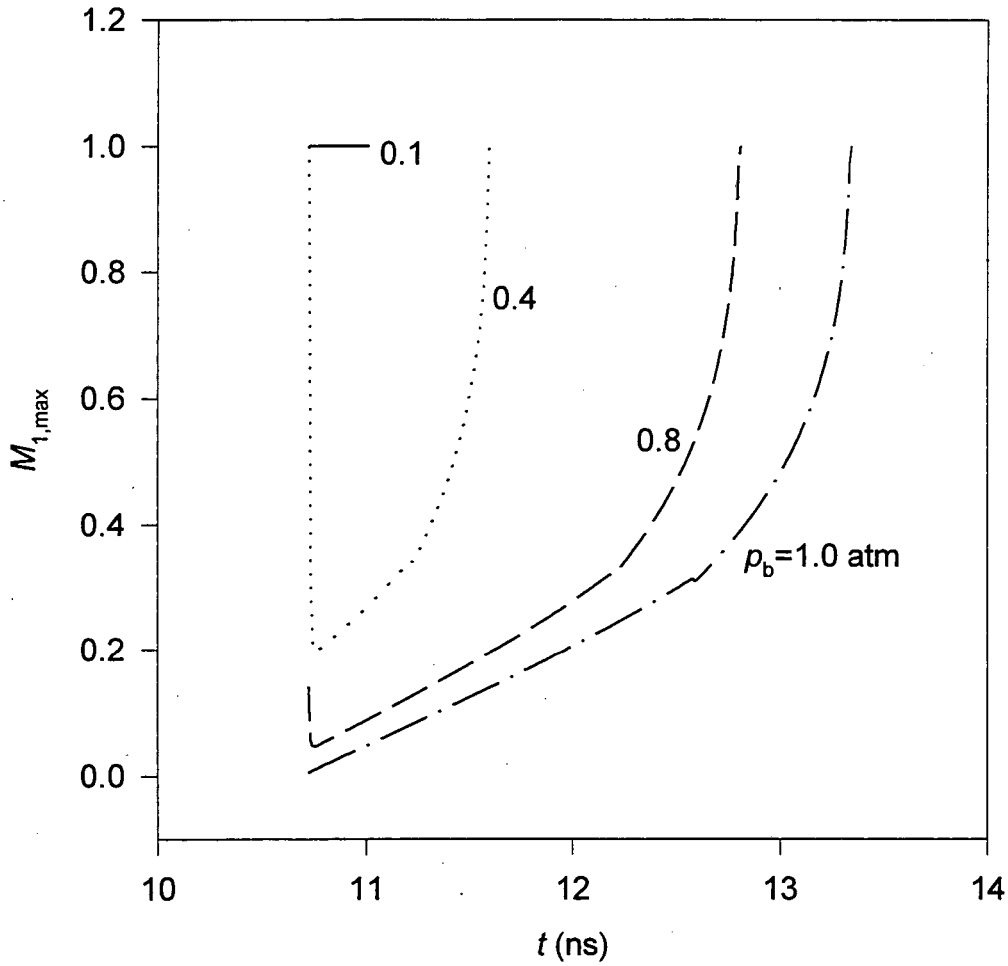

Fig. 3.5 Variation of the maximum Mach number of the vapor at the edge of the Knudsen layer for different ambient pressures (vaporization started at t=10.72 ns; F=7.5 J/cm^2)

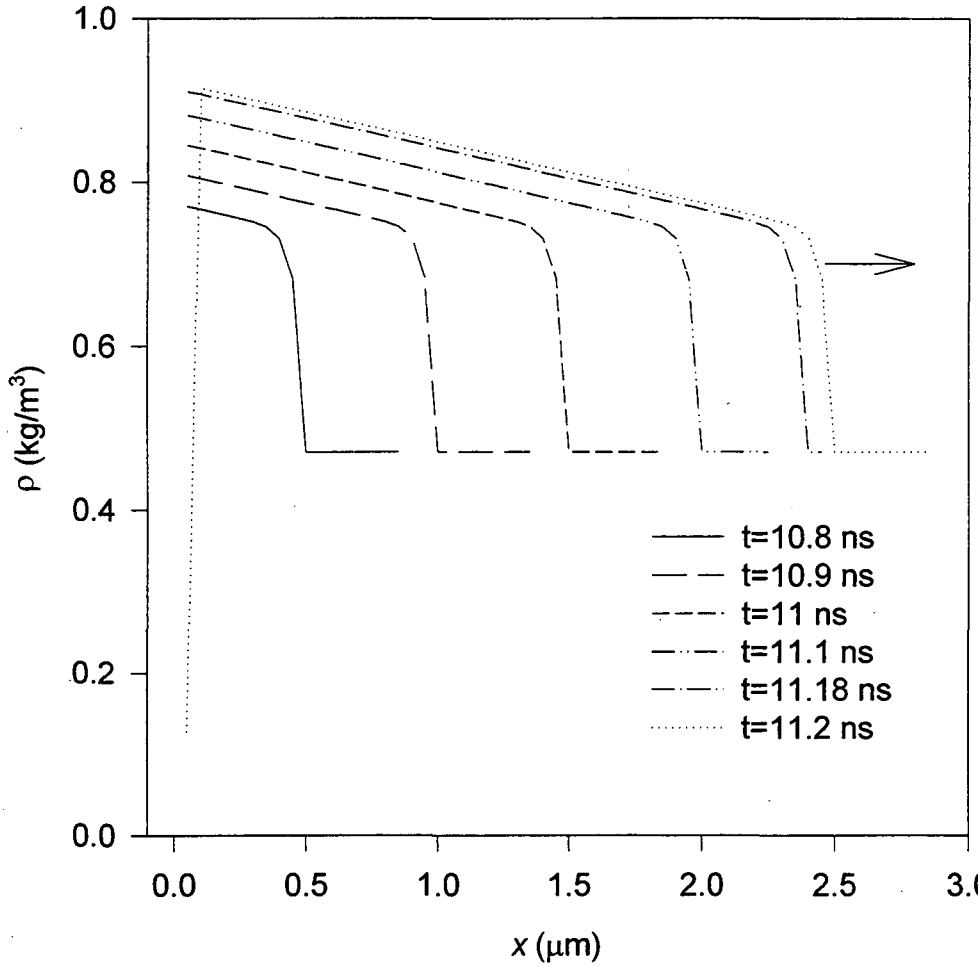

Fig. 3.6(a) Density profiles in the gasdynamic regime near the edge of the Knudsen layer during the early period of evaporation (vaporization started at t=10.72 ns; p_b=0.4 atm, F=7.5 J/cm^2)

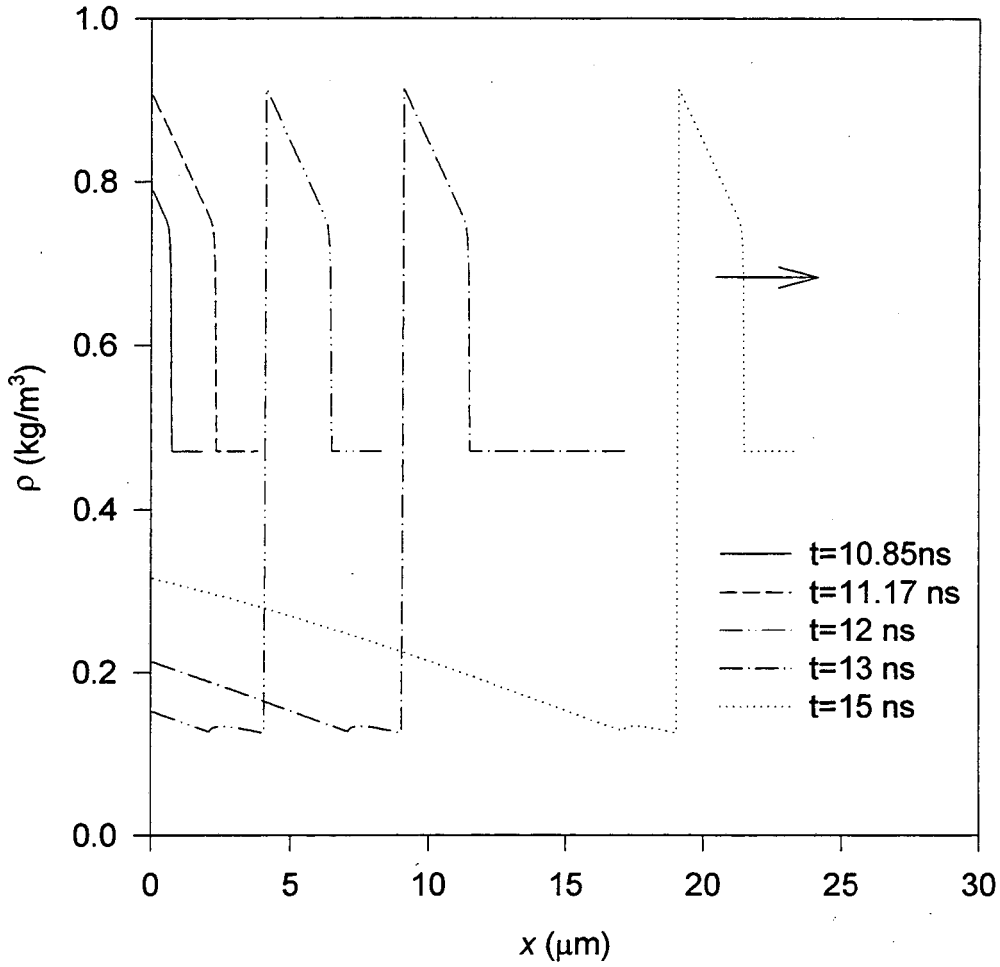

Fig. 3.6(b) Density profiles in the gasdynamic regime near the edge of the Knudsen layer during the early period of evaporation (vaporization started at t=10.72 ns; p_b=0.4 atm, F=7.5 J/cm^2) (continued)

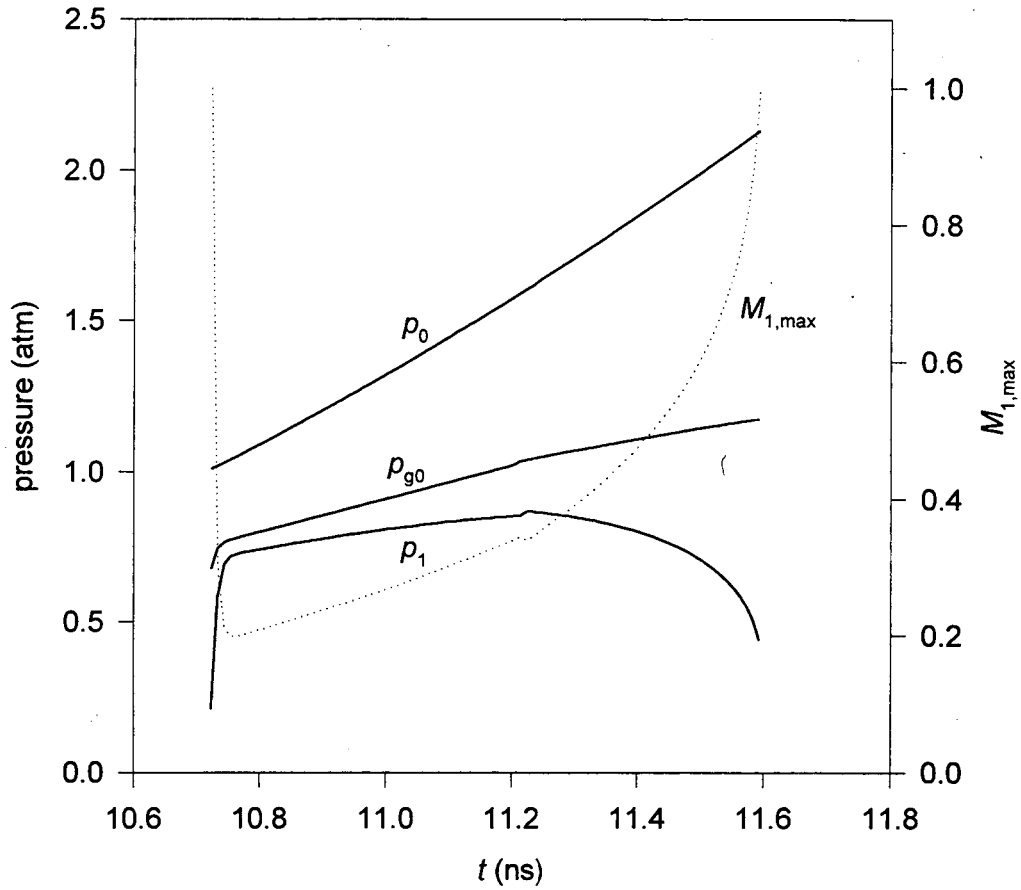

Fig. 3.7 Variation of the maximum Mach number of the vapor and pressure during the early period of evaporation (vaporization started at t=10.72 ns; p_b=0.4 atm, F=7.5 J/cm^2)

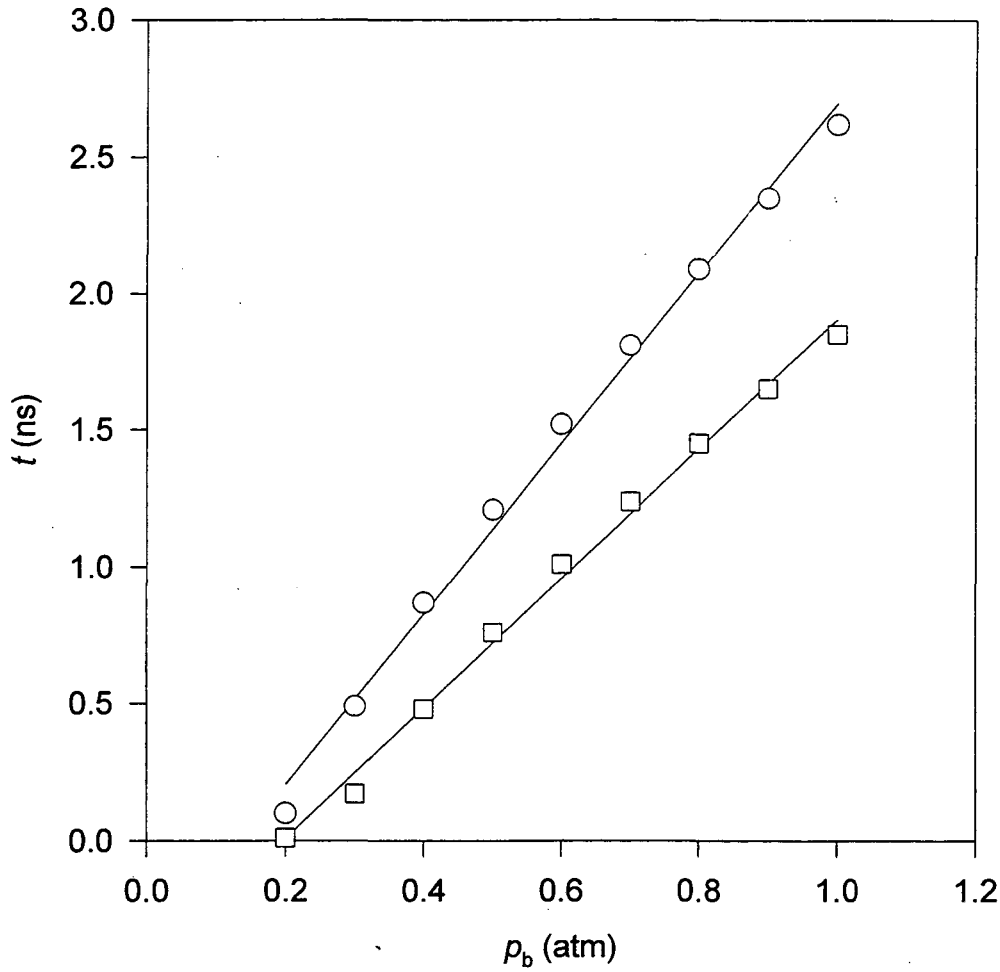

Fig. 3.8 Delay times for $M_{1,max}$ to become unity and for the contact surface to appear in the gasdynamic regime with respect to the ambient pressure (circle: $M_{1,max}$, square: contact surface; F=7.5 J/cm^2)

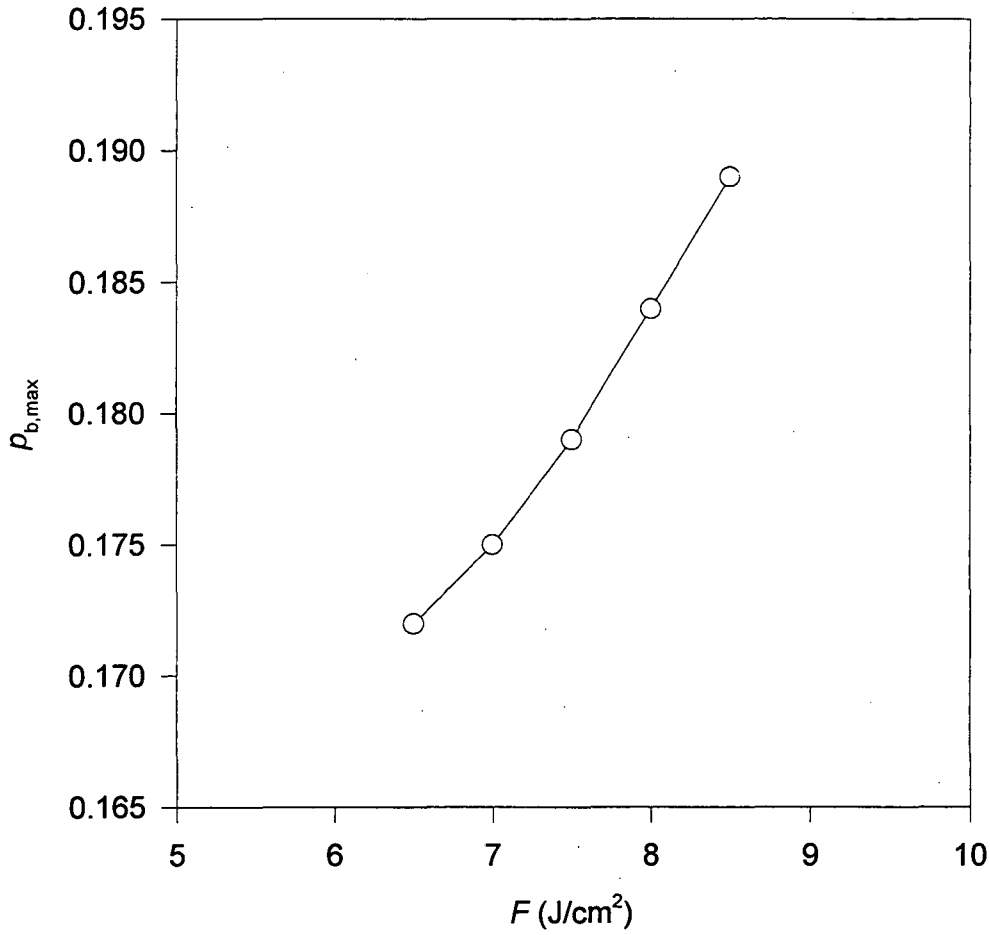

Fig. 3.9 Maximum ambient pressure allowed for $M_{1,max}$ to be equal to unity from the beginning of the evaporation

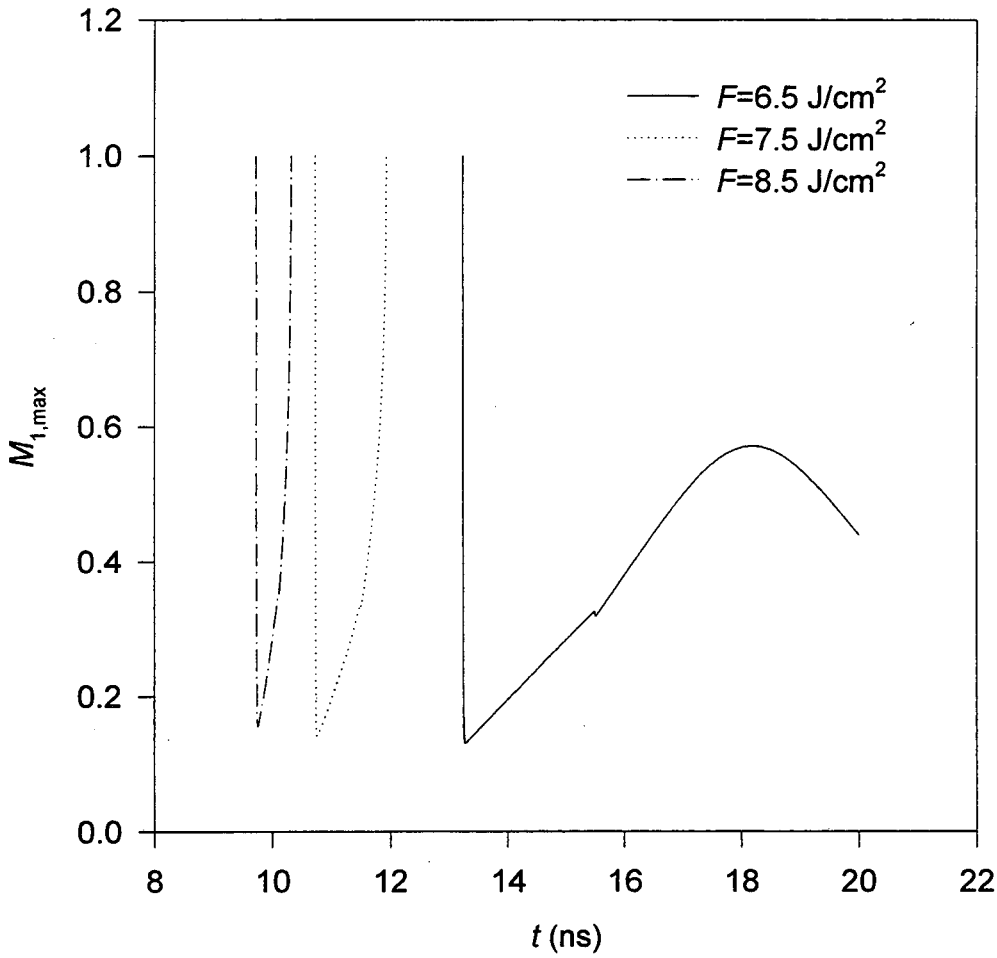

Fig. 3.10 Variation of $M_{1,max}$ with time at different laser fluence. For F=6.5 J/cm^2 $M_{1,max}$ does not become unity during the evaporation.

in laser heating analysis that the vapor velocity at the Knudsen layer is equal to the local sound velocity, which is also known as the Chapman-Jouguet condition. On the contrary to this common assumption, it is found that the Chapman-Jouguet condition can be violated by a small change of the laser fluence; see the difference of $M_{1,max}$ for F=6.5 J/cm^2 and 7.5 J/cm^2 in Fig. 3.10. This indicates that the sonic condition at the edge of the Knudsen layer, which is often employed for simplicity, is not always valid.

These calculation demonstrate that the sonic condition can be applied to the vapor velocity at the Knudsen layer only if the ambient pressure is sufficiently small. In the following, we assume that this condition is satisfied so that M_1 remains equal to unity during evaporation. Since the equations for target heating and the Knudsen layer can be decoupled from those for gasdynamics when M_1 is equal to 1, the equations for target heating and the Knudsen layer are solved separately from the gasdynamic flow in the following calculations. Figs. 3.11(a)-(f) show the temporal variation of the temperature, pressure, and interface velocity at the target surface and the maximum values of these properties with respect to laser fluence. Since the present model considers thermal evaporation only and excludes plasma shielding, the surface temperature should be below the critical temperature of aluminum, about 5720 K [47,48]. (Note that the critical temperature of aluminum used in literatures is not always consistent. Miotello and Kelly [47] used ~5720 K while Bothwick et al [48], Batanov et al.[44], and Wang et al. [49] used 5726 K, ~4700 K, and ~3940 K, respectively). The maximum surface temperatures shown in Fig. 3.11(a) and (b) remains well below the critical temperature for the laser fluences used in this study. However, the surface temperature in Fig. 3.11(a) and (b)

implies strong superheating of the liquid above the boiling temperature, 2793 K. An interesting study was made by Peterlongo et al. [27] by considering the boiling of the target during laser heating. By including the boiling mechanism in their model which eliminated the superheating of the liquid, they obtained a larger material removal rate.

Figs. 3.11(c) and (d) and 3.11(e) and (f) show that the saturation pressure at the surface and the liquid-vapor interface velocity are very strong functions of the laser fluence and change by an order of magnitude over the fluence range from 6.5 to 8.5 J/cm^2. Since the material removal rate from the target is directly related to the velocity of the liquid-vapor interface, these data imply that the material removal rate is also a strong function of the laser fluence. The ablation depth in the target for a single pulse is obtained by integrating the liquid-vapor interface velocity with time and the result is shown in Fig. 3.12. The ablation depth varies from 0.45 to 9.8 nm for the laser fluences from 6.5 to 8.5 J/cm^2 of the current study. Note that the ablation depth calculated by Peterlongo et al. [27] ranges from about 0.05 to 0.65 nm for laser fluences from 3 to 3.7 J/cm^2 while by Ho et al. [16] it varies from about 0.4 to 370 nm for laser fluences from 10 to 25 J/cm^2. The measured ablation depth per single laser pulse reported by Lisfi et al. [50] for frequency tripled Nd-YAG laser (λ=355 nm) heating of Fe_2O_3 was about 33 nm for a laser fluence of about 2.2 J/cm^2 and (FWHM) pulse width of 8 ns and by Jordan et al. [51] for frequency doubled Nd-YAG laser (λ=532 nm) heating of copper was about 5 nm for a laser fluence of about 2.0 J/cm^2 and pulse width of 6 ns. Matthias et al. [52] reported 80 nm per pulse for excimer laser heating of gold film on a fused silica substrate at the laser fluence of 0.47 J/cm^2 for a 14 ns pulse. Because of the rareness and inconsistency of the

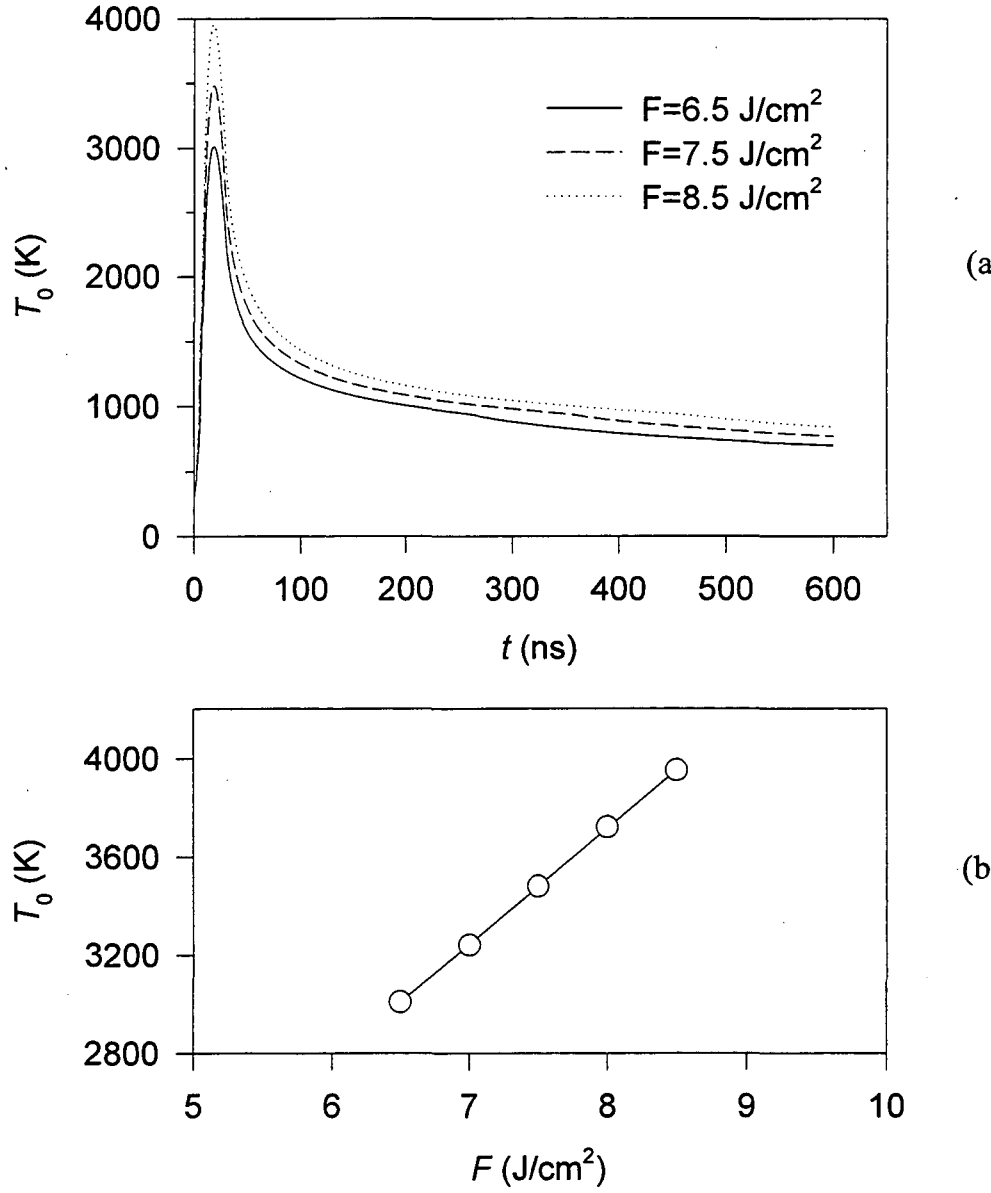

Fig. 3.11 (a) Temporal variation of the target surface temperature and (b) the maximum values for different laser fluences

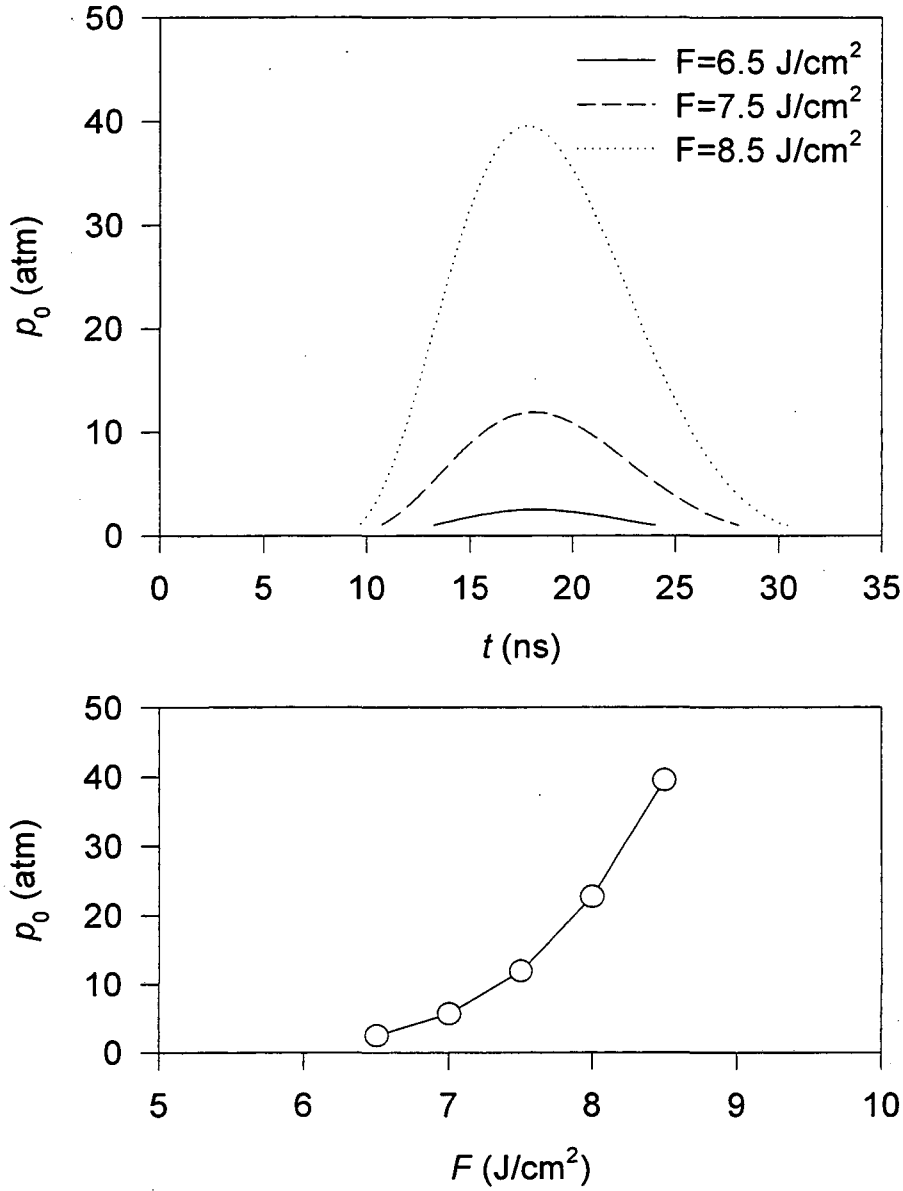

Fig. 3.11 (c) Temporal variation of the saturation pressure at the target surface and (d) the maximum values for different laser fluences

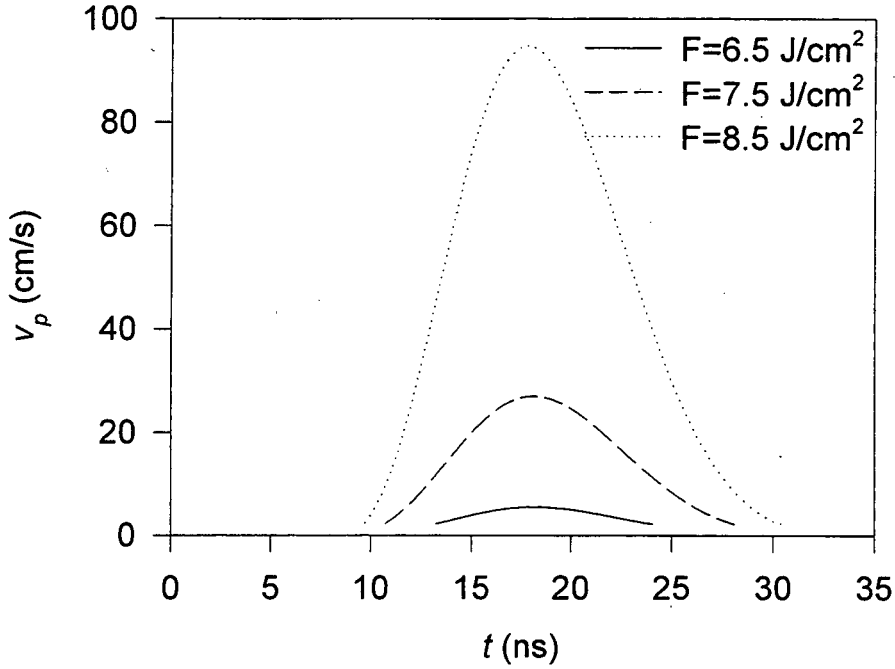

(e)

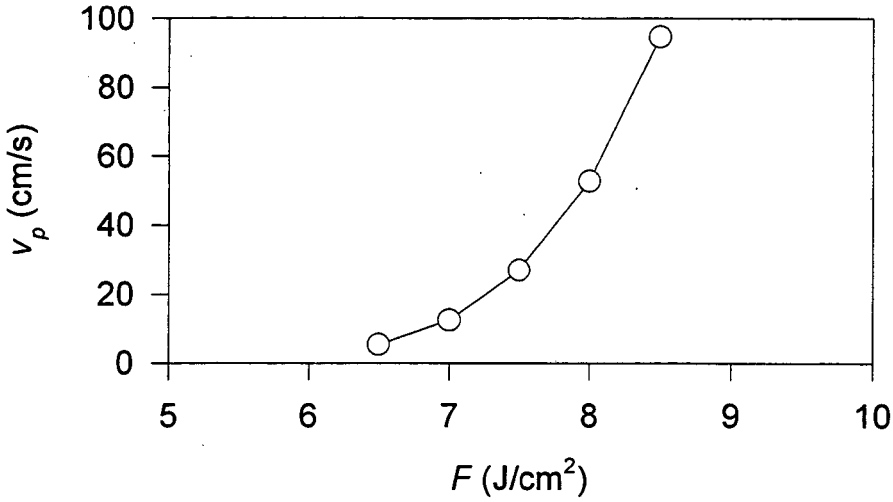

(f)

Fig. 3.11 (e) Temporal variation of the liquid-vapor interface velocity at the target surface and (f) the maximum values for different laser fluences

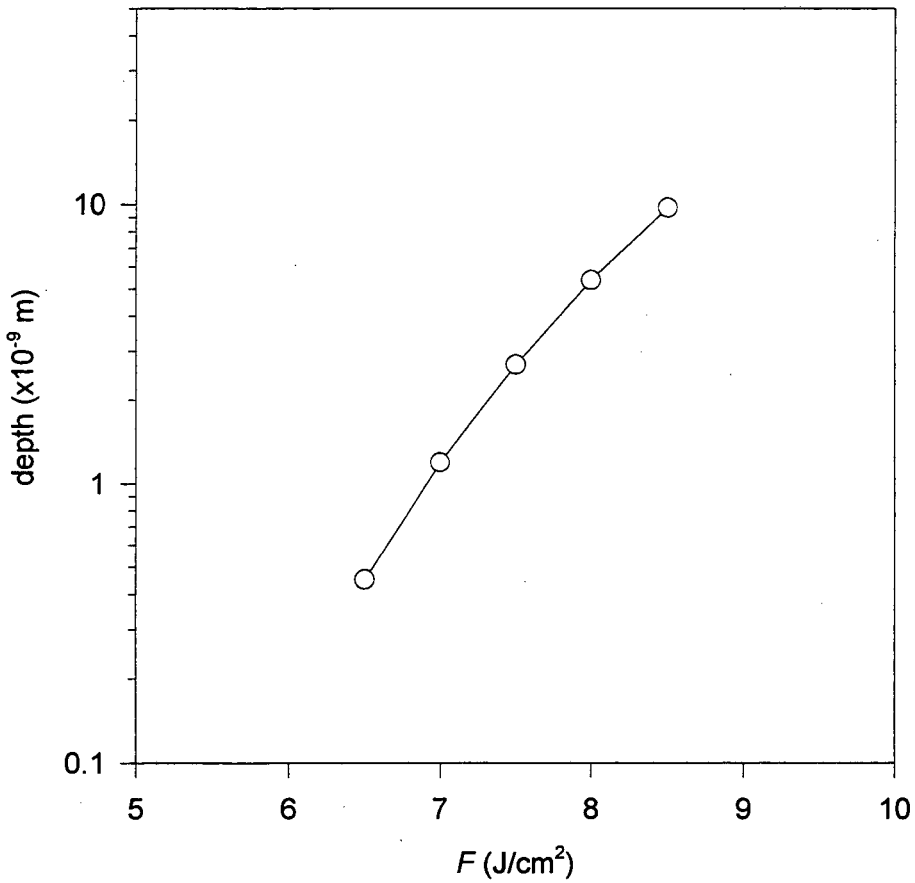

Fig. 3.12 Ablation depth for a single laser pulse with respect to the laser fluence

measured ablation depths, it is difficult to make direct comparison of the computed ablation depth with the measured ones. Nevertheless the computed ablation depth appears to be smaller in general than the measured data. The limits of the thermal model to describe the actual laser evaporation process may be considered as a reason for the difference between the computed and measured ablation depths. Nonthermal mechanisms such as electronic excitation, subsurface explosion, boiling, droplet or particle ejection may be responsible for the increase in the ablation depth.

The temperature profiles in the target after the laser pulse are shown in Fig. 3.13. The thermal penetration into the target after 50 ns is about 10 μm; this is much smaller than the laser spot size (about 1 mm) and is consistent with the one dimensional approximation.

The vapor velocity at the edge of the Knudsen layer is shown in Fig. 3.14(a) and (b). The maximum velocity of the vapor leaving the Knudsen layer appeared to be greater than 1 km/sec. Similar results for this velocity was found by Peterlongo et al. [27].

The behavior of the gasdynamic flow for a given laser fluence of 7 J/cm^2 are presented in Figs. 3.15(a) and (b). The pressure and temperature of the ambient air are 0.01 atm and 300 K, respectively. As noted above, the Mach number of the vapor at the edge of the Knudsen layer for the small selected ambient pressure can be taken to be unity. For the specified conditions, the evaporation of the target initiated at t=11.7 ns and ceased at t=26.4 ns. The maximum target surface temperature occurred at t=18.1 ns. The density profile in the gasdynamic flow is shown in Fig. 3.15(a). The shock wave, the first discontinuity from the far field, and the contact surface, the second discontinuity, are

clearly observed. The region ahead of the shock wave is occupied by the undisturbed air and the region behind the contact surface is by the expanding vapor. The region between the shock wave and the contact surface is the compressed air. (For convenience, these regions and discontinuities are indicated on the curve for t=36.6 ns only.) The region for compressed air becomes larger as the discontinuities move away from the target, which implies different propagation speeds of the two discontinuities. Unsteady adiabatic expansion of the vapor outside the Knudsen layer is an important characteristics of laser induced flow [20, 21, 22]. In case of evaporation into a vacuum, unsteady adiabatic expansion induces the maximum vapor velocity of $4u_1$ at the expansion front. Recall that u_1 is the vapor velocity at the edge of the Knudsen layer. The maximum of u_1 is equal to 1055 m/s for the results shown in Fig. 3.15(a) and (b). For the evaporation into the air with finite pressure (0.01 atm for the present results), the unsteady adiabatic expansion is also observed; see the velocity profile in Fig. 3.15(b). For this case, however, the maximum velocity increase of the vapor is about $1.58u_1$, in contrast to $4u_1$. Instead of developing a greater vapor velocity, the vapor produces a strong compression of the surrounding air between the vapor front and the shock wave which results in a conspicuous density change at the contact surface and at the shock wave; see the density increase of the compressed air in Fig. 3.15(a). The velocity profiles for t=20 ns and t=36.6 ns show that the velocity of the compressed air behind the shock also increased during this period. Therefore, the flow experiences acceleration during the early period through the unsteady adiabatic expansion.

The density profile behind the shock wave shows that the density of the compressed air increases as it approaches the contact surface. The density of the vapor behind the contact surface also first increases and then decreases as moves toward x=0. This discontinuous change of the density at the contact surface and the increase of the air and the vapor density adjacent to the contact surface can not be represented by the analytical solution of an ideal blast wave [53] which is often employed to explain laser induced gasdynamic flows. The density field predicted by the solution of an ideal blast wave decreases monotonically toward x=0. Therefore, there exists an obvious difference between the laser induced flow and the ideal blast wave. However, the ideal blast wave may be still useful as an approximation of the laser induced flow.

The propagation of the shock wave and the contact surface are shown in Fig. 3.16. From the analytical solutions for one dimensional expansion of vapor it is expected that $0.75 < u_{cf} / u_{sh} < 1$ [54], where u_{cf} and u_{sh} is the velocity of the contact surface and the shock wave, respectively. For the result shown in Fig. 3.16, $u_{cf,\mathrm{avg}}/u_{sh,\mathrm{avg}}$ ($u_{,\mathrm{avg}}$ is computed from $x(t)/\Delta t$) decreases from 0.83 to 0.74 with propagation distance, which implies faster deceleration of the contact surface. The maximum average speeds of the shock wave and the contact surface are about 2.0 and 1.6 km/s, respectively.

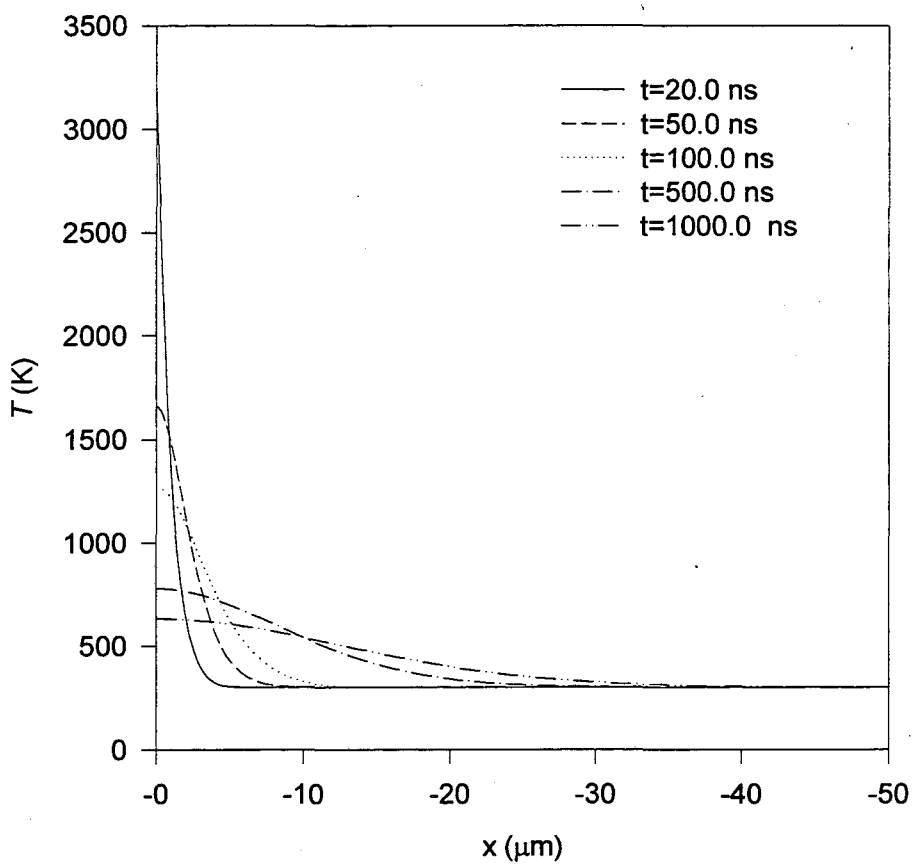

Fig. 3.13 Temperature distribution in the target with time (F=7 J/cm^2)

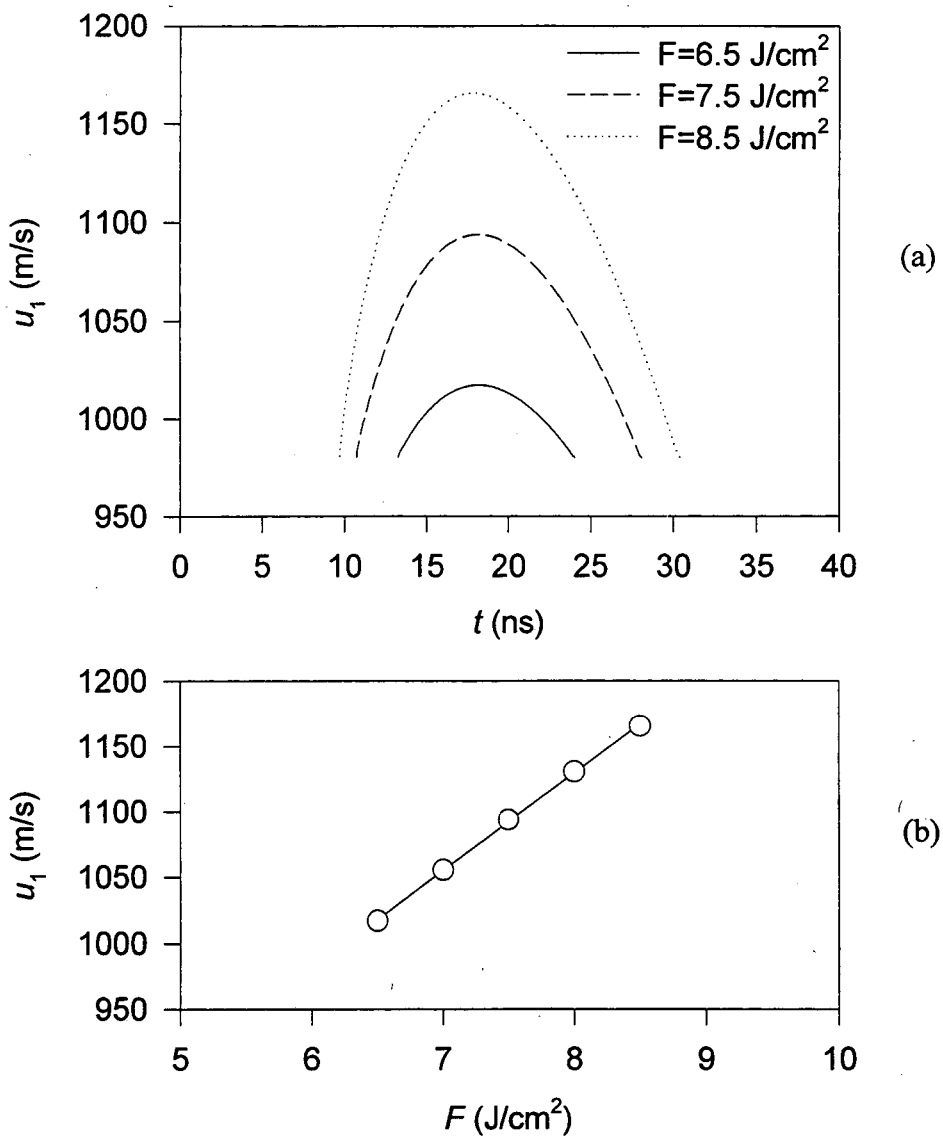

Fig. 3.14 (a) Temporal variation of the vapor velocity at the edge of the Knudsen layer and (b) the maximum values for different laser fluences

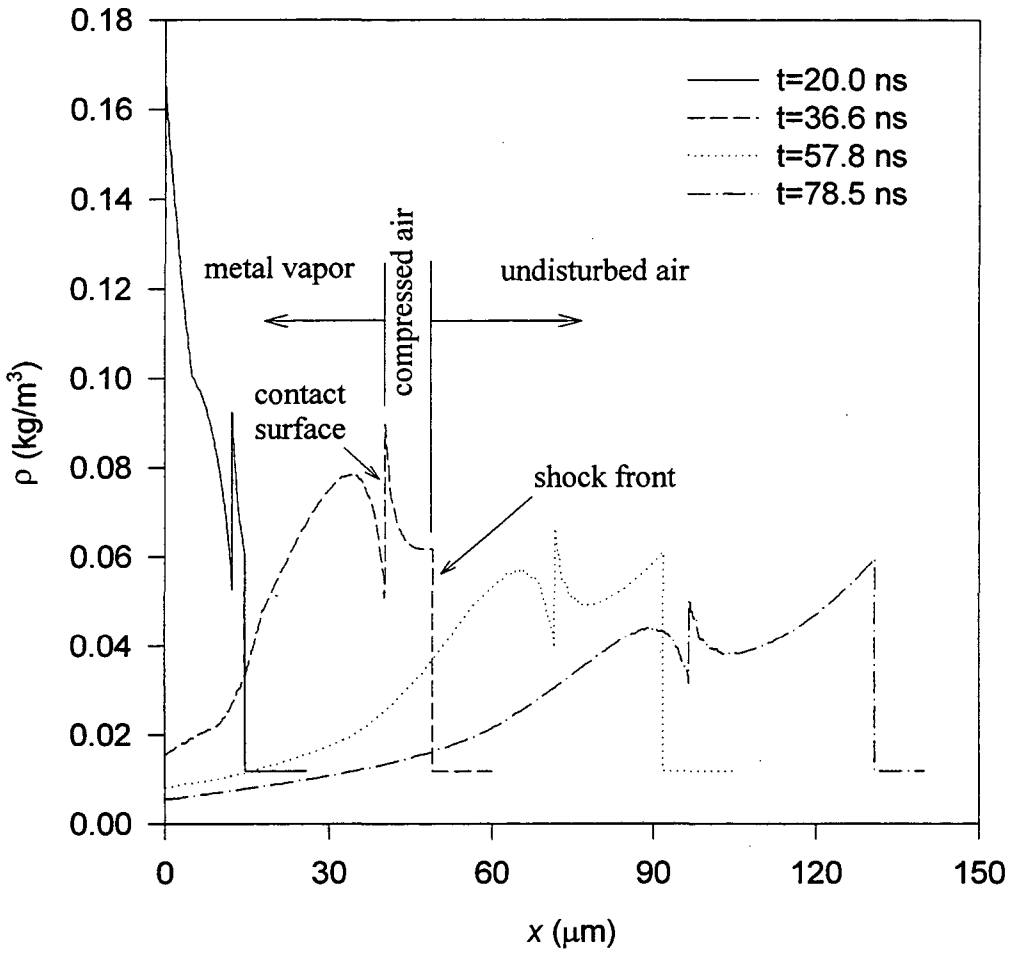

Fig. 3.15(a) Distribution of density in the gasdynamic flow with time (F=7 J/cm^2, p_b=0.01 atm, vaporization started at t=11.68 ns and ceased at t=26.42 ns. Each region and the discontinuities are explained in the context.)

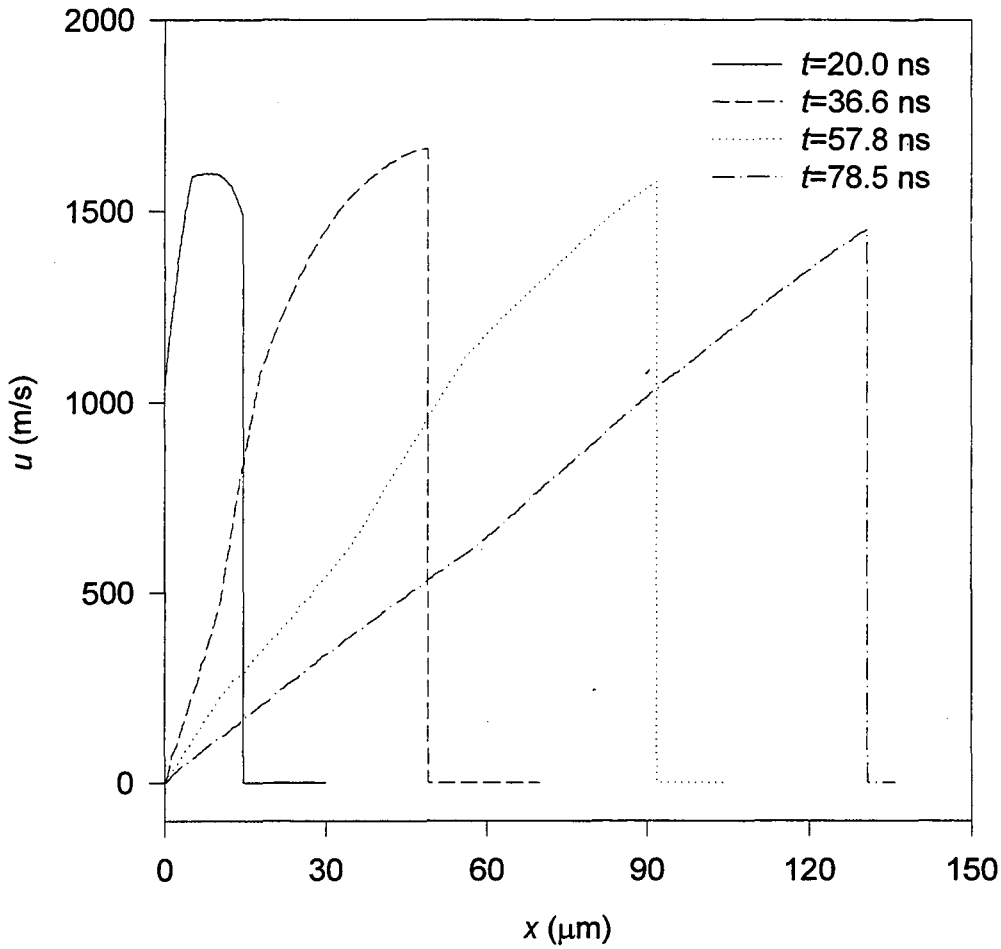

Fig. 3.15(b) Distribution of velocity in the gasdynamic flow with time (F=7 J/cm^2, p_b=0.01 atm, vaporization started at t=11.68 ns and ceased at t=26.42 ns. The maximum vapor velocity at the Knudsen layer is 1055 m/s.)

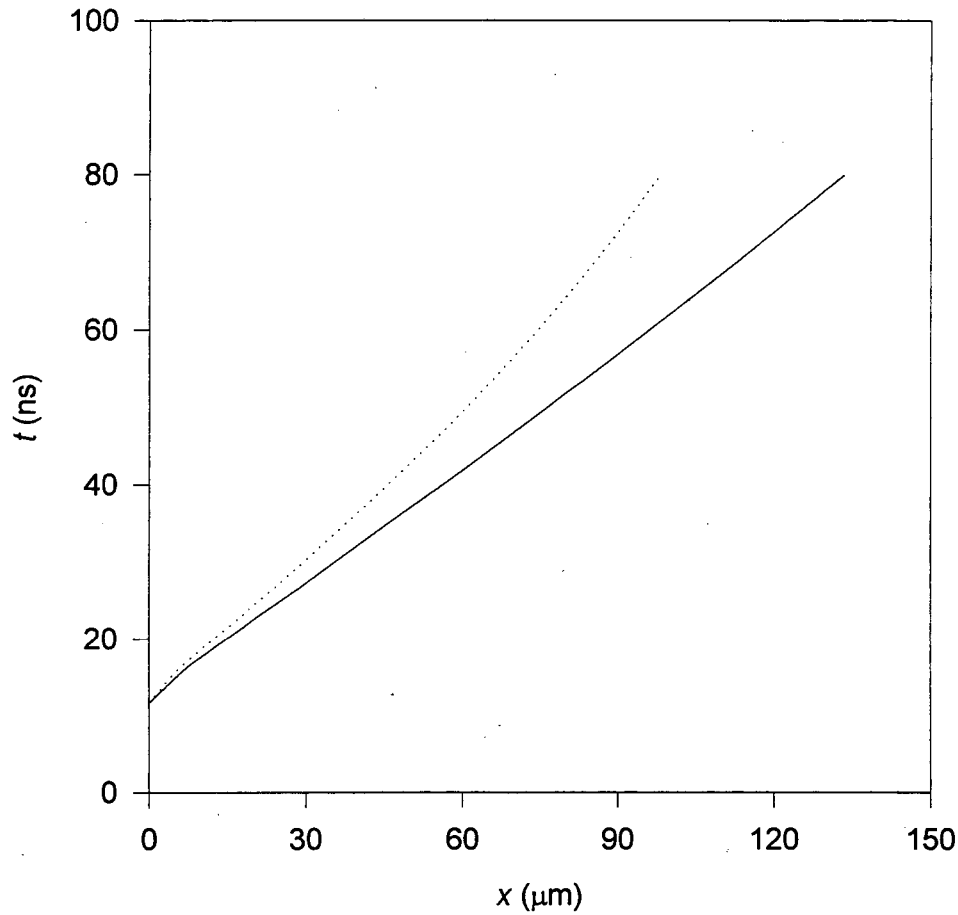

Fig. 3.16 Propagation of the shock wave (solid line) and the contact surface (dotted line) (F=7 J/cm^2, p_b=0.01 atm)

3.5 Conclusion

Unsteady vaporization of a metal target due to nanosecond pulsed laser heating with an ambient gas of finite pressure was studied. A one dimensional thermal evaporation model was employed for target heating with a detailed description of the vapor motion inside the Knudsen layer. Even though the thermal model alone may not be sufficient to describe the complex mechanisms for laser heating of solids, it represents a reasonably good approximation for laser heating with relatively low energy, i.e. below the plasma formation regime. For gasdynamic flow of the vapor, the one dimensional compressible flow equations for an inviscid fluid was solved utilizing the reflection boundary condition. The effects of surface reflectivity on the overall laser energy coupling with the target and the effects of the ambient pressure on the velocity of the vapor leaving the Knudsen layer were investigated in detail. Results for target surface conditions and gasdynamic properties of the vapor for various laser fluences were obtained when the vapor velocity at the Knudsen layer was sonic.

Several important findings can be summarized as follows;

i) The efficiency of laser energy coupling with the target is greatly dependent on the target surface reflectivity.

ii) The threshold laser fluence predicted with the thermal model is larger than the values obtained experimentally. Surface condition change and/or the inability of the thermal model to accurately describe the laser evaporation process is inferred as the possible reason.

iii) The vapor velocity at the edge of the Knudsen layer becomes sonic from the beginning of evaporation only when the ambient pressure is sufficiently small. For large ambient pressures, the vapor velocity varies during the early period of evaporation. The assumption that vapor velocity at the Knudsen layer is equal to the local sound velocity from zero time is found to be valid only for low ambient pressures.

iv) The velocity of the vapor leaving the Knudsen layer is less than the local sound velocity when the laser fluence is too small, i.e. the Chapman-Jouguet condition is not satisfied.

v) The formation of discontinuities, the shock wave and the contact surface, and the separation of flow regions, undisturbed gas, compressed gas, and the expanding vapor, are clearly observed in the density profiles. A difference in the laser induced gasdynamic flow and the ideal blast wave theory is observed.

References

[1] K. Brugger, "Exact solutions for the temperature rise in a laser-heated slab", J. Appl. Phys. Vol. 43, No. 2, 1972, pp. 577-583

[2] B. S. Yilbas, "Analytical solution for the heat conduction mechanism appropriate to the laser heating process", Int. Comm. Heat Mass Transfer, Vol. 20, pp. 545-555, 1993

[3] M. A. Chaudhry and S.M. Zubair, "Conduction of heat in a semi-infinite solid with an exponential-type initial temperature profile : temperature and heat flux solutions due to an instantaneous laser source", Warme und Stoffubertragung 30 (1994) pp. 41-46

[4] B. S. Yilbas and A. Z. Sahin, "Laser heating mechanism including evaporation process", Int. Comm. Heat Mass Transfer, Vol. 21, No. 4, pp. 509-518, 1994

[5] A. A. Rostami, R. Greif, and R. E. Russo, "Modified enthalpy method applied to rapid melting and solidification", Int. J. Heat Mass Transfer, Vol. 35, No. 9, pp. 2161-2172, 1992

[6] S. H. Jeong, R. Greif, and R. E. Russo, "Laser heating of a cavity versus a plane surface for metal targets utilizing photothermal deflection measurements", J. Appl. Phys. 80 (4), 1996, pp. 1996-2002

[7] C. L. Chan and J. Mazumder, "One-dimension steady-state model for damage by vaporization and liquid expulsion due to laser-material interaction", J. Appl. Phys. 62 (11) 1987, pp. 4579-4586

[8] R. Kelly, A. Miotello, B. Braren, A. Gupta, and K. Casey, "Primary and secondary mechanisms in laser-pulse sputtering", Nuclear Instruments and Methods in Physics Research B 65, 1992, pp. 187-199

[9] Yu. V. Afanasev and O. N. Krokhin, "Vaporization of matter exposed to laser emission", Soviet Physics JETP, Vol. 25, No. 4, 1967, pp. 639-645

[10] S. I. Anisimov and A. Kh. Rakhmatulina, "The dynamics of the expansion of a vapor when evaporated into a vacuum", Sov. Phys. JETP, Vol. 37, No. 3, 1973, pp. 441-444

[11] C. J. Knight, "Theoretical modeling of rapid surface vaporization with back pressure", AIAA Journal Vol. 17, No. 5, May 1979, pp. 519-523

[12] H. M. Urbassek and J. Michl, "A gas-flow model for the sputtering of condensed gases", Nuclear instruments and methods in physics research B22, 1987, pp. 480-490

[13] R. Kelly, "Thermal sputtering as a gas-dynamic process", Nuclear Instruments and Methods in Physics Research B46, 1990, pp. 441-447

[14] V. I. Igoshin and V. I. Kurochkin, "Laser evaporation of metals in a gaseous atmosphere", Sov. J. Quantum Electron. 14 (8), 1984, pp. 1049-1052

[15] M. Aden, E. Beyer, and G. Herziger, "Laser-induced vaporisation of metal as a Riemann problem", J. Phys. D, 23, 1990, pp. 655-661

[16] J. R. Ho, C. P. Grigoropoulos, and J. A. C. Humphrey, "Computational study of heat transfer and gas dynamics in the pulsed laser evaporation of metals", J. Appl. Phys. 78 (7) 1995, pp. 4696-4709

[17] J. R. Ho, C. P. Grigoropoulos, and J. A. C. Humphrey, "Gas dynamics and radiation heat transfer in the vapor plume produced by pulsed laser irradiation of aluminum", J. Appl. Phys. 79 (9) 1996, pp. 7205-7215

[18] R. Kelly and R. W. Dreyfus, "Reconsidering the mechanisms of laser sputtering with Knudsen-layer formulation taken into account", Nuclear Instruments and Methods in Physics Research B32, 1988, pp. 341-348

[19] R. Kelly and B. Braren, "On the direct observation of the gas-dynamics of laser-pulse sputtering of polymers", Appl. Phys. B 53, 1991, pp. 160-169

[20] B. Braren, K. G. Casey, and R. Kelly, "On the gas dynamics of laser-pulse sputtering of polymethylmethacrylate", Nuclear instruments and methods in physics research B 58, 1991, pp. 463-472

[21] R. Kelly, "Gas dynamics of the pulsed emission of a perfect gas with applications to laser sputtering and to nozzle expansion", Physical Review A, Vol. 46, No. 2, 1992, pp. 860-874

[22] A. Miotello, A. Peterlongo, and R. Kelly, "Laser-pulse sputtering of aluminum: gas-dynamic effects with recondensation and reflection conditions at the Knudsen layer", Nuclear instruments and methods in physics research B 101, 1995, pp. 148-155

[23] A. Fernandez, X. L. Mao, W. T. Chan, M. A. Shannon, and R. E. Russo, "Correlation of spectral emission intensity in the inductively coupled plasma and the laser-induced plasma during laser ablation of solid samples", Anal. Chem, Vol. 67, No. 14, 1995, pp. 2444-2450

[24] X. L. Mao, W. T. Chan, M. Caetano, M. A. Shannon, and R. E. Russo, "Preferential vaporization and plasma shielding during nanosecond laser ablation", Applied Surface Science, 96-98, 1996, pp. 126-130

[25] Xianglei Mao and Richard E. Russo, "Observation of plasma shielding by measuring transmitted and reflected laser pulse temporal profiles", Appl. Phys. A 64, 1997, pp. 1-6

[26] S. I. Andreev, I. V. Verzhikovskii, and Yu. I. Dymshits, "Plasma formation in a solid target by a single-shot laser", Soviet Physics-Technical Physics, Vol. 15, No. 7, 1971, pp. 1109-1112

[27] A. Peterlongo, A, Miotello, and R. Kelly, "Laser-pulse sputtering of aluminum: Vaporization, boiling, superheating, and gas-dynamic effects", Physical review E, Vol. 50, No. 6, 1994, pp. 4716-4727

[28] V. I. Mazhukin and A. A. Samokhin, "Kinetics of a phase transition during laser evaporation of a metal", Sov. J. Quantum Electron. 14 (12), 1984, pp. 1608-1611

[29] L. Balazs, R. Gijbels, and A. Vertes, "Expansion of Laser-Generated Plumes Near the Plasma Ignition Threshold", Anal. Chem., 63, 1991, pp. 314-320

[30] J.P. Hirth and G.M. Pound, *Condensation and Evaporation; Nucleation and Growth Kinetics*, Pergamon, 1963

[31] S. I. Anisimov, "Vaporization of metal absorbing laser radiation", Soviet Physics JEPT, Vol. 27, No. 1, 1968, pp. 182-183

[32] T. Ytrehus, "Theory and experiments on gas kinetics in evaporation", in *Rarefied gas dynamics,* edited by J.L. Potter, AIAA, 1977, pp. 1197-1212

[33] R. J. LeVeque, *Numerical Methods for Conservation Laws*, 2nd Ed., Birkhauser Verlag, Basel, 1992

[34] P. Colella, "Glimm's method for gas dynamics", SIAM J. Sci. Stat. Comput., Vol. 3, No. 1, March 1982, pp. 76-110

[35] G.A. Sod, "A survey of several finite difference methods for systems of nonlinear hyperbolic conservation laws", Journal of Computational physics, 27, 1978, pp. 1-31

[36] A.J. Chorin, "Random choice solution of hyperbolic systems", Journal of Computational Physics, 22, 1976, pp. 517-533

[37] G.A. Sod, *Numerical Methods in Fluid Dynamics*, Cambridge, 1985

[38] C. J. Smithells, *Smithells Metals Reference Book*, 7th ed., Butterworth-Heinemann, 1992

[39] Y.S. Touloukian et al., Thermal Conductivity; Metallic Elements and Alloys, Vol. 1, and Thermal Diffusivity, Vol. 10, *Thermophysical Properties of Matter*, IFI/Plenum, 1970

[40] J. R. Ho, *Numerical Modeling of the Pulsed Laser Evaporation of Metals*, Ph. D Thesis, University of California, Berkeley, 1994

[41] T. Iida and R. I. L. Guthrie, *The Physical Properties of Liquid Metals*, Oxford, 1988

[42] E. Heidecker, J. H. Schafer, J. Uhlenbusch, and W. Viol, "Time-resolved study of a laser-induced plasma by means of a beam-deflection technique", J. Appl. Phys., 64 (5), 1988, pp. 2291-2297

[43] M. von Allmen, *Laser-Beam Interactions with Materials*, Springer, 1987

[44] V. A. Batanov, F. V. Bunkin, A. M. Prokhorov, and V. B. Fedorov, "Evaporation of metallic targets caused by intense optical radiation", Soviet Physics JETP, Vol. 36, No. 2, 1973, pp. 311-322

[45] R. M. Gilgenbach and P. L. G. Ventzek, "Dynamics of excimer laser ablated aluminum neutral atom plume measured by dye laser resonance absorption photography" Appl. Phys. Lett., 58 (15), 1991, pp. 1597-1599

[46] R. W. Dreyfus, R. Kelly, and R. E. Walkup, "Laser-induced fluorescence studies of excimer laser ablation of Al_2O_3", Appl. Phys. Lett., 49(21), 1986, pp. 1478-1480

[47] A. Miotello and R. Kelly, "Critical assessment of thermal models for laser sputtering at high fluences", Appl. Phys. Lett., 67 (24), 1995, pp. 3535-3537

[48] I. Borthwick, C. T. J. Scott, K. W. D. Ledingham, and R. Singhal, "Velocity distributions of aluminum atoms ablated from aluminum metal", in *Laser ablation; mechanisms and applications II*, edited by J. C. Miller and D. B. Geohegan, AIP Press, 1993, pp. 414-420

[49] H. Wang, A. P. Salzberg, and B. R. Weiner, "Laser ablation of aluminum at 193, 248, and 351 nm", Appl. Phys. Lett., 59 (8), 1991, pp. 935-937

[50] A. Lisfi, M. Guyot, R. Krishnan, and V. Cagan, "Measurement and calculation of the Fe_2O_3 ablation depth", Applied surface Science, 96-98, 1996 pp. 66-70

[51] R. Jordan, D. Cole, J. G. Lunney, K. Mackay, and D. Givord, "Pulsed laser ablation of copper", Applied surface Science, 86, 1995, pp. 24-28

[52] E. Matthias, J. Siegel, S. Petzoldt, M. Reichling, H. Skurk, O. Kading, and E. Neske, "In-situ investigation of laser ablation of thin films", Thin solid films 254, 1995, pp. 139-146

[53] L. I. Sedov, *Similarity and dimensional methods in mechanics*, 10th ed., 1993, CRC press

[54] R. Kelly, A. Miotello, B. Braren, and C. E. Otis, "On the debris phenomenon with laser-sputtered polymers", Appl. Phys. Lett., 60 (24), 1992, pp. 2980-2982

Chapter 4

Measurement of the propagation of the laser induced shock wave and material plume utilizing the probe beam deflection technique

4.1 Introduction

In this chapter, the dynamics of the laser generated plume due to pulsed laser heating of solid targets is investigated experimentally. The extremely rapid heating and evaporation of a solid target due to nanosecond pulsed laser heating results in the vapor pressure at the target surface being orders of magnitude higher than atmospheric pressure as discussed in chapter 3. The subsequent explosive expansion of the vapor into the ambient gas produces a strong compression of the ambient gas and a shock wave propagates ahead of the compressed gas. The compressed ambient gas is followed by the vapor from the target and the boundary between these two region is called the contact surface. The vapor flow near the target surface is considered one dimensional and transforms into a hemispherical shape as the plume expands. Fig. 4.1 schematically depicts this process. Fig. 4.1 is a significantly simplified representation of the complex laser ablation process. (Actually Fig. 4.1 represents the thermal evaporation only.) Other mechanisms such as the strong recoil pressure exerted on the liquid by the expanding

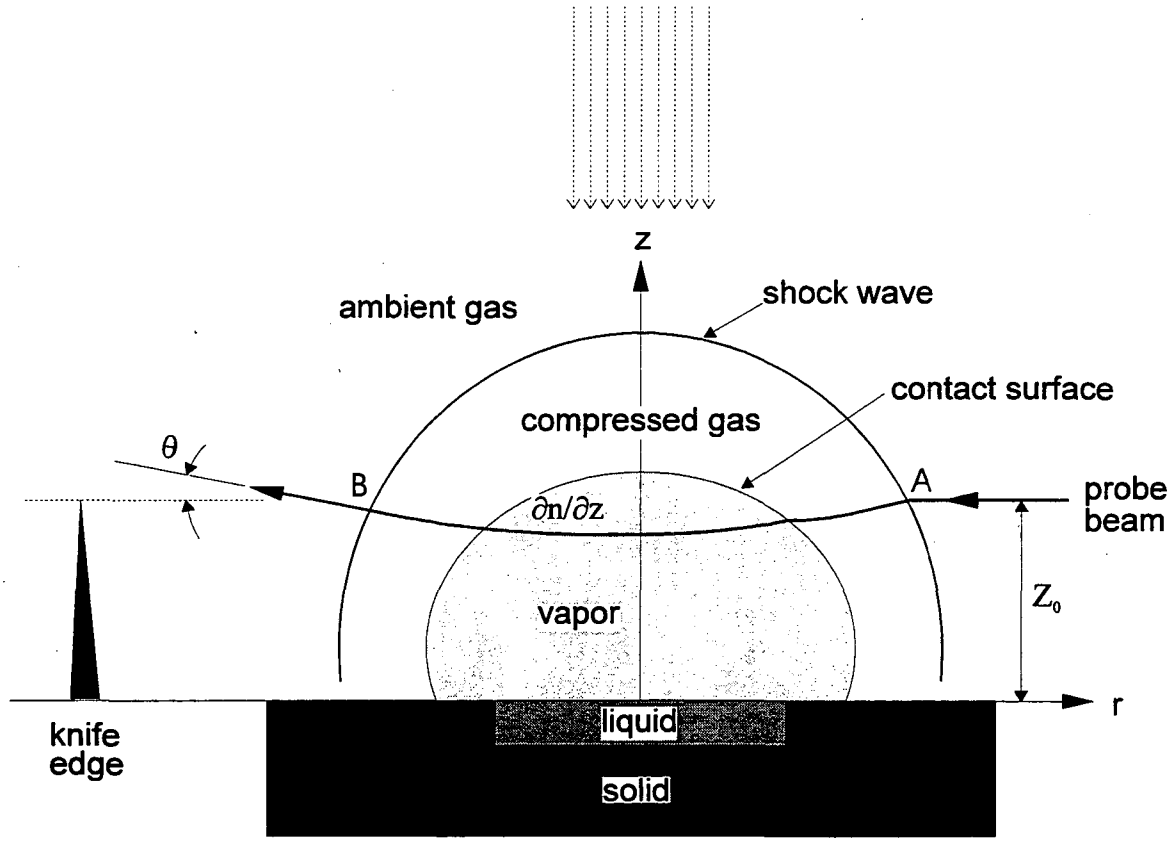

Fig. 4.1 Schematic diagram of the laser induced gasdynamic flow and the deflection of the probe beam

vapor, boiling, or subsurface explosion of the material may result in the flow of droplets or particles into the plume [1]. When the vapor density is high enough, the heating of the vapor by the incident laser light may results in ionization of the vapor with associated plasma shielding [2-4].

In many laser-material interactions the laser induced plume is the most convenient source of in-situ information on the laser evaporation process. Material liberation from the target, vapor interaction with the surrounding gas, target temperature during laser heating, conversion efficiency of laser energy, and plasma formation may be examined experimentally with properly designed diagnostic systems. Also since the pulsed laser deposition (PLD) technique directly utilizes the laser generated material vapor to produce a thin film on a nearby substrate, understanding the characteristic features of the laser induced plume is important for achieving high quality thin films.

Experimental methods which are most often employed for laser induced plume studies include laser induced fluorescence (LIF) spectroscopy [5,6], resonance ionization mass spectroscopy (RIMS) [7], fast imaging with intensified-charge coupled devices (ICCD) [8-10], fast photography [11-15], and probe beam deflection measurements [16-22]. The spectroscopy methods, LIF or RIMS, measure (in principle) the velocity distribution of individual atoms in the plume and the acquired data may be used to predict the target surface temperature [6,7]. These methods, however, are not covered in the present study. Fast imaging, fast photography, and probe beam deflection techniques measure the propagation of ablated material, shock wave, and laser generated plasmas. With the fast imaging or photography, the instantaneous spatial distribution of vapor,

particles [8,11,13,14,23,24], shock wave [12-15], and plasma [15] in the plume can be obtained. When the delay time is varied, information for the propagation of the plume with time may also be obtained. However, to obtain an image or photograph of the plume with good time and spatial resolution, at least two high power lasers are required; one for target heating and another for illumination of the plume [13,15]. If tuning of the illumination laser wavelength is required, another laser, usually a dye laser, is also necessary. Therefore an imaging or photographic system tends to be complex and costly. The probe beam deflection technique, on the other hand, measures the propagation of gasdynamic phenomena that produce the variation of the refractive index in the flow field, e.g. the laser induced shock wave or the vapor from the target. Since a small power continuous wave (CW) laser is used as the probe beam (usually a He-Ne laser with a power of a few mili-Watts), the experimental system is simple. Furthermore the fast response of the probe beam to any variation of the refractive index enables the measurement of rapidly varying temporal signals (with this technique), which is especially useful for time-of-propagation measurements. Thus the probe beam deflection technique is widely employed for the diagnostics of laser induced gasdynamic flows [16-21,25-29].

The theory of deflection of a single ray of light traveling through a continuously changing refractive index field is presented in the Appendix. Experimentally, a CW laser beam with a finite diameter is used as the probe beam. When there is no gasdynamic flow, the probe beam passes parallel to the target surface with a certain distance from the surface (see Fig. 4.1). When the laser induced gasdynamic flow including the shock

wave, contact surface, and the vapor propagate across the probe beam, the resulting variation of the refractive index makes the probe laser beam change its direction. At the shock wave front, refraction of the probe beam occurs while a continuous change of direction occurs in the compressed gas and the vapor regimes. Thus the resultant deflection of the probe beam as it leaves the gasdynamic flow region, θ in Fig. 4.1, is an integrated deflection of the probe beam over the whole path, $\overline{AB}$. Note that θ can be either positive or negative. The resultant deflection of the probe beam can be measured with a knife edge and a photodiode or with a position sensitive detector. In Fig. 4.1, the knife edge and photodiode method is depicted. When there is no deflection, the knife edge blocks one half of the probe beam from the target side and the remainder of the probe beam illuminates the photodiode, which is placed behind the knife edge (not shown in Fig. 4.1). As the plume propagates, the deflection angle θ varies resulting in a variation of the fraction of the probe beam blocked by the knife edge (and thus the fraction illuminating on the photodiode). This variation of the photodiode output during the propagation of the laser induced plume is recorded as the probe beam deflection signal.

The probe beam deflection technique can be utilized to diagnose laser heating of solids with and without evaporation of the target. Without evaporation of the target, the deflection of the probe beam is due to the thermal gradient in the ambient gas as presented in Chapter 2 and is called photothermal deflection [30-32]. The time scale of the photothermal deflection measurement is mostly on the order of milliseconds. When laser evaporation of solids is involved, the time scale decreases to the order of microseconds. The probe beam deflection technique has been used for various studies of

the laser evaporation processes, e.g. measurements of the damage threshold of solids [16,33-35], velocity of the vapor [16,29], shock wave velocity [17,18,20,21,25,26,28], and surface plasmas [19,36]. Lately measurements of shock wave propagation using the probe beam deflection technique have been increased. Since the laser induced shock wave carries information for the energy at the source, the time-of-propagation data of the laser induced shock wave can be used to estimate the laser energy associated with the gasdynamic flow. In order to predict the conversion efficiency of the laser energy into the laser induced gasdynamic flow, a theoretical model is necessary for comparison with the measured data. Blast wave theory which is described in section 4.3 is widely used [9,11,15,17,20,21,25,37,38]. There is considerable variation of the energy conversion efficiency predicted by various researchers using blast wave theory. For example, a 20% conversion efficiency was reported by Diaci and Mozina [25] for aluminum and steel heating with a Nd-YAG laser (λ=1064 nm) while 80% was given by Caliies et al. [15] for copper sample with an excimer laser(λ=248 nm), 37-42% by Jamieson and Wetsel [18] for silicon with a N_2-pumped dye laser , about 25% by Zyung et al. [9] for PMMA with a Nd-YAG laser (λ=532 nm), and 12% by Lee et al. [37] for Al_2O_3 film on silicon substrate with CO_2 laser (λ=10.6 μm). All these conversion efficiencies were based on the laser pulse energy incident on the target. There are also many cases in which the shock wave propagation data are fitted using a blast wave correlation, without explicitly calculating the conversion efficiency [11,20,38]. In order to make better use of the theory and the measured shock wave propagation data during laser evaporation, further studies of laser induced gasdynamic flow, especially in comparison with blast wave theory, are desirable.

In the present work, the propagation of the plume generated during excimer laser heating of an aluminum targets is studied. The probe beam deflection technique is utilized to measure the transit time of the gasdynamic flow. The deflection of the probe beam due to a traveling shock wave is identified. The effects of ambient pressure and laser spot size on the propagation of the shock wave are investigated. From the comparison of the measured shock wave propagation data with ideal blast wave theory, conditions for which ideal blast wave theory is applicable to a laser induced blast wave are found. The incident laser energy coupled to the laser induced blast wave is estimated using the theoretical solution and used to examine the difference between a laser induced blast wave and the ideal blast wave. The propagation of material vapor is observed from the deflection at later time of the probe beam.

4.2 Experimental System

The experimental system is shown schematically in Fig. 4.2. A KrF excimer laser with wavelength 248 nm (Lambda Physik) was used as the heating source. A typical excimer laser pulse has an intensity profile of about 21 ns full-width at half maximum (FWHM) with a decay tail extending to about 45 ns (see Fig. 4.3). In order to obtain a uniform spatial energy distribution on the target, the central portion of the excimer laser beam is selected with a circular aperture with diameter of 4.3 mm. A beam splitter (BS1) is placed in the optical path to extract a small fraction of the heating laser beam for triggering the oscilloscope. The laser pulse energy delivered to the target is measured

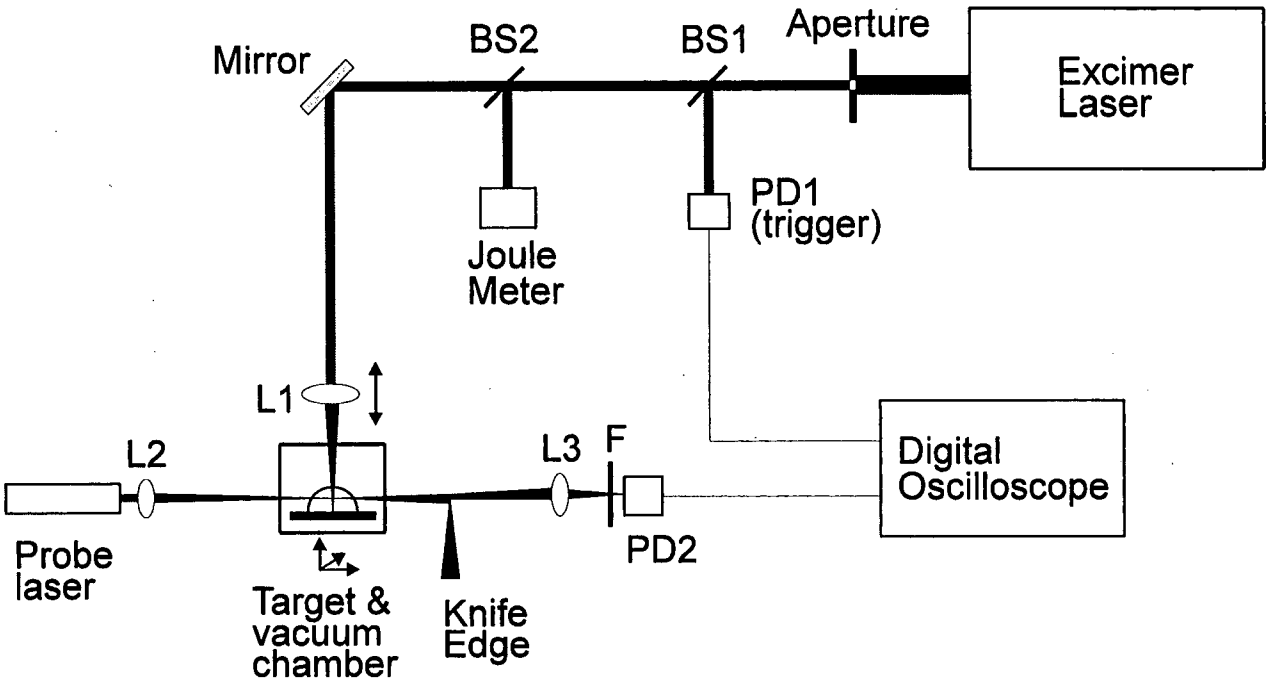

Fig. 4.2 Schematic diagram of the experimental system

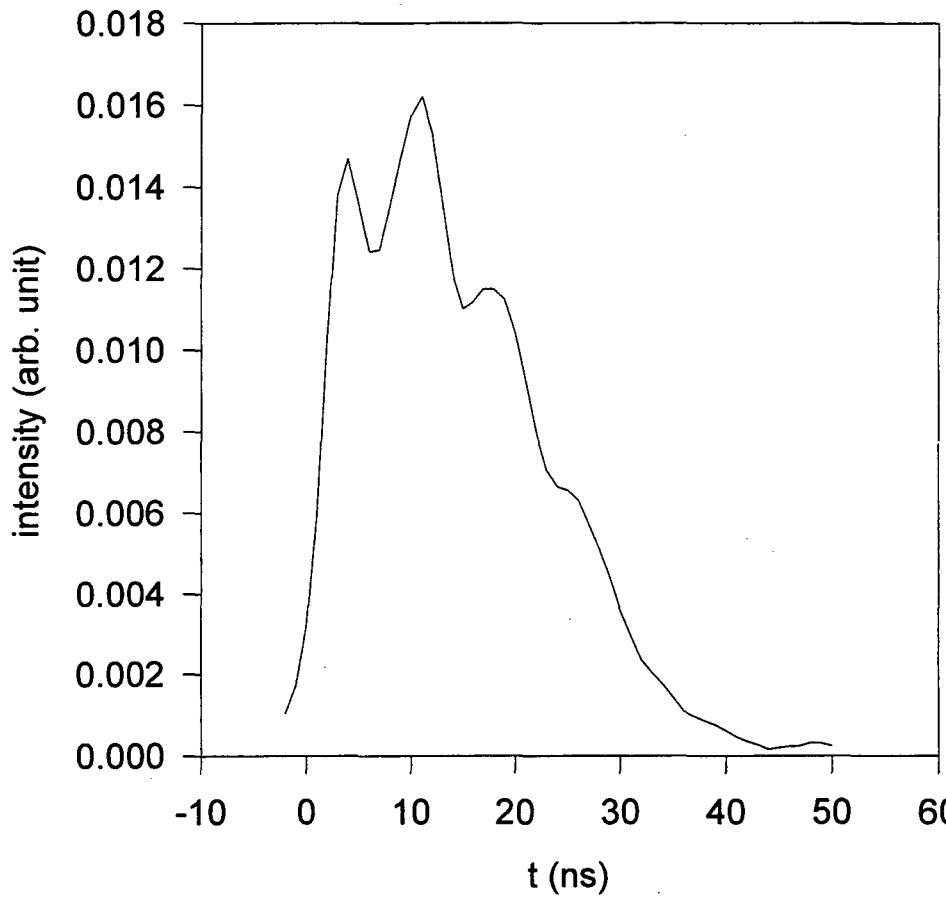

Fig. 4.3 A typical temporal profile of the excimer laser pulse

with a joulemeter (Molectron, Model J50) by collecting a known portion of the excimer laser beam with a second beam splitter (BS2). The excimer laser beam is focused on the target with a lens (L1) to achieve a high power density. The diameter of the laser spot on the target surface is adjusted by varying the distance between the focusing lens and the target surface. A He-Ne laser with wavelength of 543.5 nm (Electro-Optics) is used as the probe beam. The probe laser beam is focused into a small beam diameter using a lens (L2) with a focal length of 350 mm. The probe beam is aligned parallel to the target surface. To minimize lateral deflection of the probe beam during laser heating of the target, i.e. the deflection in a plane parallel to the target surface, the axis of the probe beam is aligned to pass over the center of the laser spot. The deflection of the probe laser beam is measured with a knife edge and photodiode (PD2, ThorLab, Model DET-I) combination. In order to eliminate the effect of stray light, a filter (F) is used in front of the photodiode. The photodiode signal is measured with a digital oscilloscope (Tectronics, DSA 602). The sample is mounted on a three directional translation stage in order to adjust the offset of the probe beam. The data for low ambient pressures were obtained by placing the sample in a vacuum chamber.

Aluminum targets with 1 mm thickness and purity 99.99 % (Aldrich) were used as the sample. The surface of each sample was polished with #600 SiC sand paper and cleaned of particles using an ultrasonic cleaner. The surface of some samples was mirror polished in order to achieve a better observation of the surface morphology with scanning electron microscope (SEM). The data shown in this study are for single pulse laser

heating unless otherwise specified. For the single pulse measurements, the target was translated to a new location for the heating laser beam after each measurement.

4.3 Blast wave theory

When a finite amount of energy is instantaneously released in a gas at a point, a spherical shock wave forms and propagates through the surrounding gas. The gas inside the shock wave is strongly compressed and remains in a relatively thin layer just behind the shock front. As the shock wave expands, more and more surrounding gas is contained in the shock front. Since the original amount of energy released in the explosion is constant, the expansion velocity decreases. This type of unsteady shock wave is called a blast wave [39]. Because the explosive evaporation of solids by a focused high power pulsed laser has many similarities to an ideal blast wave, there have been increasing attempts to analyze laser evaporation in terms of blast wave theory [9,11,15,17,20,21,25,37,38]. To apply blast wave theory to the laser evaporation of solids, two crucial assumptions have to be made. First the mass of the evaporated material must be negligibly small compared to the mass of the surrounding gas swept by the shock. Second the maximum pressure of the blast wave front must be much greater than the ambient pressure. According to Taylor [40], the similarity solution for an ideal strong blast wave remains valid if the maximum overpressure is greater than a factor of 10. For a strong blast wave the overpressure is represented by the following equation [41].

$$\frac{\Delta p}{p_\infty} = \frac{2\gamma}{\gamma + 1} M_s \tag{4.1}$$

where Δp is the pressure increase in the compressed gas, p_∞ and γ are the pressure and the specific heat ratio of the ambient gas, respectively, and M_s is the Mach number of the shock wave. In addition, blast wave theory applies only for one dimensional flows, either spherical, cylindrical, or plane propagation.

The propagation of a strong blast wave was investigated analytically by Taylor [40] and Sedov [42] using the similarity method. The solution by Sedov is:

$$r_s = \left(\frac{\alpha E_0}{\rho_\infty}\right)^{1/(n+2)} t^{2/(n+2)} \tag{4.2}$$

where r_s is the location of the shock wave in the spatial coordinate, E_0 is the energy incorporated into the blast wave, ρ_∞ is the density of the undisturbed ambient gas, t is the elapsed time from the instance of explosion, α is a constant, and n is 3, 2, and 1 for spherical, cylindrical, and plane propagation, respectively. From Eq. (4.2), the velocity of the shock wave is derived as

$$c_s = \left(\frac{2}{n+2}\right)\left(\frac{\alpha E_0}{\rho_\infty}\right)^{1/2} \frac{1}{r_s^{n/2}} = \left(\frac{2}{n+2}\right)\left(\frac{\alpha E_0}{\rho_\infty}\right)^{1/(n+2)} \frac{1}{t^{n/(n+2)}} \tag{4.3}$$

where c_s is the propagation speed of the shock wave. Eq. (4.2) is the expression used to estimate the laser induced blast wave energy with the assumption that the blast wave is sufficiently intense. Specifically, when the distance traveled by the shock wave, $r_{s,e}$, and the corresponding elapsed time, $t_{,e}$, are measured experimentally the blast wave energy E_0 can be directly found by substituting these values into Eq. (4.2). In other cases, either Eq.

(4.2) or (4.3), is used to investigate whether the time-of-propagation data agree with the predictions from blast wave theory [13,20,21].

4.4 Results and discussion

4.4.1 Deflection of the probe beam for the early period (0 <t<10 μs)

The deflection profile of a probe laser beam obtained from nanosecond pulsed laser heating of a metal target consists of a fast component and a slow component. Generally speaking, the faster part includes deflection of the probe beam approximately for the first 10 μs after the heating laser pulse. The slower part of a deflection signal can be from about 40-50 microseconds to about a millisecond depending on the intensity of the laser power and the normal offset of the probe beam. Because the characteristics of a deflection signal in these two time periods are very different, the fast component of the deflection signal is discussed first in this section and the slower component will be discussed in the following section.

The experimental parameters for a probe beam deflection measurement that possibly make the measured response look significantly different are the normal offset of the probe beam, the laser power density, and the pressure of the ambient gas. The variation of time-response of the probe beam with respect to the changes of these parameters is very important for understanding the fundamental mechanisms during laser ablation when using the probe beam deflection measurement technique. Therefore in the following sections, the variation of deflection time-response for each of these parameters

will be examined. Again all the deflection measurements shown in the following sections are made for single-pulse laser heating of polished aluminum targets, unless otherwise specified.

4.4.1.1 Characteristics of the deflection produced by a shock wave

In the following discussion, the experimental parameters are denoted as follows; the normal offset of the probe beam by Z_0 (shown in Fig. 4.1), the laser pulse energy by E_p, the laser power density by P_p, and the laser spot size by d_s.

Fig. 4.4 shows the deflection time-response of the probe beam for the early period for different normal offsets. The measurements were performed at atmospheric pressure. The laser pulse energy between each profile in Fig. 4.4 varies (due to fluctuation) within 6%. Accurate measurement of the laser beam spot size at the target surface is very difficult for high power pulsed laser heating. In this study, it is approximated that the laser spot size varies linearly between the focusing lens and the focal point. Thus the variation of the power density in Fig. 4.4 due to the uncertainty of the laser spot size is expected to be about 10-15 %. For the calculation of laser power density, the FWHM of the excimer laser pulse (21 ns) is used. In Fig. 4.4, the decrease of signal intensity corresponds to the deflection of the probe beam toward the target surface and is defined as the negative deflection for the rest of this chapter. Similarly, the deflection with increasing signal intensity is defined as the positive deflection.

The deflection profiles for small normal offsets in Fig. 4.4 (Z_0=0.25 or 0.51 mm) show different characteristics from those for larger normal offsets (Z_0=1.02 mm or

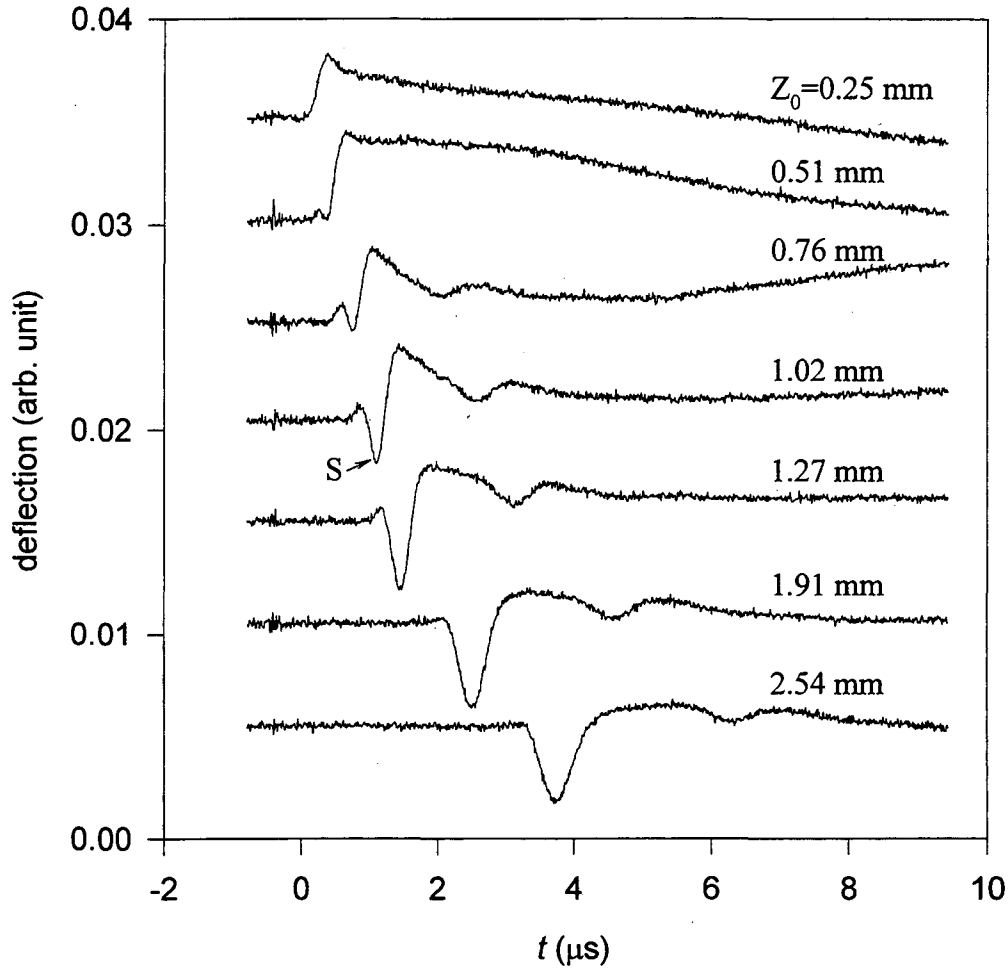

Fig. 4.4 Deflection time-response profiles measured in air for different normal offsets of the probe beam (E_p=7 mJ, P_p=2.0 x10^7 W/cm^2)

greater). The deflection for a small normal offset is always positive and the amplitude decreases slowly with time. As the normal offset of the probe beam increases, a negative deflection starts to appear at the leading portion of the deflection time-response profiles (indicated by the letter 'S' in Fig. 4.4) and grows further in the negative direction with increasing Z_0. Based on repeated measurements, the deflection profile transforms gradually from a completely positive response to one with a sharp negative peak, as the normal offset of the probe beam is increased. For normal offsets greater than 1 mm, the deflection response shows in principle the same pattern, i.e. a strong and short negative deflection followed by a longer positive deflection. When the normal offset of the probe beam is divided by the elapsed time at the beginning of deflection, the average propagation velocity of the fastest characteristic of the laser induced flow can be obtained. The average velocity varies from 2780 m/s to 760 m/s for those deflection profiles shown in Fig. 4.4. Since a shock wave can form immediately after the laser heating of a solid target and is always ahead of the compressed air and the contact surface, the most probable characteristic that propagates at this speed during laser ablation is the shock wave. To confirm that this deflection is due to a shock wave, the deflection patterns of a probe beam by a propagating shock wave are simulated below with a simplified model.

Probe beam deflection by a expanding spherical shock wave

i) Deflection of a single ray of light by an ideal spherical blast wave

First we consider the deflection of a single ray of light due to a spherical shock wave (see Fig. 4.5). Because a shock wave is a discontinuity to the gas in front of the shock front, the refractive index as well as gasdynamic properties vary discontinuously across the shock wave. Thus when a ray of light from the undisturbed gas is incident on the shock front, it experiences a refraction at the shock front due to the change of refractive index. The exit angle, θ_2, of the ray which is incident with an angle θ_1 with respect to the normal on the shock front is determined by Snell's law as

$$\frac{\sin\theta_1}{\sin\theta_2} = \frac{n_s}{n_\infty} \tag{4.4}$$

where n is the refractive index and the subscripts ∞ and s represents the undisturbed gas and the shock front, respectively. Using the distance of the ray from the target surface and the radius of the shock hemisphere, θ_1 can be represented by

$$\theta_1 = \sin^{-1}\left(\frac{Z_0}{r_s}\right) \tag{4.5}$$

The dependence of the refractive index of light at a particular wavelength on the density, ρ, is represented by the Lorentz-Lorenz formula [43]

$$\frac{n^2-1}{n^2+2} = A_m \rho \tag{4.6}$$

where A_m, the molar refractivity (cm^3/mole), is expressed for gases by

$$A_m = \frac{RT}{p}\frac{n^2-1}{3} \tag{4.7}$$

where R is the gas constant, T is temperature, and p is pressure. Thus using Eq. (4.6), the refractive index at the shock front becomes:

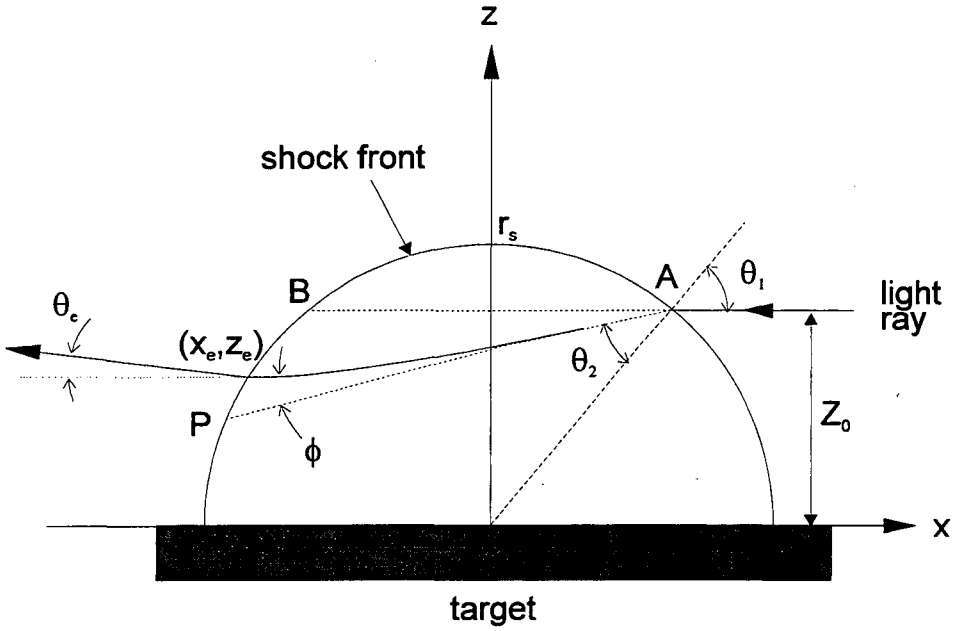

Fig. 4.5 Schematic diagram for the deflection of a single ray of light due to an ideal spherical blast wave

$$n_s = \sqrt{\frac{2A_m\rho_s + 1}{1 - A_m\rho_s}} \tag{4.8}$$

The density behind the shock front for a strong blast wave was given by Sedov [42] as

$$\rho_s = \frac{\gamma + 1}{\gamma - 1}\rho_\infty \tag{4.9}$$

Inside the shock hemisphere is a field with continuous and discontinuous changes. Analytical expressions for the propagation of compressed gas, contact surface, and the vapor and for the distribution of properties in each region are unavailable. For a strong blast wave, however, Sedov [42] obtained the analytical solution, which is employed in the present model, for the distribution of gasdynamic properties behind the shock wave using the similarity method. Sedov's similarity solution for the density distribution for a spherical explosion is shown in dimensionless form in Fig. 4.6. Assuming that the density field behind the laser generated shock wave can be approximated by the solution shown in Fig. 4.6, the deflection of the light ray inside the shock hemisphere, ϕ in Fig. 4.5, is obtained as follows. Since the angle (θ_1-θ_2) in Fig. 4.5 is small, of the order of milliradians (note that this angle is extremely exaggerated in Fig. 4.5), and the diameter of the shock hemisphere is only a few mm for laser heating, we make the approximation that $\overline{AB} \cong \overline{AP}$ in Fig. 4.5. Then the deflection angle by the density field inside the shock hemisphere is obtained by the following equation (see Appendix);

$$\phi = \frac{1}{n_0}\int_{\overline{AB}} \frac{dn}{d\rho}\frac{\partial\rho}{\partial z}ds \tag{4.10}$$

where $dn/d\rho$ and $\partial\rho/\partial z$ are found from Eq. (4.6) and Fig. 4.6, respectively. For the density field given by Fig. 4.6, the deflection ϕ computed from Eq. (4.10) is always positive

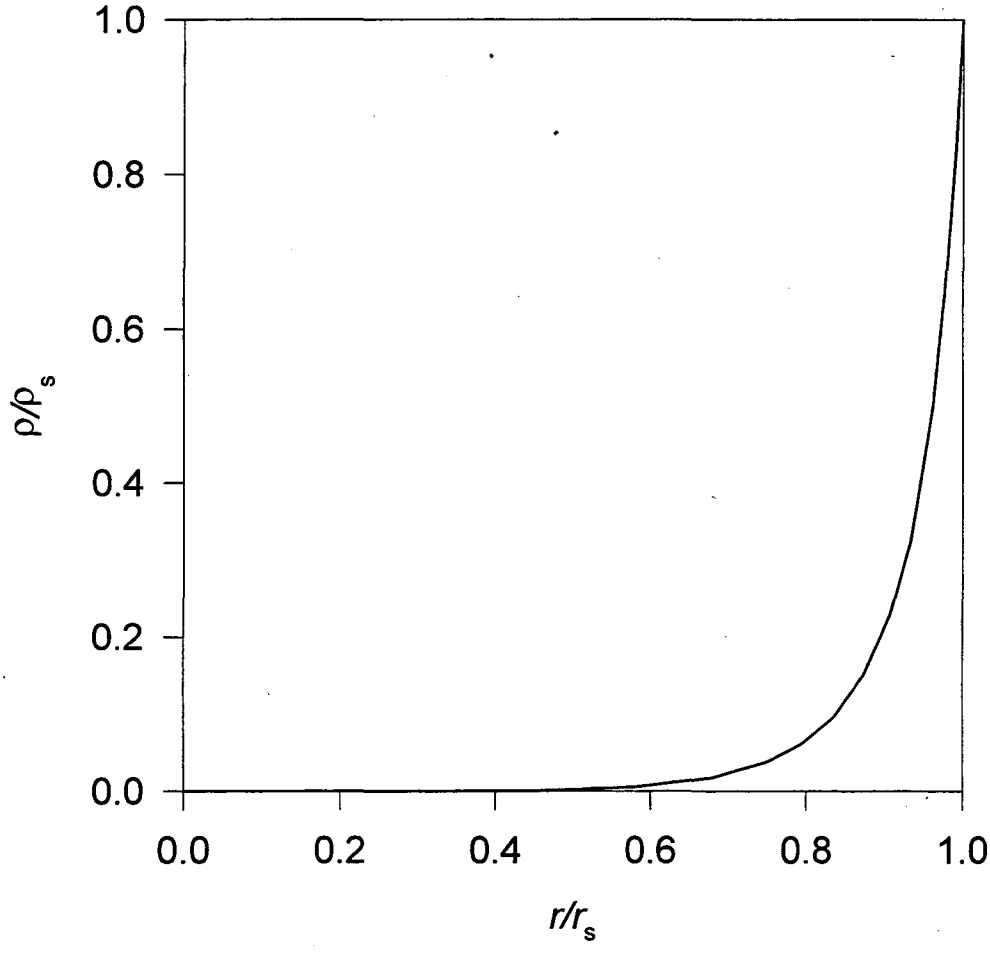

Fig. 4.6 Density distribution behind the shock for an intense spherical blast wave obtained by Sedov's similarity method [42] (γ=1.4)

because the deflection of light always occurs toward the field with a higher density (i.e. a higher refractive index). From the deflection angles θ_2 and ϕ, the location (x_e, z_e) and the angle θ_e as the ray leaves the shock hemisphere are obtained. Using (x_e, z_e) and θ_e, the position of the ray along the probe beam direction, where the detector is located, is found.

ii) Deflection of a Gaussian beam having a finite diameter

The deflection of a Gaussian beam having a finite diameter can be approximated by dividing the beam into many slices. With the known distribution of the beam intensity, the resultant deflection that is measured on the detector can be approximated by the superposition of the deflection of each beam slice. It is assumed that the center of the Gaussian beam passes over the center of explosion so that the deflection of each beam slice occurs only in the direction normal to the target surface.

iii) Computed deflection of a Gaussian beam using Sedov's solution

The computed deflection of a Gaussian beam due to a density field described by Eq. (4.9) and Fig. 4.6 (Sedov's self-similar solution) is shown in Fig. 4.7. The propagation of the blast wave is simulated by gradually increasing the radius of the shock. For the calculations, the diameter of the Gaussian beam and the distance from the center of explosion to the knife edge are taken to be 100 μm and 40 mm, respectively. The undisturbed gas is air at atmospheric pressure and 300 K. The density increase at the shock front represented by Eq. (4.9) and the dimensionless density profile behind the shock wave represented from Fig. 4.6 are assumed to remain the same during the

expansion of the shock wave. By introducing the propagation speed of the shock wave, Fig. 4.7 can be transformed to deflections in time. From Eq. (4.3), the velocity of the shock for a spherical blast wave is represented by

$$c_s = \frac{2}{5}\left(\frac{1.175E_0^*}{\rho_\infty}\right)^{1/5} t^{-3/5} \tag{4.11}$$

where α=1.175 [42] has been used. To use Eq. (4.11), it is necessary to know the energy released into the blast wave E_0^*, where E_0^* is $0.5E_0$ because a laser induced blast wave is hemispherical. The result for E_0^*=5 mJ is presented in Fig. 4.8. The deflection profiles when the density decrease behind the shock wave is omitted from the calculations (which is equivalent to the condition that the density inside the shock hemisphere is uniform and equal to ρ_s) are shown in Fig. 4.9. With no density decrease behind the shock wave, the computed deflection is completely negative. This implies that the density jump at the shock front produces only a negative deflection of the probe beam.

The computed deflection for the probe beam close to the surface, for example Z_0=0.5 mm in Fig. 4.8, shows a positive deflection only which implies that the deflection of the probe beam for this value of Z_0 is dominated by the density decrease behind the shock. Note that, for the computed deflections, the density jump at the shock front is responsible for the negative deflection and the density decrease behind the shock wave is for the positive deflection. As Z_0 increases, a negative deflection appears in the leading portion of the computed deflections (indicated by the letter 'S' in Fig. 4.8) and becomes larger for a greater Z_0. This behavior implies that with increasing distance from the target the deflection due to the density jump at the shock front becomes more dominant for the

initial deflection in time while that due to the density gradient behind the shock becomes smaller.

The computed deflections in Fig. 4.8 closely reproduce the observed trends of the measured deflections in Fig. 4.4 with increasing distance of the probe beam from the target surface. Both computed and measured deflections show a completely positive deflection of the probe beam for small values of Z_0 and a negative deflection at the leading portion of the temporal deflection profiles for large values of Z_0. The gradual change of the temporal deflection profiles from a completely positive signal to one with a sharp negative peak with respect to the increasing Z_0 also agrees well between the computed and measured deflections. Note that we are only discussing the trends of the temporal variation of the probe beam deflection. The computed deflection pattern behind the negative peak does not agree with the measured data; this is not surprising in view of the large difference between the laser induced blast wave and the computational model employed.

From these results, it is possible to explain the change of time-response (in the leading portion) of the measured deflections with respect to the increasing Z_0 as a result of the density variation near the shock wave. When the radius of the shock wave is small, corresponding to the period immediately after the explosion, the density decrease behind the shock is very large and is responsible for the deflection of the probe beam. As the blast wave proceeds, the density gradient behind the shock decreases and the negative deflection gradually becomes greater.

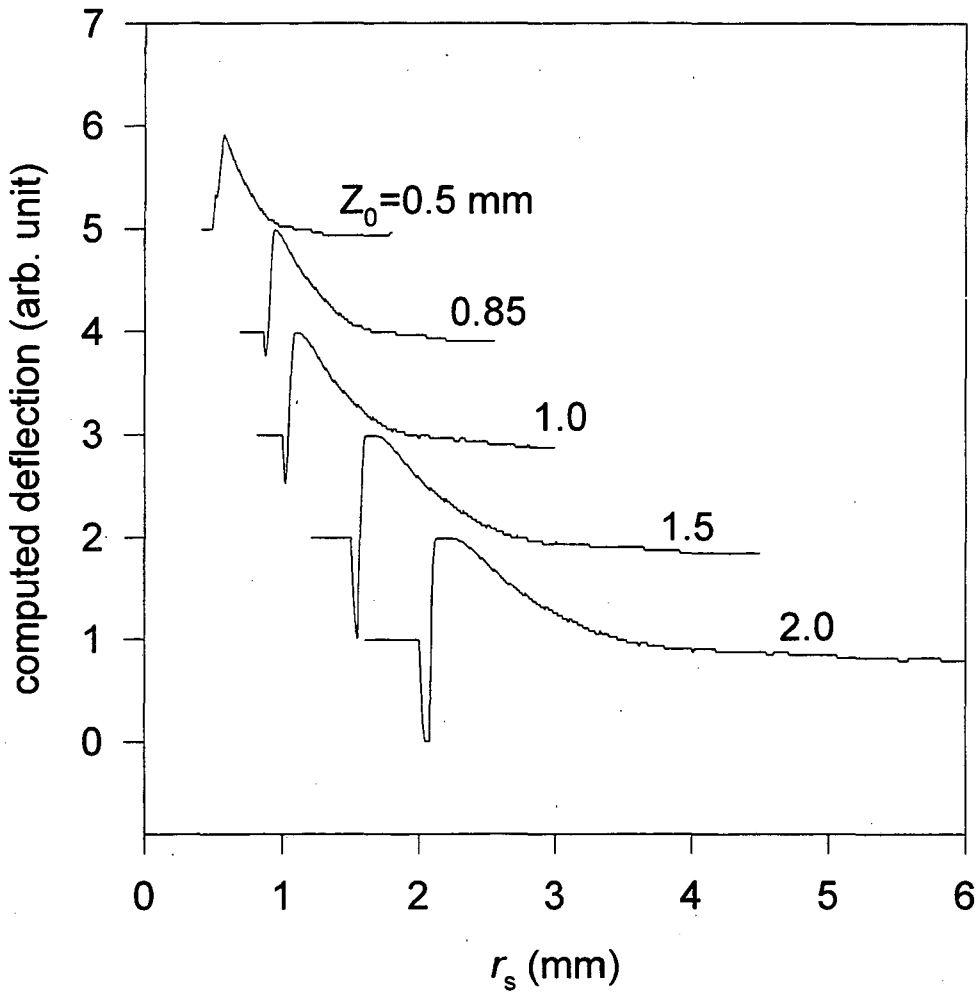

Fig. 4.7 Computed deflection of a Gaussian beam due to an ideal spherical blast wave. Self-similar solution by Sedov [42] is used to calculate the density distribution.

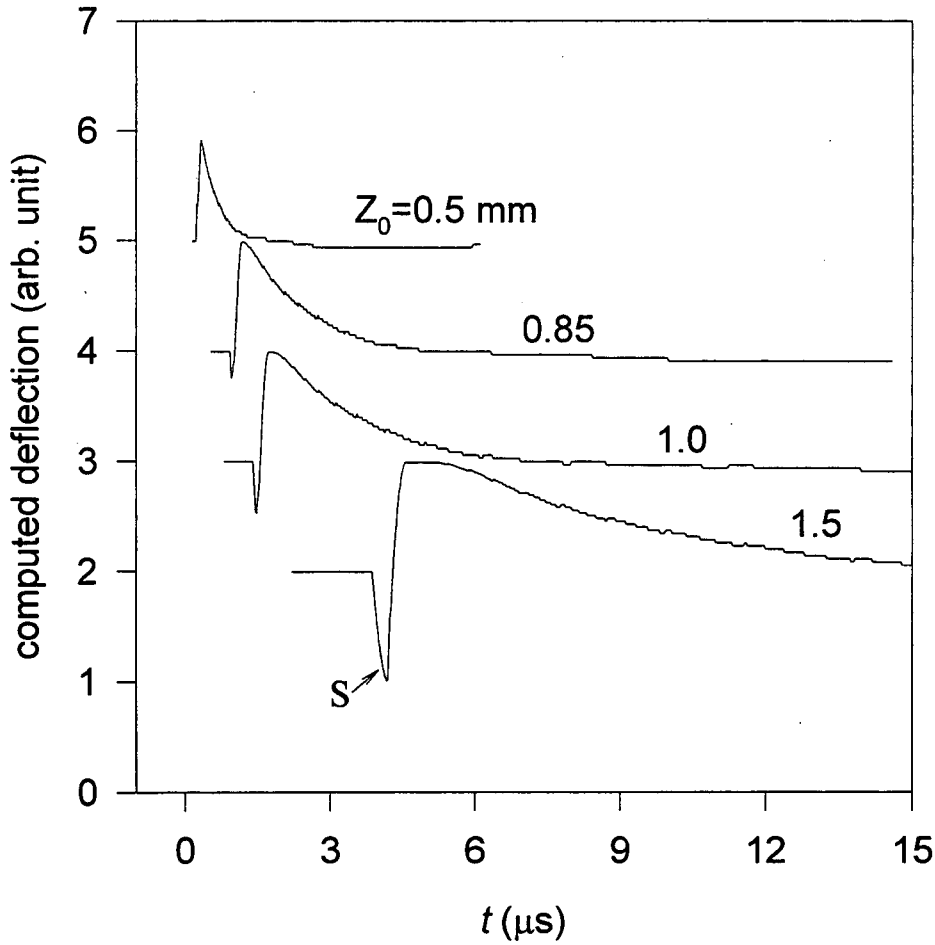

Fig. 4.8 Computed deflection of a Gaussian beam with time. The results in Fig. 4.7 are reformed using Eq. (4.11) with E_0^*=5 mJ

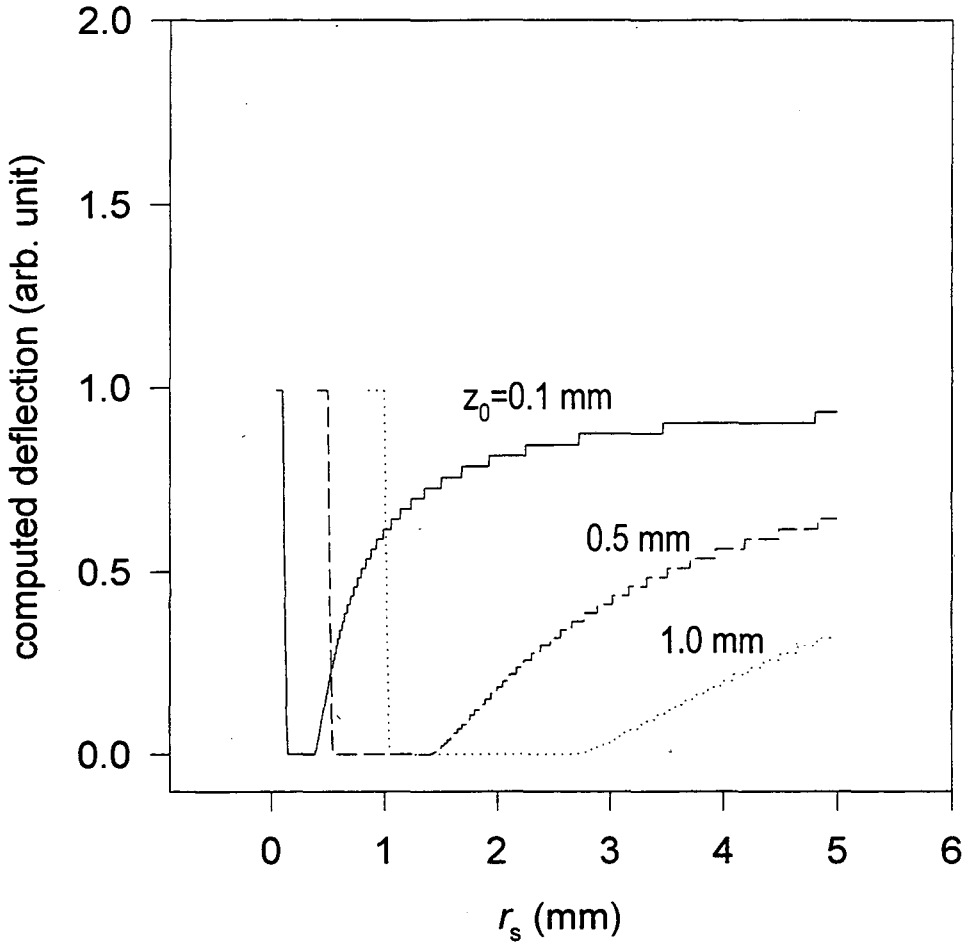

Fig. 4.9 Computed deflection when the density decrease behind the shock wave is omitted

The time from the initiation of the blast wave until the shock wave reaches the probe beam height is defined as the time-of-propagation of a laser induced shock wave in the rest of this thesis. It is observed from the computed deflections that the beginning of the positive deflection for small Z_0 or the beginning of the negative deflection for large Z_0 corresponds to the time at which a shock wave reaches the probe beam height. Accordingly, the time-of-propagation of a shock wave in the measured deflection time-response profiles, Δt_1, is defined by the same manner as shown in Fig. 4.10. This definition is also consistent with the fact that a shock wave propagates at the outermost front of a blast wave.

4.4.1.2 Time-of-propagation of the shock

The variation of the time-of-propagation of the laser induced shock wave, Δt_1 in Fig. 4.10, with respect to the major experimental parameters, i.e. laser pulse energy, ambient pressure, and the propagation distance of the shock, is examined below.

Pulse energy of the heating laser

The effect of pulse energy of the heating laser beam on Δt_1 is shown in Fig. 4.11. The measurements are made for single pulse heating of an aluminum target in air. The distance between the probe beam and the target surface is 2 mm. For this value of normal offset, the deflection time-response consists of a sharp negative peak and a following positive peak (similar to the one for Z_0=1.91 mm in Fig 4.4). The laser pulse energy E_p

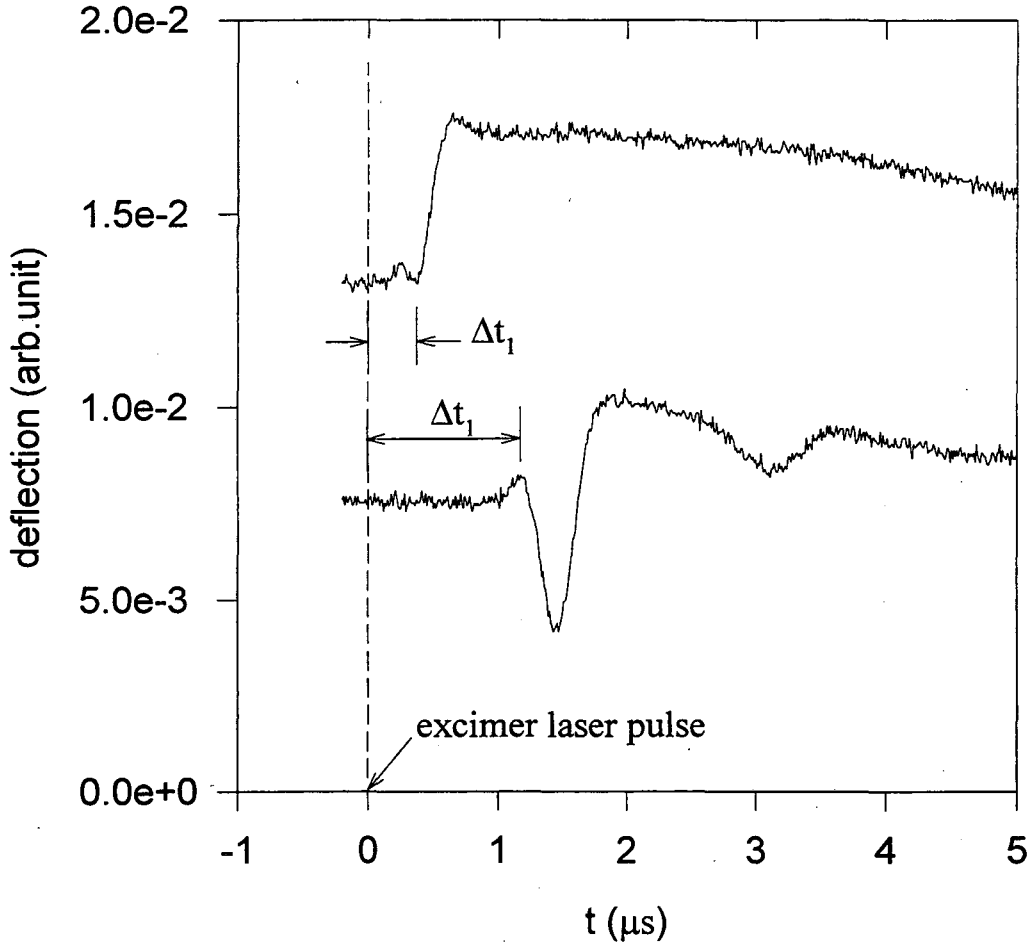

Fig. 4.10 Time-of-propagation, Δt_1, of the shock wave for measured deflection signals (the curves for Z_0=0.51 and 1.27 mm in Fig. 4.4 are reshown)

varies from 4 to 10 mJ for the data in Fig. 4.11 which corresponds to the laser power density P_p from 5.6 to 14.0×10^6 W/cm^2 while other experimental conditions remain the same. The amplitude of the negative deflection increases with increasing laser pulse energy. The time-of-propagation of the shock for these measured deflection response decreases with laser pulse energy. Since a higher pulse energy results in a larger saturation pressure of the vapor at the target, the propagation of the laser induced shock wave at a greater E_p is expected to be faster. From Eq. (4.2), Δt_1 is found to be proportional to $(E_p)^{0.5}$ for an ideal blast wave. The curve in Fig. 4.11 represents a fitting of the experimental data in the figure; using this dependence on E_p the relation is $\Delta t_1=8.32(E_p)^{0.5}$ which closely follows the experimental data. It is noted, however, that the data may also be fitted fairly well with a linear regression. The consistency of the measured data with ideal blast wave theory is further examined in the following sections.

Ambient pressure

The speed of the shock varies significantly with the ambient pressure [11,28]. The variation of Δt_1 with respect to the ambient pressure is presented in Fig. 4.12. Z_0 and E_p are 2 mm and 10±0.5 mJ, respectively. The time-of-propagation decreases with decreasing ambient pressure. The decrease of time-of-propagation, or equivalently increase of the shock wave velocity with decreasing ambient pressure, was also reported by Gupta et al. [11] for an excimer laser ablation of $YBa_2Cu_3O_{7-\delta}$ targets and by Azzeer et al. [28] for a laser generated shock wave in air. According to Eq. (4.2), the decrease of the time-of-propagation with decreasing ambient pressure is expected for an ideal blast wave.

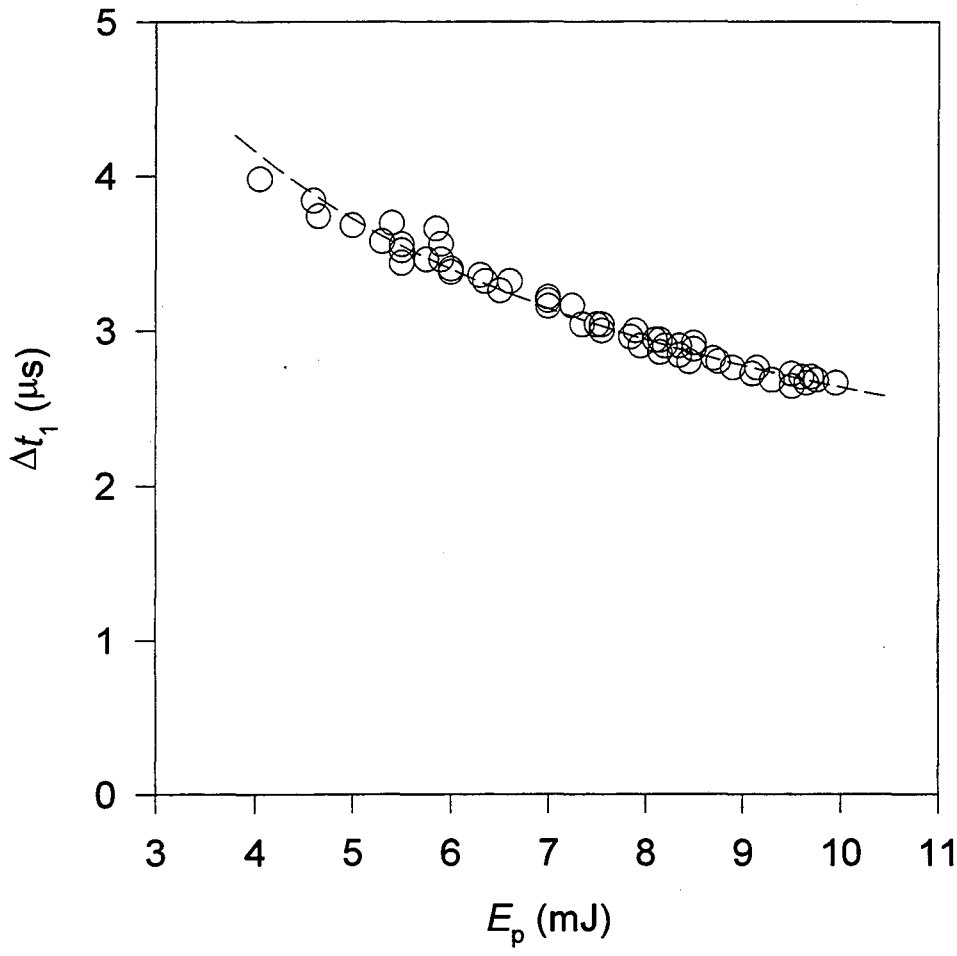

Fig. 4.11 Time-of-propagation of the shock wave with respect to the pulse energy of the heating laser (Z_0=2 mm)

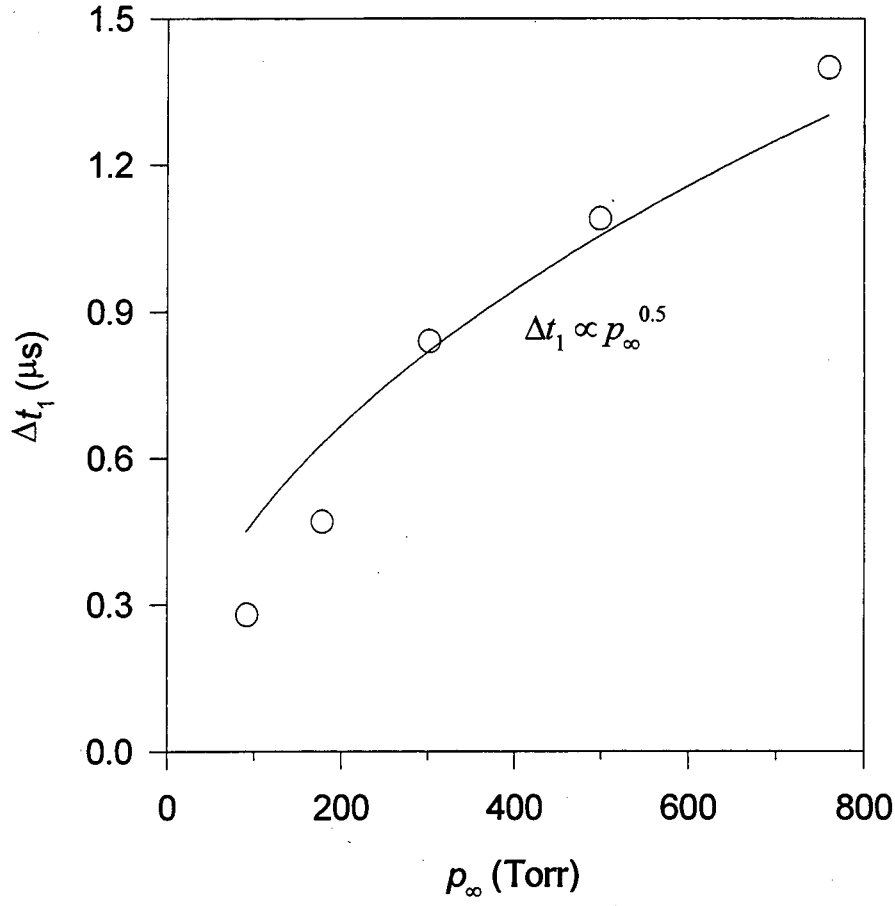

Fig. 4.12 Time-of-propagation with respect to ambient pressure (E_p=10 mJ, Z_0=2 mm)

From Eq. (4.2), the relationship between the ambient pressure and the time-of-propagation for an ideal blast wave is found to be $\Delta t_1 \propto (p_\infty)^{1/2}$. The experimental results in Fig. 4.12, however, fit better with the relation $\Delta t_1 \propto (p_\infty)^{0.7}$ implying a possible difference between a laser induced blast wave and an ideal blast wave.

Propagation distance of the shock wave

The variation of the time-of-propagation of the shock wave with propagation distance, Δt_1, is frequently used in comparing ideal blast wave theory with experimental results from a laser induced blast wave. In Fig. 4.13, the deflection time-response at an ambient pressure of 300 Torr are shown for the same range of normal offsets as shown in Fig. 4.4 for which the ambient pressure is 760 Torr. The experimental conditions for Fig. 4.13 differs from that in Fig. 4.4 only in the ambient pressure. Note that the deflection time-response in Fig. 4.13 for small normal offsets, Z_0=0.25 and 0.51 mm, show a negative deflection at the beginning of the deflection in time instead of the positive deflection observed in Fig. 4.4. Since it has been previously established that the negative deflection is due to the density increase at the shock wave front, this reflects that a relatively stronger shock wave forms at lower ambient pressures. The strength of a shock wave can be estimated from the overpressure of the shock wave which is computed from Eq. (4.1) for a strong blast wave. The overpressure for Z_0=0.25 mm is 12 and 27 for p_∞=760 and 300 Torr, respectively. Therefore a stronger discontinuity is expected at the shock front for p_∞= 300 Torr; which may be the reason for the initial negative deflection for the small offsets in Fig. 4.13.

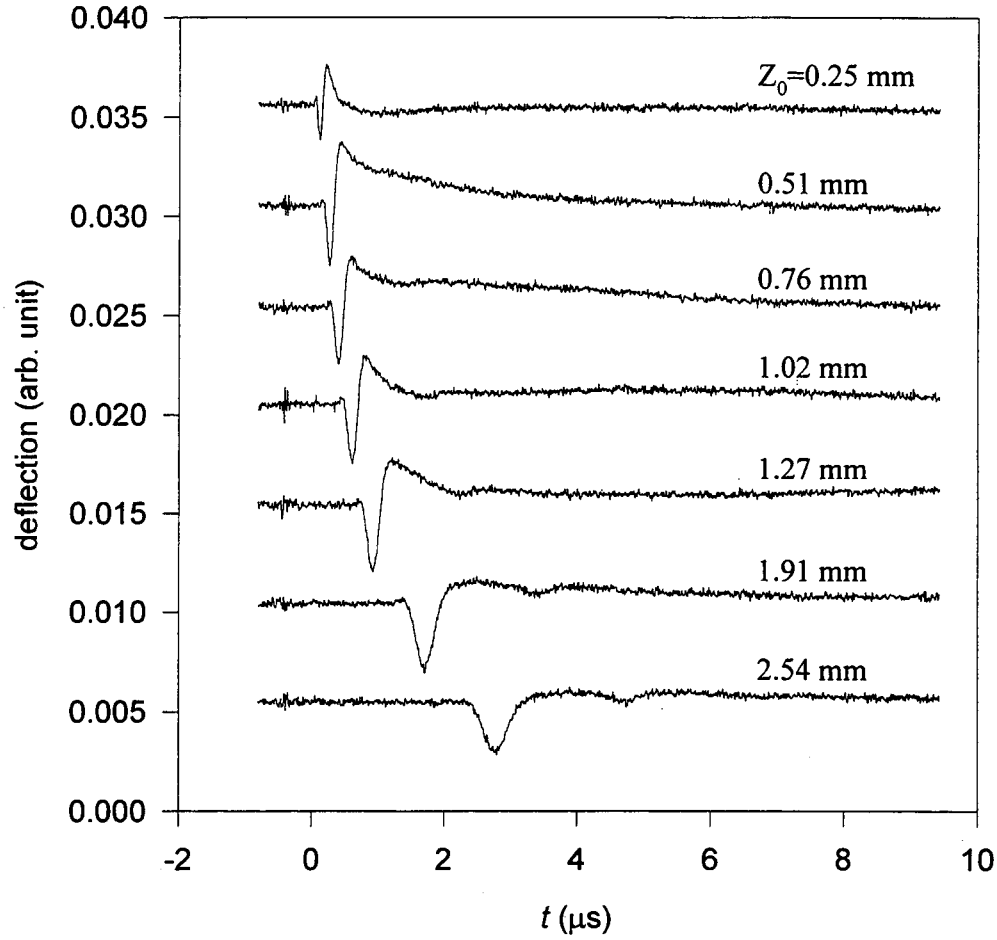

Fig. 4.13 Deflection time-response profiles at reduced ambient pressure for different values of Z_0 (p_∞=300 Torr, E_p=7 mJ, P_p=2.0x10^7 W/cm^2)

The time-of-propagation values from the data in Fig. 4.4 and 4.13 are presented in Fig. 4.14. The velocity of the shock in Fig. 4.14 is the local velocity computed from the derivative of a polynomial fit to the time-of-propagation data. In order to fit the data closely, the polynomial equation $\Delta t_1 = a_1 x + a_2 x^2$ is used instead of the blast wave equation. with propagation distance. At a given p_∞ the time-of-propagation data deviate significantly from the behavior predicted by the similarity solution, i.e. $\Delta t_1 \propto r_s^{2.5}$ in Eq. (4.2). The absolute discrepancy is greater for the ambient pressure of 760 Torr.

The time-of-propagation data for p_∞= 300 Torr are compared with the relationship predicted by the results from the similarity solution for a spherical shock and for a plane shock. The relationship for a spherical and for a plane shock from Eq. (4.2) is $\Delta t_1 \propto r_s^{2.5}$ and $\Delta t_1 \propto r_s^{1.5}$, respectively. The measured data are best fitted by $\Delta t_1 \propto r_s^{1.7}$ as shown in Fig. 4.15(a); thus the time-of-propagation data are closer to the propagation of a plane shock. Since a laser induced shock is expected to become more spherical with increasing propagation distance, the data for large propagation distances may exhibit a stronger spherical blast wave behavior. To examine the behavior of the shock near the target surface, the time-of-propagation data for small Z_0 only are fitted again with the relationship for spherical and plane shocks, see Fig. 4.15(b). For the data close to the target surface, the time-of-propagation data agree closely to the plane surface equation. From these results, it is clear that near the target the propagation of the shock is almost planar.

Whether the propagation is planar or spherical depends upon the laser spot size. If the laser spot is much smaller than the distance between the target surface and the probe

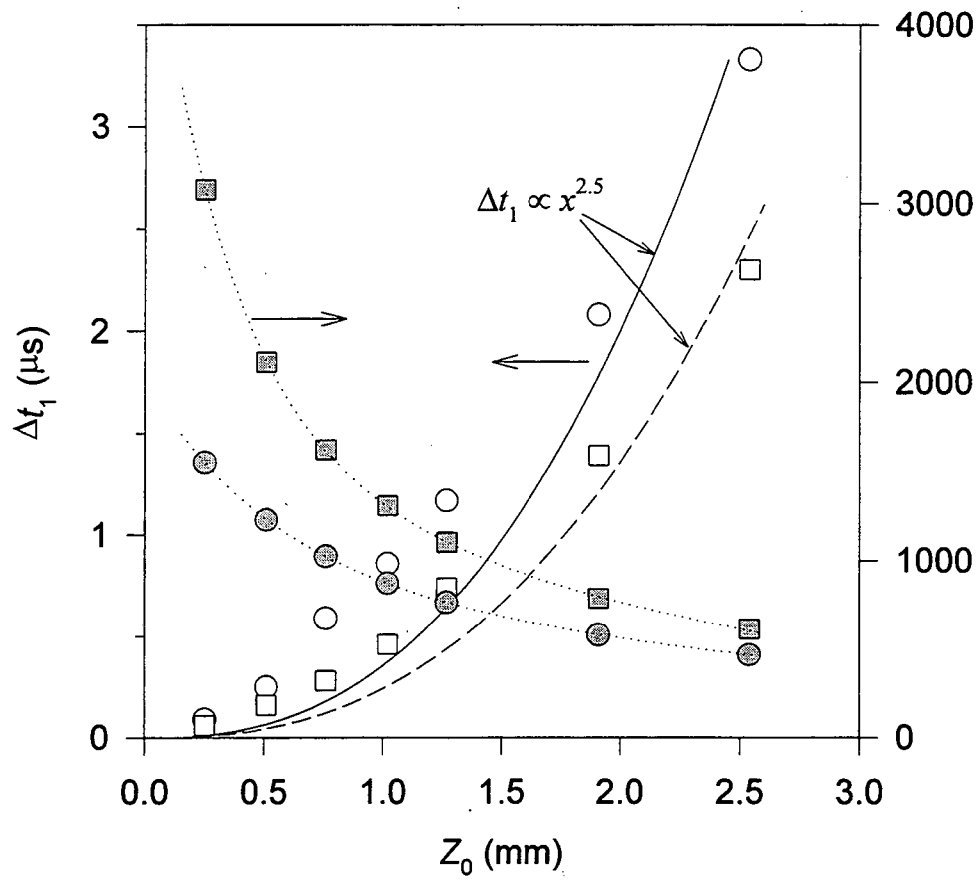

Fig. 4.14 Time-of-propagation of the shock wave for different ambient pressures, 300 and 760 torr. The velocity of the shock wave is computed from the derivative of the closest polynomial fit ($\Delta t_1 = a_1 x + a_2 x^2$) to the time-of-propagation data. (circle: 760 Torr, square: 300 Torr)

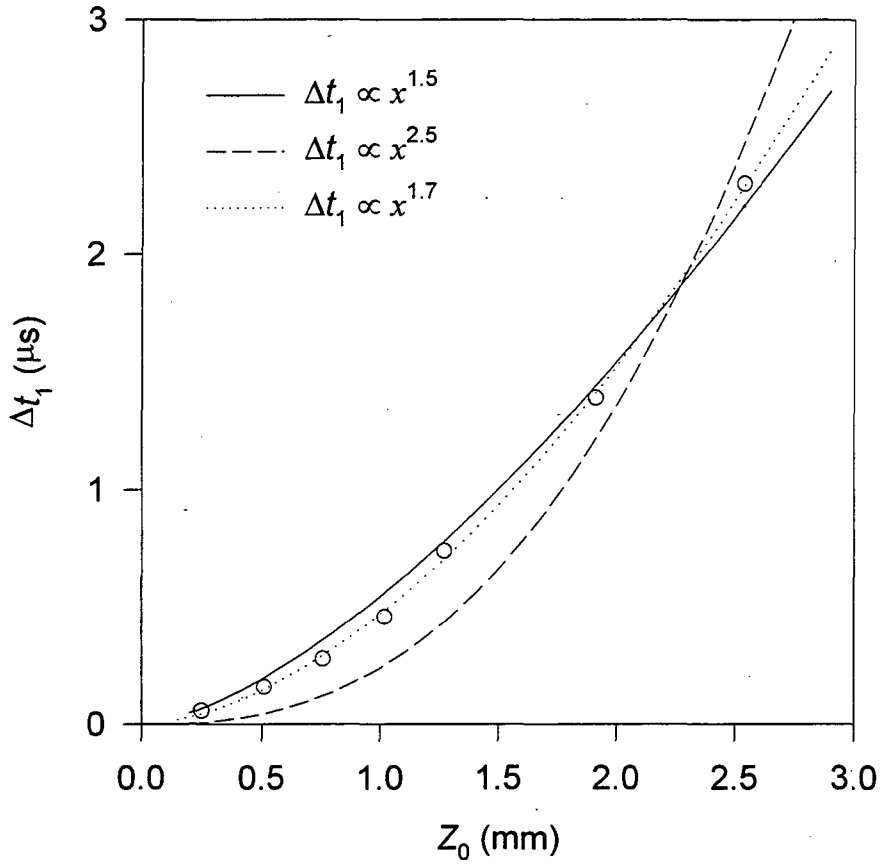

Fig. 4.15(a) Comparison of the time-of-propagation data for p_∞=300 Torr in Fig. 4.14 with the relationship predicted by the similarity solution for an ideal blast wave

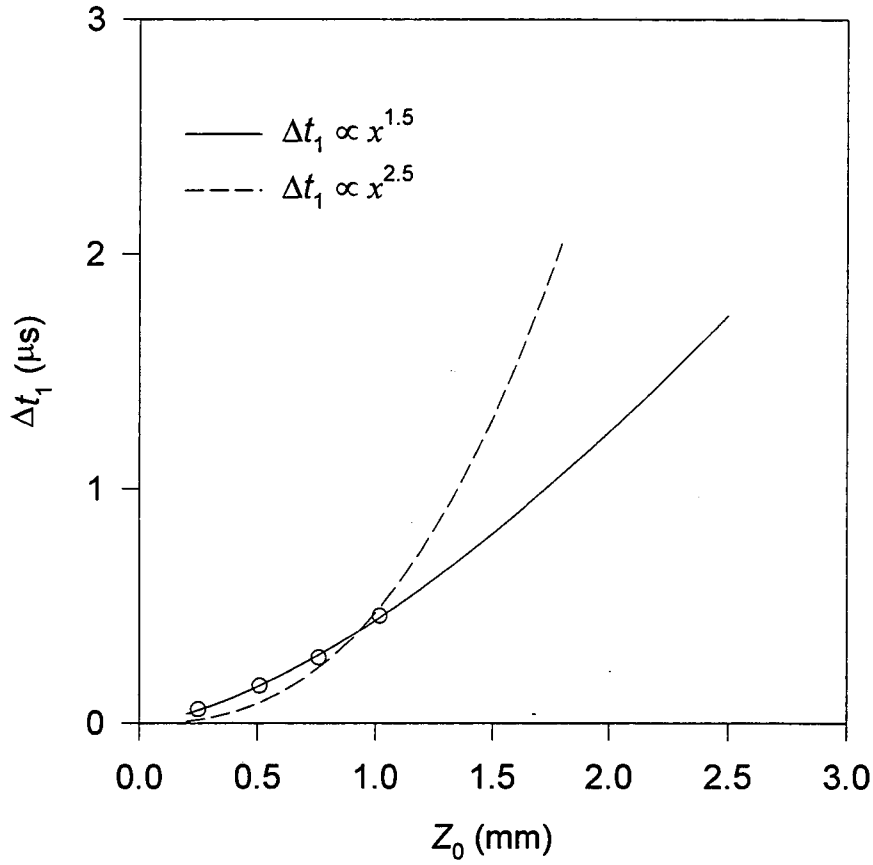

Fig. 4.15(b) Comparison of the time-of-propagation data for small Z_0 in Fig. 4.15(a) with the relationship predicted by the similarity solution for a plane and a spherical blast wave.

beam, the measured shock should show the characteristics of a spherical shock. For the data shown in Fig 4.14 and 4.15, the laser spot size is approximately 1.5 mm. Fig. 4.15(b) indicates that for this laser spot size, the propagation of the shock within the distance of 1 mm from the target surface is almost planar. This kind of planar expansion for large laser spot sizes was also observed by Gupta et al. [11] and Dyer et al. [12] using photographic techniques. Dyer at el. showed that the velocity of the shock in the direction normal to the target surface was twice than that in the direction parallel to the target surface.

The time-of-propagation of the shock wave with respect to the laser spot size is investigated in Fig. 4.16, where the laser spot sizes at the target surface are approximately 1.5 and 0.5 mm. The experiments were performed in atmospheric air. The laser pulse energy remains the same for the experiments and thus the laser power density is different for both cases, which is 2×10^7 and 1.7×10^8 W/cm^2 for d_s=1.5 and 0.5 mm, respectively. As expected, it is clearly observed from Fig 4.16 that the data for the smaller spot size of d_s= 0.5 mm follow more closely the theoretical prediction of a spherical blast wave than those for d_s=1.5 mm.

The similarity solution of a spherical blast wave, Eq. (4.2) is based on the assumptions that i) the blast wave is generated from a point explosion and ii) the ambient pressure is negligibly small compared to the pressure behind the shock. From the results shown in Figs. 4.14-4.16, it is clear that the time-of-propagation of the shock agrees more closely with the similarity solution when the experimental conditions are closer to these assumptions, i.e. for a smaller laser spot size and a lower ambient pressure. Results for the time-of-propagation measurements when the ambient pressure is reduced to 300 Torr

and the laser spot size is kept at the small value of 0.5 mm are shown in Fig. 4.17. The data for p_∞=760 Torr and d_s=0.5 mm are also shown for comparison. For p_∞= 300 Torr and d_s=0.5 mm, the theoretical relation $\Delta t_1 \propto r_s^{2.5}$ is in excellent agreement with the time-of-propagation data.

In studies of laser induced shock wave, blast wave theory is often employed [9,11,15,17,20,21] without clearly specifying under what conditions this theory is applicable. It is sometimes simply stated that the data from the location closer to the target surface are more reasonable for the comparison with the theoretical blast wave solution [9,21]. From the present study, it is found that the data close to the target, or those for earlier time, do not necessarily follow the behavior predicted by spherical blast wave theory. Actually, the data closer to the target show the characteristics of a planar blast wave. Indeed, laser spot size and ambient pressure should be considered in determining the applicability of ideal spherical blast wave theory to the laser generated blast wave. For the experimental conditions of this work, i.e. excimer laser heating of a polished aluminum target with the laser power density of 1.7×10^8 W/cm^2, the laser spot size and ambient pressure of 0.5 mm and 300 Torr, respectively, produce time-of-propagation data which closely follow the theoretically predicted behavior. These conditions may vary with the target material and the laser power density.

It is observed from Fig. 4.16 that the local velocity of the laser induced shock decreases very fast over small distances from the target surface. It should be noted that the local velocity of the shock wave is different from the average velocity obtained by

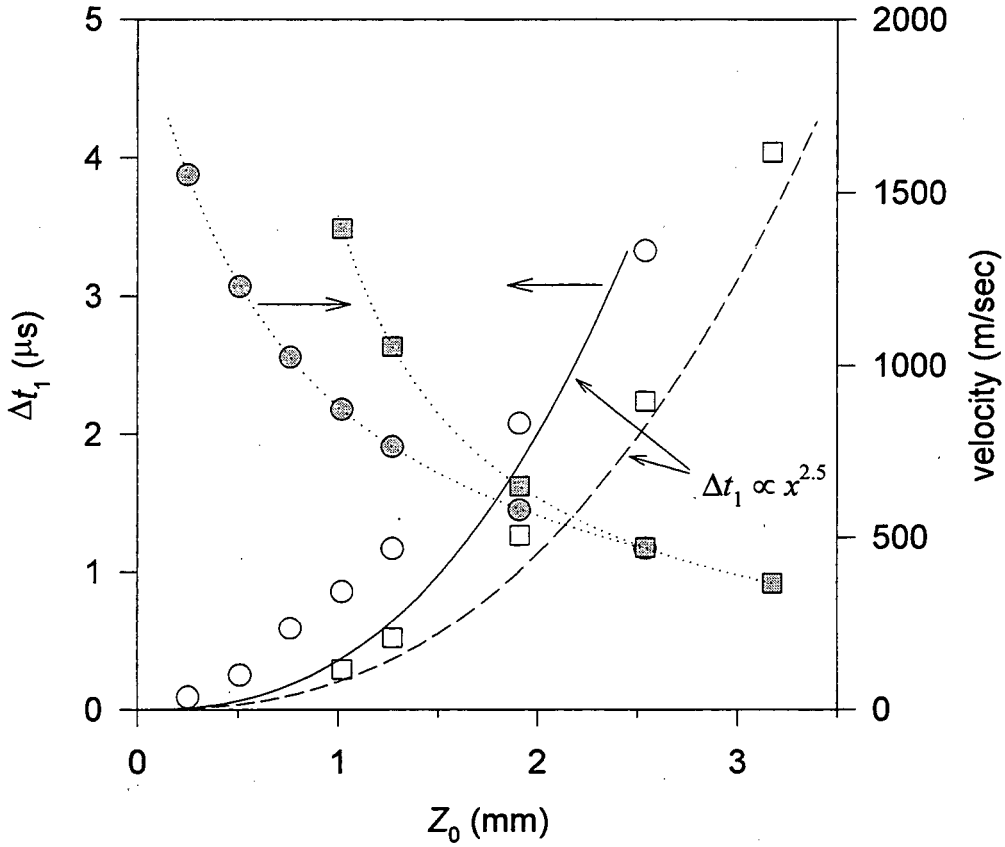

Fig. 4.16 Time-of-propagation of the shock wave for different laser spot sizes, 1.5 and 0.5 mm at atmospheric pressure. The velocity of the shock wave is computed from the derivative of the closest polynomial fit ($\Delta t_1 = a_1 x + a_2 x^2$) to the time-of-propagation data. (circle: 1.5 mm, square: 0.5 mm)

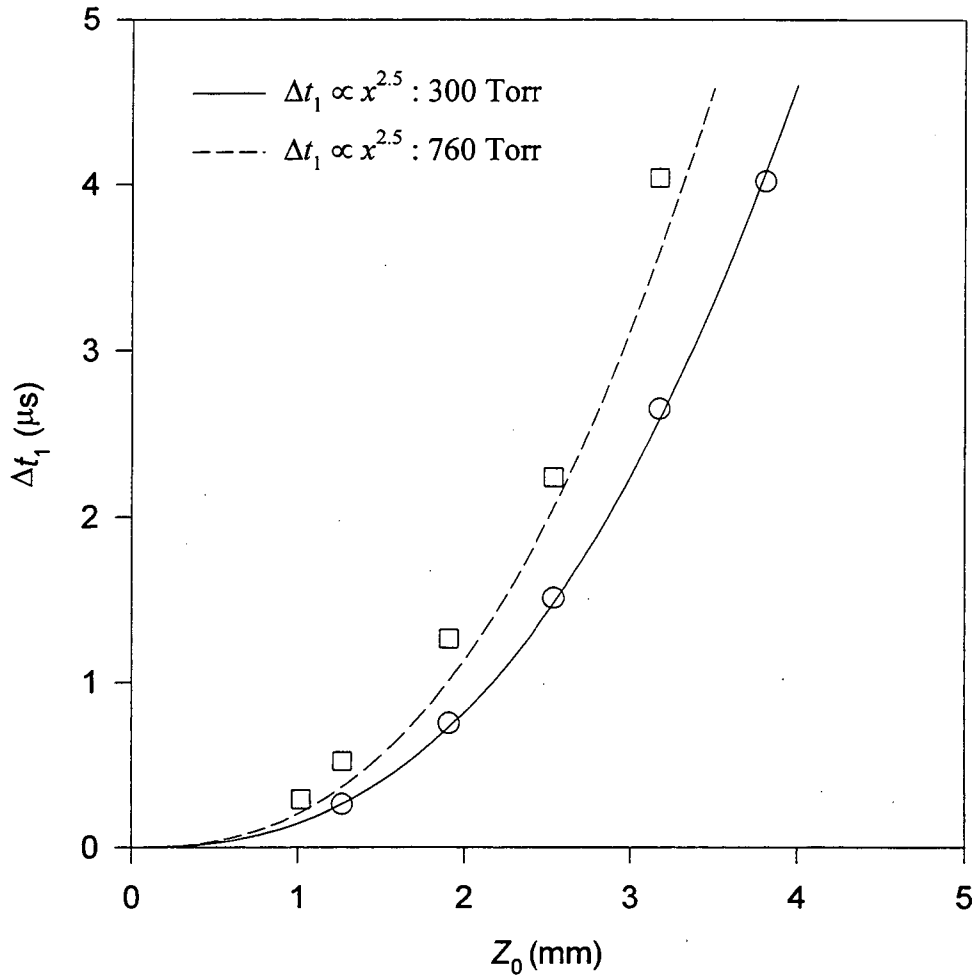

Fig. 4.17 Time-of-propagation of the shock wave for different ambient pressures, 300 and 760 Torr as the laser spot size is kept to be small, 0.5 mm. (circle: 300 Torr, square: 760 Torr)

dividing the propagation distance by the elapsed time. The local velocity was obtained from the derivative of the polynomial curve closely fit the time-of-propagation data.

For large values of Z_0, the time-of-propagation increases linearly with distance and thus for this region the shock velocity is constant as obtained from the slope of the time-of-propagation data. An example is presented in Fig. 4.18 which is for laser heating in air with E_p=5.8 mJ and d_s=0.8 and 2.1 mm; the corresponding laser power density is 6.1×10^7 and 8.1×10^6 W/cm^2 for d_s=0.8 and 2.1 mm, respectively. The time-of-propagation of the shock for both cases show almost linear variations for Z_0>3mm. The velocity of the shock estimated from the slope of the time-of-propagation data in this region is found to be about 387 and 384 m/s for d_s=2.1 and 0.8 mm, respectively. Despite the large difference of laser power density (corresponding to the difference spot sizes), the shock velocity in this region is almost the same. Time-of-propagation data over a large range of laser power density, approximately between 8×10^6-1.2×10^9 W/cm^2, showed that the local shock velocity in this linear region is almost independent of the laser power density. Instead the shock velocity in this region is dependent upon the propagation distance and decreases slowly with the propagation distance. For example, for the data over the range of Z_0=3-5 or 6 mm, the slope of the time-of-propagation data for the above range of laser power densities produces a shock velocity about 380-400 m/s while the data over the range of Z_0=5 or 6-10 mm produce velocities of about 360 m/s. From these results it is postulated that after the propagation over a certain distance all the blast waves originally produced at different conditions may gradually result in similar weak blast waves. If this hypothesis is true, the weak blast wave occurring at large

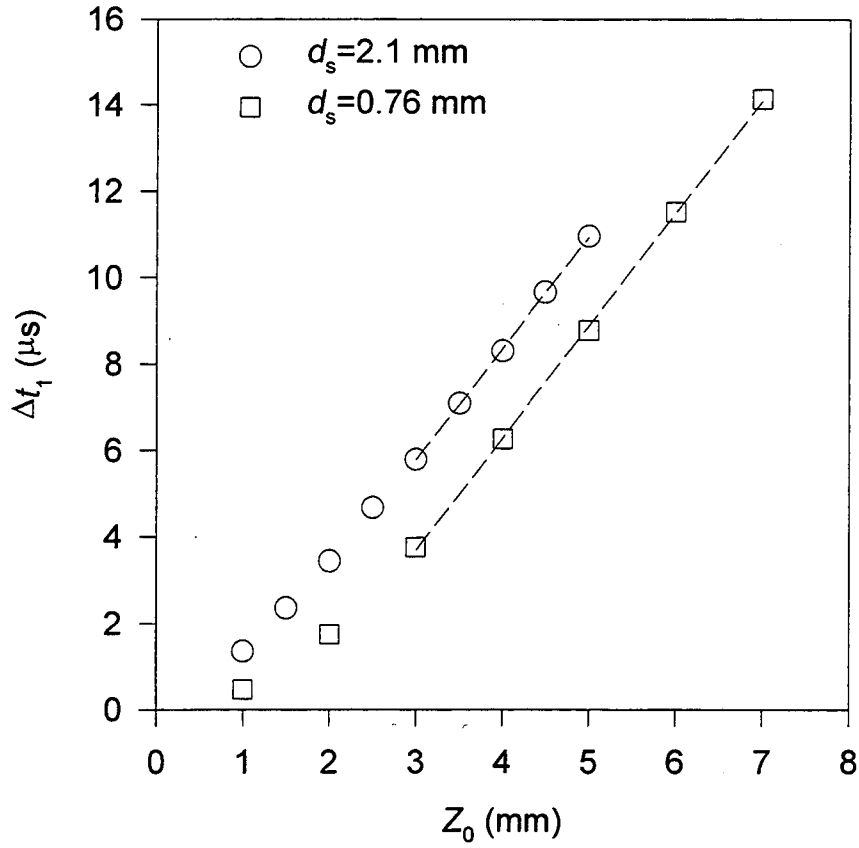

Fig. 4.18 Time-of-propagation of the shock wave over large propagation distances. Dashed lines represent linear curve fitting of the data for large values of Z_0. (circle: d_s=2.1 mm, square: d_s=0.8 mm)

distances from the center of explosion may not contain much information about the original explosion. In this far-field region, the difference in time-of-propagation is basically a delayed effect of the velocity difference near the target surface. For excimer laser heating of polished aluminum under the condition studied here this far-field region is approximately Z_0>3~4 mm from the target surface. Obviously, the boundary of this far-field region above which differences in local shock velocity become small may change with material and other experimental conditions. However, since $c_s \propto r_s^{-1.5}$ for a spherical blast wave, most of the laser generated blast wave may develop a weak blast wave after propagating relatively small distances.

Repetitive heating on the same surface location

The time-of-propagation of the laser induced shock wave during repetitive heating at the same spot on the target surface is found to increase for the first few pulses and become almost uniform for successive pulses. An example for repetitive heating in air is shown in Fig. 4.19 where Z_0 and E_p are 2 mm and 6 mJ, respectively,. Since it was observed from Fig. 4.11 that the time-of-propagation increases for decreasing laser pulse energy, the increase of the time-of-propagation for the first few pulses may be interpreted as resulting from the decrease of the laser energy coupling efficiency during the repetitive heating. It may be that there exists a surface layer that absorbs more laser energy and after a few pulses the surface layer is completely removed and the subsequently exposed bulk aluminum absorbs less laser energy. Oxidation or contamination of the target surface are other possible mechanisms to describe the increased energy coupling for the first few

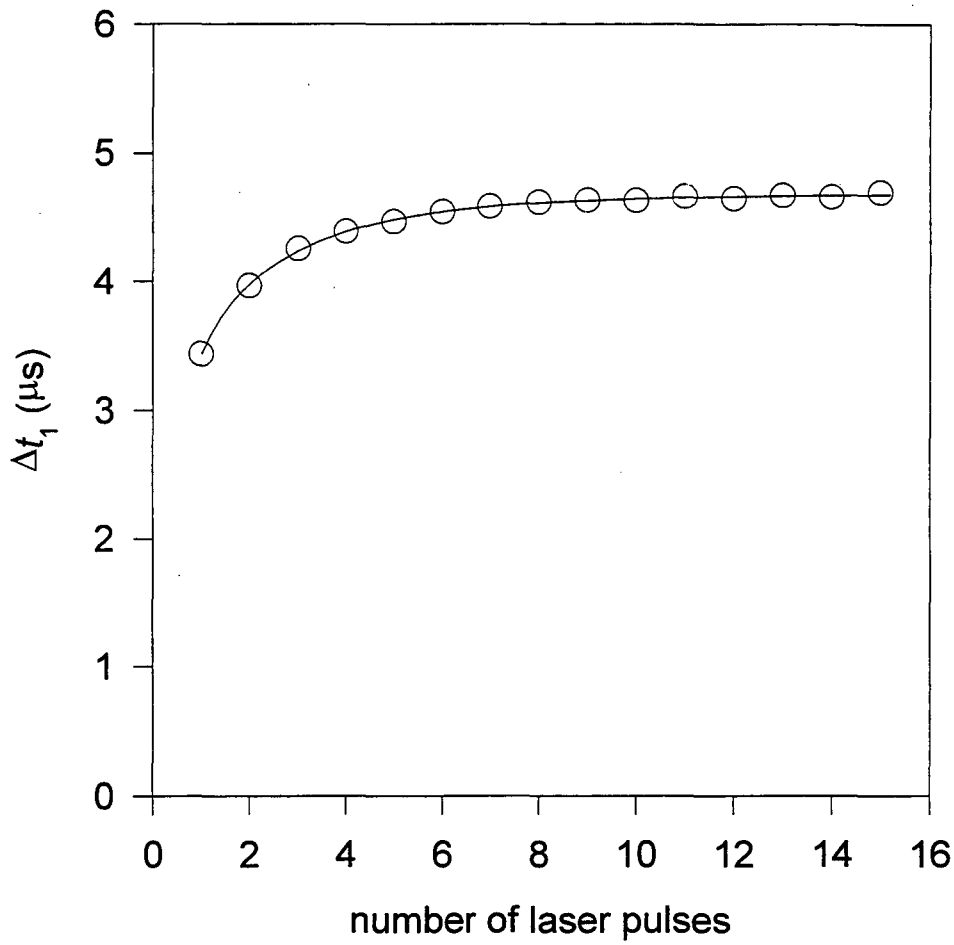

Fig. 4.19 Time-of-propagation of the shock wave with respect to the repetitive heating at the same spot

pulses.

4.4.1.3 Estimation of the blast wave energy

The time-of-propagation data of a laser induced blast wave are useful in predicting the energy coupled into the explosion by comparisons with theoretical models. The similarity solution is most often used for the theoretical model. Eq. (4.2) can be rewritten for the blast wave energy as

$$E_0 = \frac{\rho_\infty}{\alpha} \frac{r_s^{(n+2)}}{t^2} \tag{4.12}$$

Since Eq. (4.12) is valid for an ideal strong blast wave, the time-of-propagation data in Fig 4.17, which follow this relationship most closely, are used to estimate the blast wave energy. The laser pulse energy E_p for these data is about 7 mJ. The blast wave induced by laser heating of a solid target is different from an explosion generated in a gas. Hall [39] showed that the effective blast wave energy for laser heating of solids can be obtained by considering the effect of the target on the geometrical shape of the blast wave. For a perfect target surface, which exerts no drag force on the gas flow, the shape of the laser induced blast wave is expected to be hemispherical and the effective blast wave energy in this case is one half of the value predicted by Eq. (4.12) which is for a spherical blast wave. A perfect target surface is assumed in the present study. Also the air is assumed to be a polytropic gas satisfying the relation p/ρ^γ=constant. The constant α is 1.175 for a spherical blast wave [42]. The time-of-propagation data and the corresponding blast wave energy predicted using Eq. (4.12) are shown in Fig. 4.20, where E_0^* is $E_0/2$. First we

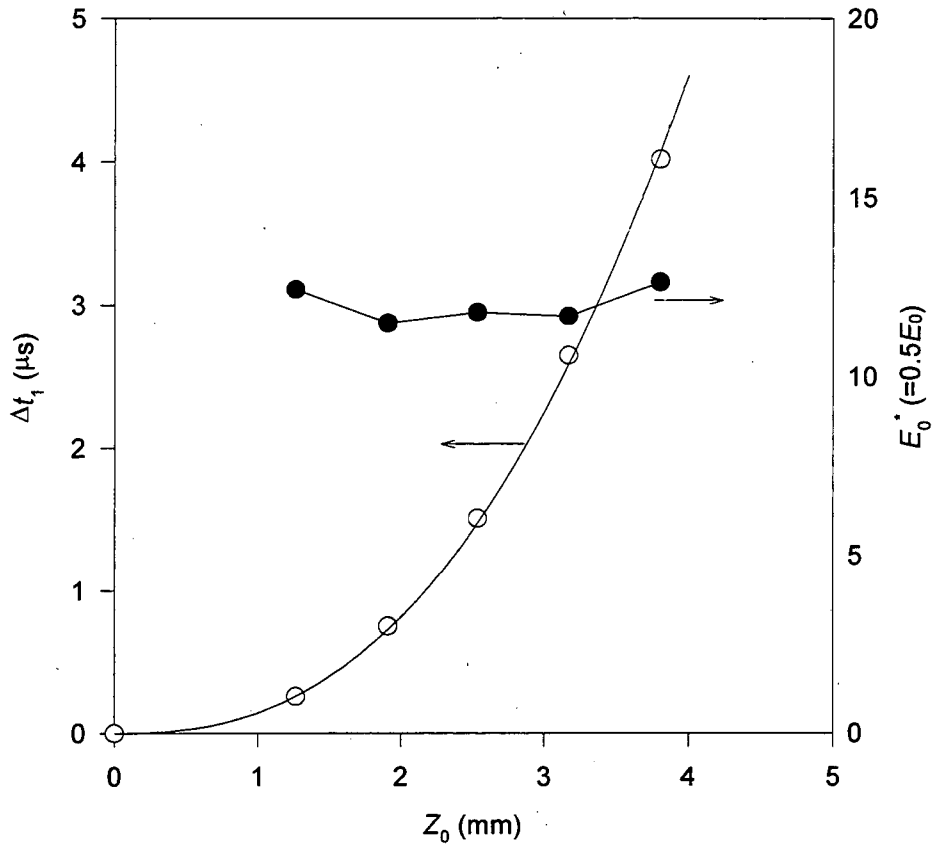

Fig. 4. 20 The energy contained in the laser induced blast wave estimated using the ideal strong blast wave solution. E_0^*=0.5E_0 (E_0 is given by Eq. (4.12)). Data for p_∞= 300 Torr in Fig. 4.17 is used for the calculation.

observe that the energy predicted by Eq. (4.12) is almost constant for the measured data in Fig. 4.20 in that the theoretically predicted propagation matches closely the measured data. The average value of the predicted blast wave energy E_0^* is about 12 mJ and agrees within 5% deviation from the average value (of predicted E_0^*) based on the propagation results (see Fig. 4.20). This result implies that any data which lie within the range where the time-of-propagation data comply with the theoretical propagation can be used for the prediction of the blast wave energy. Therefore the data at short distance from the target surface are not required for a better blast wave energy prediction. The measurement of time-of-propagation data for very small Z_0 is difficult and there is usually more variation between measurements.

Note that the total experimental laser pulse energy is only 7 mJ, while the blast wave energy in Fig. 4.20 predicted using Eq. (4.12) is 12 mJ. If the large reflectivity of aluminum surface is considered, the degree of overestimation in the predicted blast wave energy becomes even greater. The predicted blast wave energy indicates that the shock wave propagates as if the blast wave was generated with a much greater explosion energy. In other words, the result implies that the shock wave propagates much faster than the theoretically expected speed. This result leads to the possibility that there exists a fundamental difference between the laser induced blast wave and ideal blast wave theory. Since the time-of-propagation of the shock wave is the result used for the prediction of the blast wave energy, the difference may be found in the shock wave velocity. To be able to produce such a high shock wave velocity that results in the overestimation of the blast wave energy in Fig. 4.20, there may have been an acceleration of the shock wave.

However, the similarity solution for ideal strong blast wave in Eq. (4.3) only predicts a deceleration of the shock wave in accordance with the relation $c_s \propto r_s^{-1.5}$ or $c_s \propto t^{-0.4}$. Acceleration of the shock wave, if exists, can not be obtained from this theory. The possibility of unsteady adiabatic expansion of the vapor was observed from the numerical simulation of the one dimensional vapor flow, see Fig. 3.15(b). Since $E_0 \propto c_s^2$ from Eq. (4.3), the acceleration of the shock wave may result in a quadratic increase of the predicted blast wave energy.

Ideal blast wave theory assumes that the mass release from the target is negligible. However, it is known that energetic vapor is always present during laser ablation of solids at high power density. The experimental value of laser power density for the measurements shown in Fig. 4.20 is about 1.7×10^8 W/cm^2; it may be possible at this power density to produce excited atoms or a weakly ionized gas. It is known that the threshold laser power density for plasma shielding is about 3×10^8 W/cm^2 for many materials [3]. In the present experiments, white luminescence was observed during the excimer laser heating of the aluminum target. Even though the luminescence does not necessarily mean that there exists plasma shielding, it is likely that excited gas particles are generated. The existence of (ionized) gas particles with higher velocities than expected in laser generated plumes was observed by different researchers [5,6,7]. If excited gas particles exist near the target surface and they return to the ground state or condense after the laser pulse is completed, they will release energy which would provide additional kinetic energy to the vapor flow. If direct absorption of the incident laser

energy by the vapor is involved, this may also result in an increase of the kinetic energy of the flow.

It is found that using the solution of an ideal blast wave to match the shock wave propagation data results in an overestimation of the energy transferred into a laser induced blast wave. The reason for the overestimation may be an acceleration of the flow in the laser induced blast wave. Unsteady adiabatic expansion of the vapor or the existence and supply of additional kinetic energy to the flow from excited gas particles may be responsible for the acceleration.

4.4.2 Deflection of the probe beam for the period $t > 10$ μs

The shock wave generated during pulsed laser heating of solids propagates with a maximum speed on the order of 1000 m/s near the target surface and hence is always observed in the deflection time-response profiles within a few microseconds. However, when the deflection of the probe beam is recorded over a long interval of time, another deflection signal appears that correspond to a propagation only of an average speed of tens of meters per second. An example of this signal is shown in Fig. 4.21 for which the normal offset of the probe beam is 1.9 mm. The deflection profiles in Fig. 4.21(a), (b), and (c), are obtained at the same experimental conditions and the only difference among these deflection signals is the recording time on the oscilloscope. This deflection of the probe beam at later time basically consists of a large positive deflection followed by a large negative deflection. It is clear that this deflection at later time is completely separate from the shock wave which is denoted by 'S' in Fig. 4.21. This deflection at later time is

reproducible and consistent for small values of Z_0 (<2.0 mm) while those for larger values of Z_0 show differences between measurements. This type of deflection at later time was also observed by other researchers [21,22,26,38]. Matthias et al. [22] described this later deflection from excimer laser heating of an aluminum target as being due to the plasma plume. Koren [26] explained this type of deflection from excimer laser heating of Kapton films as being due to a cooling wave. Ventzek et al. [38] observed this type of deflection signal from excimer laser heating of a polyethyleneterephthalate (PET) target in atmospheric pressure gases. Ventzek et al. also took photographs of the plume and described this deflection as resulting from the formation of a local volume with smaller density than the surrounding.

It can be proved that the deflection response at later time shown in Fig 4.21 is not due to a temperature gradient. For example, when Z_0=1.9 mm the signal returns to its original conditions in about 310 μs after the excimer laser pulse. The thermal diffusion length during this period in atmospheric air at room temperature is only about 0.12 mm, which is much smaller than the normal offset of 1.9 mm of the probe beam. Also photothermal deflection should not have a negative deflection for single pulse laser heating because heat diffusion occurs only from the target to the surrounding air and for this temperature field the density only increases with distance from the surface. Note that the deflection of the probe beam occurs toward the higher density field. Since the deflection at later time is composed of a positive and then a negative deflection, it is expected that the density field first decreases and then increases until it becomes equal to the ambient density. The point where the density field changes from a decrease to an

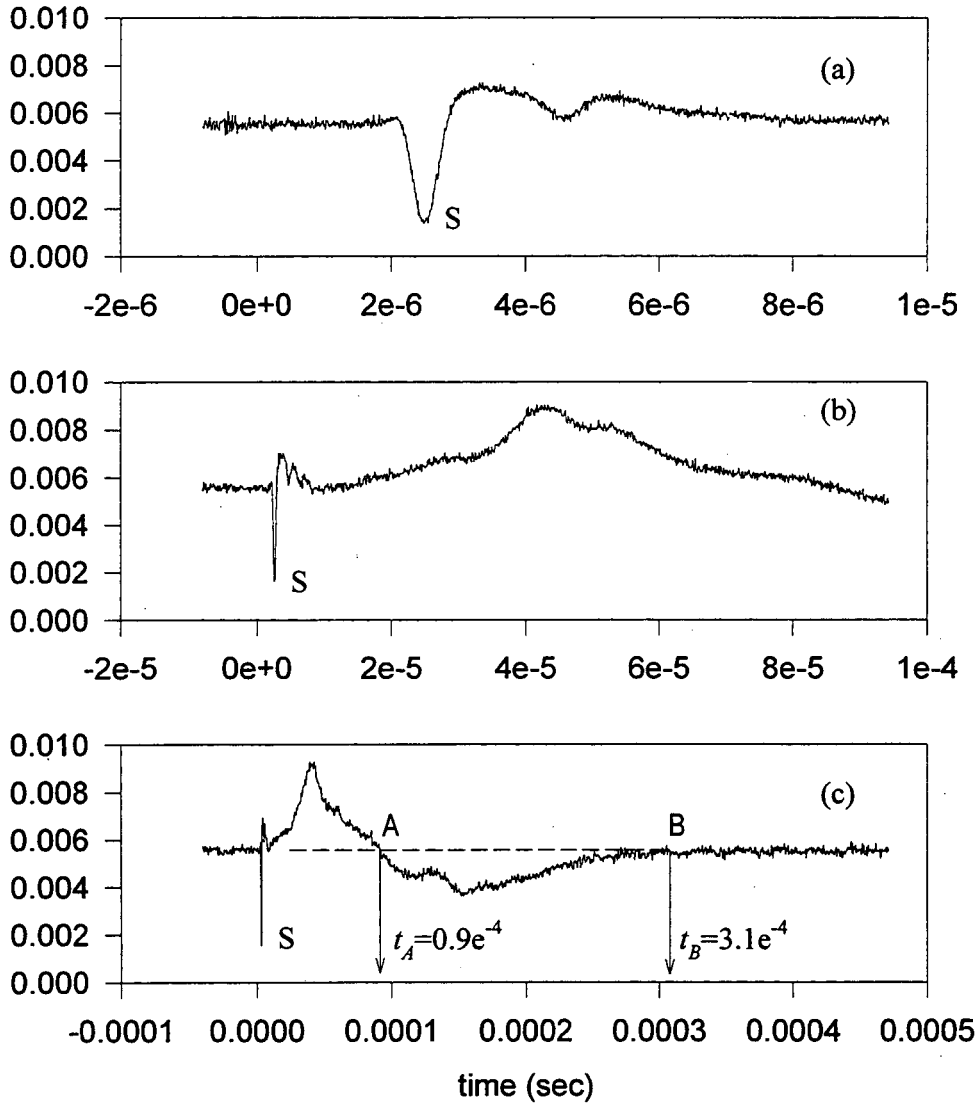

Fig. 4.21 Deflection of the probe beam recorded over different intervals of time. All three signals are produced at the same experimental conditions. (E_p=7 mJ, Z_0=1.9 mm)

increase corresponds to the time when the positive deflection returns to zero, point A in Fig. 4.21(c). Another interesting aspect of the deflection at later time signal is that the positive deflection takes place for a much shorter period than the negative deflection. Again from Fig. 4.21(c), the duration of the positive deflection is about 90 μs, $0<t<t_A$, while that for the negative deflection is about 220 μs, $t_A<t<t_B$. In other words, the density field has a narrow front with decreasing density, which produces the positive deflection, and a tail almost twice wider than the front with increasing density, which produces the negative part. From these results the density field that produces the deflection at later time can be qualitatively constructed as shown in Fig. 4.22 in which the locations S, A, and B correspond to those points in the deflection signal.

It is known that for laser heating of solids in a gaseous ambient the plume of target material in vapor state remains attached to the target surface even after the shock wave has traveled a large distance [11,13,14]. Since the gas in the plume near the target is expected to be at much higher temperatures than the surrounding gas, the corresponding density of the plume could be lower than the surrounding gas. Also note that aluminum vapor has a smaller molecular weight than the surrounding air which contributes to a smaller density. The aluminum plume which was attached to the target for a certain period of time after the heating from the excimer laser pulse will eventually detach and move away from the target. Since the target evaporation persists only almost for the duration of the excimer laser pulse, the space between the tail of the plume and the target surface after the plume detaches should be filled with the surrounding air (and not with aluminum vapor). As the plume travels away from the target, the plume will expand in

volume and mix with the surrounding air. Since the mixing occurs first at the plume boundary, the boundary will have a larger density than near the center. This type of gaseous aluminum plume surrounded by air may produce the density field consistent with the observed later deflection profile and is schematically represented in Fig. 4.23.

The average vertical velocity of the density field that produces the deflection at later time can be obtained by dividing the probe beam normal offset, Z_0, by the elapsed time until the positive deflection returns to zero, t_A in Fig. 4.21(c). The average vertical velocity of the density field is found to be about 35-40 m/s for Z_0<1.2 mm and about 20 m/s for Z_0=1.9 mm. The average vertical velocity of the plume obtained by Ventzek et al. [38] was about 18 m/s for excimer laser heating of PET target. The vertical velocity of the density field of the current study is in reasonably close range with the vertical plume velocity observed by Ventzek et al.

If the surrounding gas is at almost the same density as the gaseous material plume, mixing of the plume with the surrounding gas would not develop a large density gradient across the plume as observed in the deflection at later time. For this condition the deflection amplitude must decrease due to a smaller density gradient. The deflection signal for different ambient pressures is shown in Fig. 4.24. The amplitude of the deflection signal decreases at lower pressures and almost completely disappears at 100 Torr, which is consistent with the hypothesis that the deflection at later time is due to the propagating plume with smaller density at its center. Experiments at various ambient pressures showed that the deflection at later time disappears at ambient pressures of about

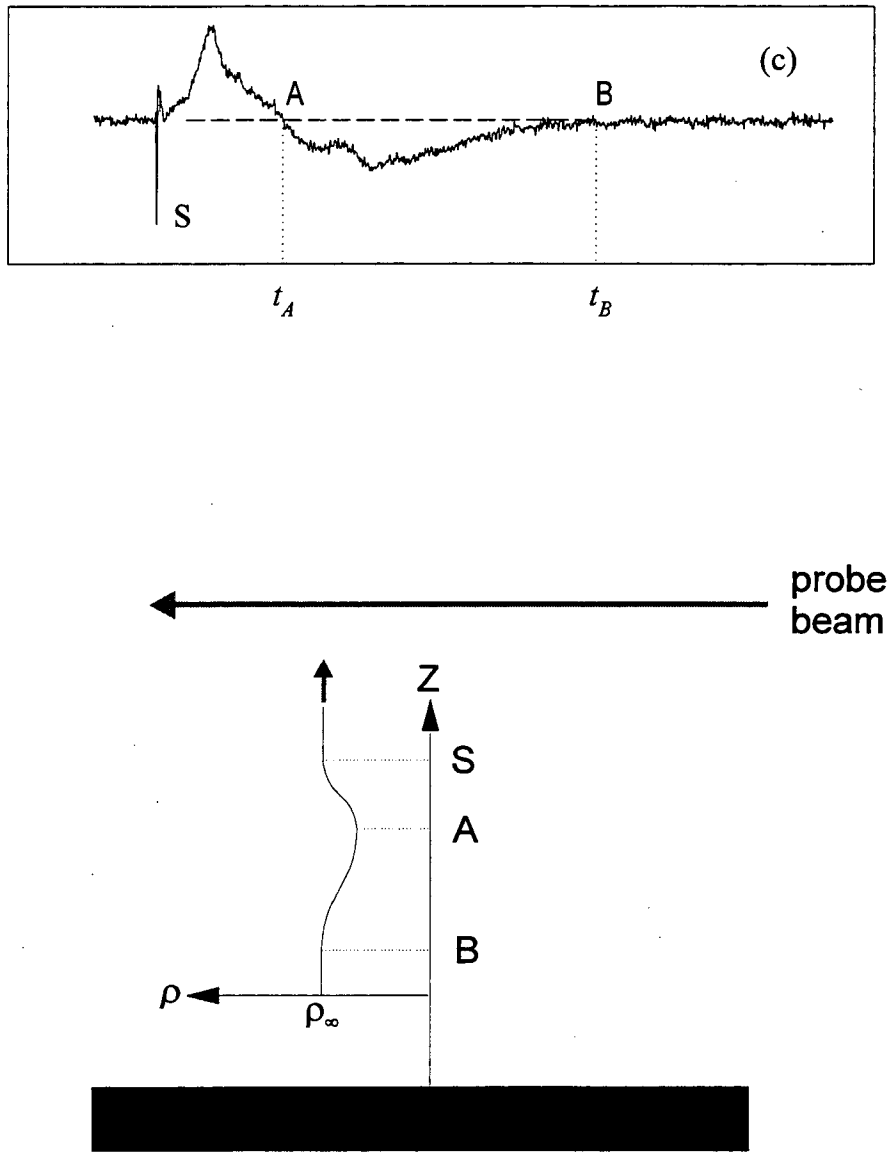

Fig. 4.22 Schematic representation of the density field for a plane wave that produces the deflection profile shown in the figure (The locations S, A, and B in both figure correspond to each other.)

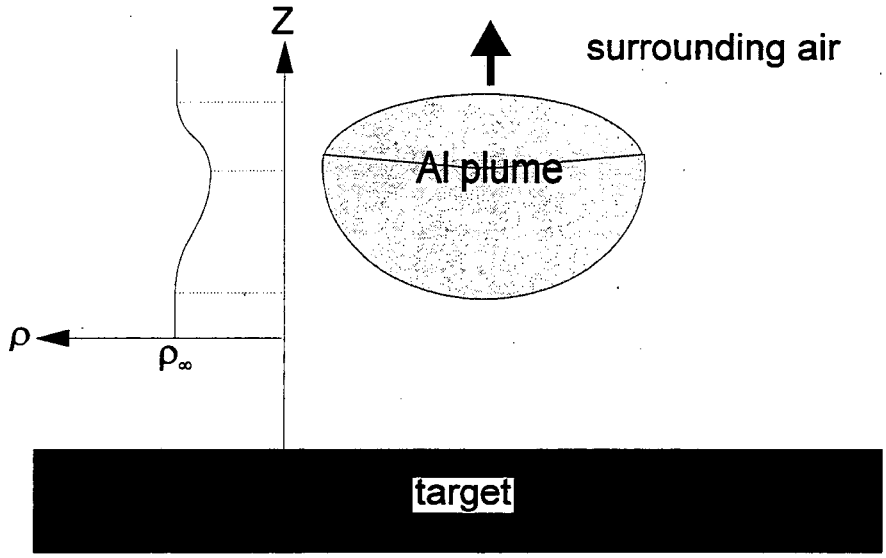

Fig. 4.23 Schematic diagram for the density cavity formed by the aluminum plume in the surrounding air.

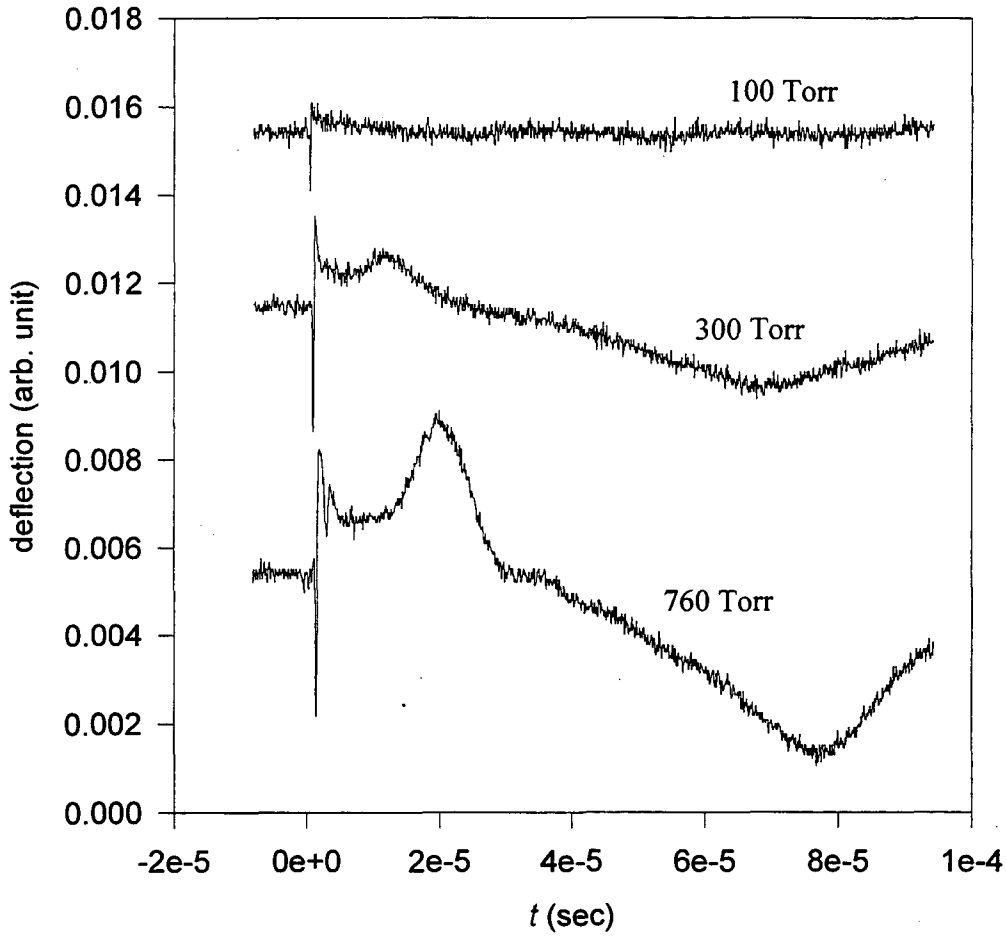

Fig. 4.24 Deflection time-response profiles at later time for different ambient pressures (Z_0=1.27 mm).

100-200 Torr. Since the deflection at later time disappears at ambient pressures between 100-200 Torr, the density of the plume should be similar to the density of air at this pressure, which is about 0.28-0.45 times smaller than the air density at atmospheric pressure.

4.4.3 Target surface morphology

Scanning electron microscope (SEM) photographs of aluminum targets irradiated by the excimer laser beam are presented in Figs. 4.25 and 4.26. The sample surface for Fig. 4.25(a)-(c) was mirror-polished to obtain better observation of the laser heated region while that for Fig. 4.26(a) and (b) was treated with sand paper (SiC #600). Since the reflectivity of the mirror-polished surface is much higher than the sanded surface, greater laser power density was required for the mirror-polished surface shown in Fig. 4.25 to produce the material deformation; the laser power densities for Fig. 4.25 and Fig. 4.26 is about 2.3×10^8 and 1.4×10^8 W/cm^2, respectively. The laser spot size is provided in the figure caption.

Fig. 4.25(a) shows the target surface after irradiation by a single laser pulse where melting of the target is easily observed. Wave like patterns are formed along the boundary of the irradiated region, which are clearer at the top and bottom edges in the figure. The outward radial flow of the melt, indicated by the arrow in Fig. 4.25(a), is also observed starting from the distance of approximately two thirds of the radius of the irradiated region to the boundary. The radial flow and accumulation of the melt at the edge of the irradiated region result in the formation of a rim around the boundary for

repetitive heating. The radial flow of the melt and the wave pattern are more distinct in Fig. 4.25(b) which is observed after 5 consecutive laser pulses at a repetition rate of 2 Hz and the formation of a rim in Fig. 4.25(c) which is after 100 pulses at the same repetition rate. The radial flow of the melt is evidence of a strong pressure difference between the middle of the irradiated area and the outer region. The radial expansion of the high pressure vapor may exert a strong drag force on the melt surface and generate the outward flow of the melt. The melt flow is opposed by the solid and accumulates at the edge and become unstable to further accumulation to form the observed waves.

The irradiated region in Fig. 4.25(a) shows almost evenly distributed roughening of the surface. The middle of the irradiated area exhibits not only pressure driven flow patterns but also many small bulges on the surface. These roughness or surface bulges become smaller with an increasing number of pulses and completely disappear after 100 pulses, see Fig. 4.25(c). After 100 pulses, the laser spot is amazingly clean and shows a smooth middle area. The roughening of the surface after a single pulse may be considered to be a surface mechanism. After the surface layer is completely removed and bulk aluminum is exposed to the incident laser radiation, a uniform absorption of the laser energy by the target may be achieved to produce the observed smooth surface. Oxidation, contamination, or mechanical imperfections of the sample surface may be the reason for the surface morphology for a single pulse.

For a sand treated target, surface damage occurred at a lower laser power density. The roughness of the surface is believed to result in higher laser energy coupling efficiency due to the multiple reflections of the laser beam inside the spaces or gaps

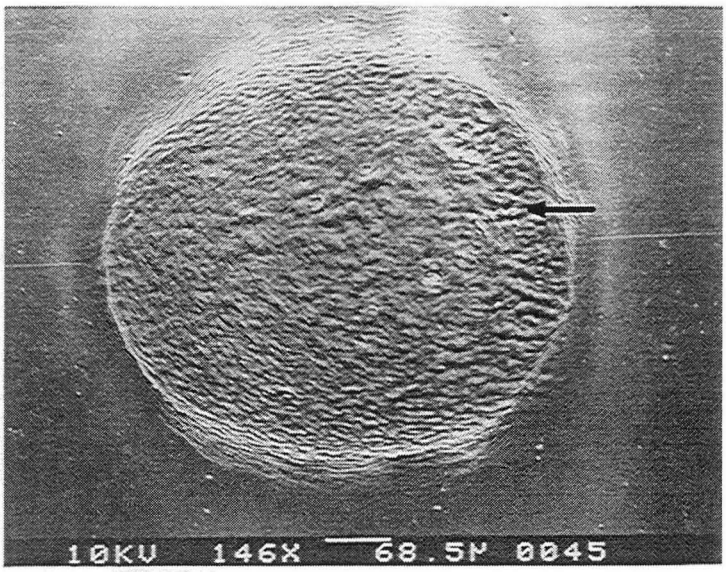

(a)

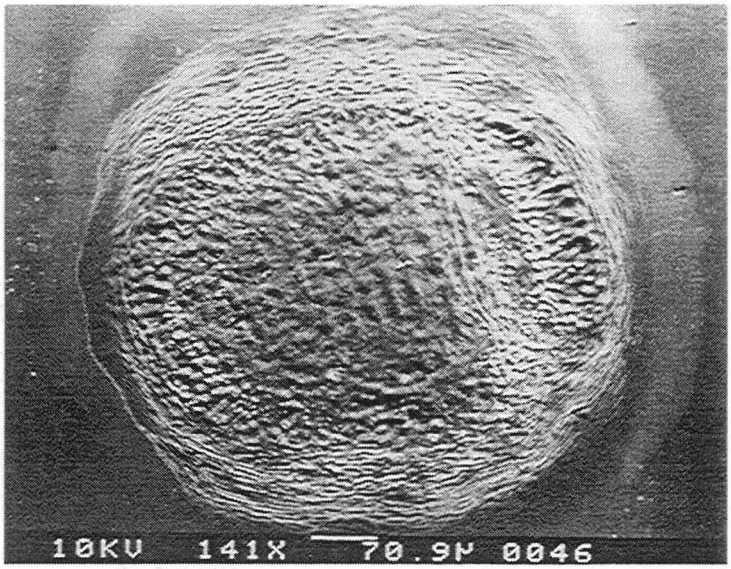

(b)

Fig. 4.25 Scanning electron microscopy photographs of a mirror polished aluminum target heated by the excimer laser; pulse duration=21 ns, d_s=~0.5 mm, (a) 1 pulse (E_p=9.9 mJ), and (b) 5 pulses (average E_p=9.5 mJ)

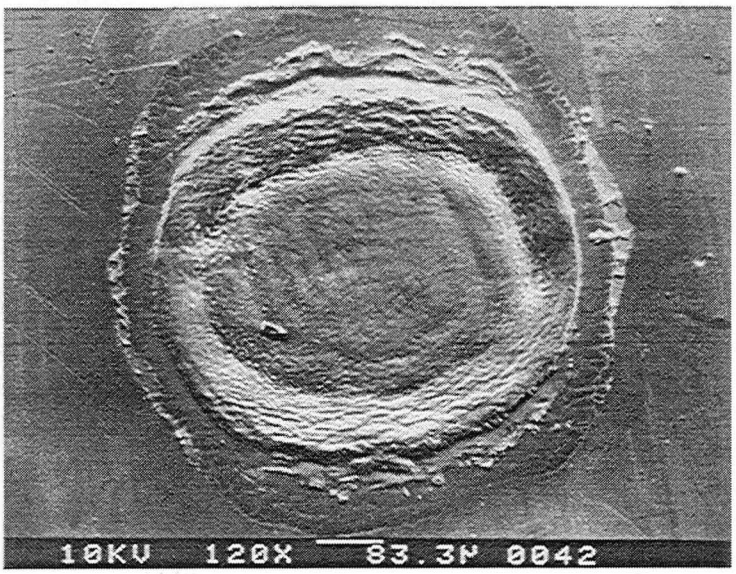

(c)

Fig. 4.25 Scanning electron microscopy photograph of a mirror polished aluminum target heated by the excimer laser; pulse duration=21 ns, d_s=~0.5 mm, (c) 100 pulses (average E_p=9.3 mJ)

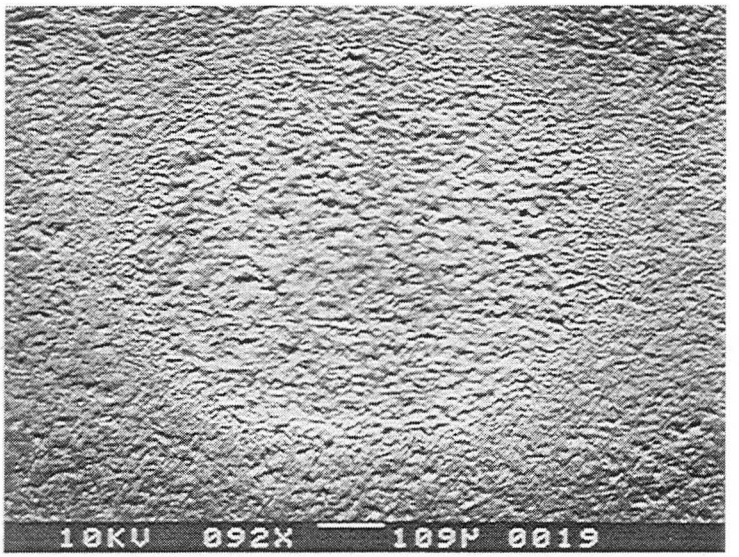

(a)

(b)

Fig. 4.26 Scanning electron microscopy photographs of a polished (with SiC paper #600) aluminum target heated by the excimer laser; pulse duration=21 ns, d_s=~0.7 mm, average E_p=11.0 mJ, (a) 20 pulses and (b) 100 pulses

produced by the surface roughnesses. The damage threshold of the laser power density is roughly about 1.0×10^8 W/cm^2 or smaller. Figs. 4.26(a) and (b) show the sanded surface irradiated by 20 and 100 excimer laser pulses, respectively. The laser power density is about 1.4×10^8 W/cm^2, which is intentionally kept higher than the surface damage threshold for better photographic images. Surface melting and the formation of the rim around the boundary are also observed at this power level.

4.5 Conclusions

The dynamics of the gasdynamic flow generated by excimer laser heating of aluminum targets was studied. The probe beam deflection technique was employed to determine the time-of-propagation of the shock wave. The time-of-propagation of the laser induced plume was investigated with respect to laser pulse energy, ambient pressure, and the propagation distance of the shock. Experimental conditions at which the measured time-of-propagation of the shock wave is consistent with blast wave theory were determined. The propagation of the gaseous target material plume is observed from the deflection at later time of the probe beam.

The results are summarized below;

(1) The time when the shock wave arrives at the probe beam height is identified from the measured deflection profile. Thus it is possible to define accurate time-of-propagation data for the laser induced shock wave.

(2) The propagation of the laser induced shock wave near the target surface is planar rather than spherical for a relatively large laser spot size. For an aluminum target, the propagation of the flow for Z_0<1 mm is almost planar when the laser spot size is about 1.5 mm.

(3) The parameters that determine the time-of-propagation of a laser induced shock to agree with the prediction by ideal blast wave theory are the small ambient pressure and the small laser spot size. The assumption that the laser induced blast wave at short distances from the target is similar to the ideal blast wave is found invalid.

(4) The similarity solution for an ideal blast wave overpredicts the laser energy that is coupled to the laser induced blast wave. The overestimation is considered to be due to unsteady adiabatic expansion of the laser induced gasdynamic flow and/or the direct absorption of laser energy by the vapor that provide additional kinetic energy to the flow.

(5) The propagation of the gaseous material plume is observed from the deflection at later time of the probe beam. The gaseous material plume produces the observed large positive and the following negative deflections. The propagation velocity of the gaseous aluminum plume decreases from about 40 m/s near the target to about 20 m/s at a distance of 2 mm from the target. The density of the gaseous material plume is expected to be about 0.28-0.45 times smaller than the air density at atmospheric pressure.

(6) Scanning electron microscopy examination of the target surface showed the radial flow of the melt and the formation of a rim, which is believed due to the strong

pressure gradient between the irradiated region and the surrounding area. The threshold laser power density for damage to a sanded surface is approximately 1.0×10^8 W/cm^2 or smaller which is less than that for a mirror-polished surface.

References

[1] M. von Allmen, *Laser-Beam Interactions with Materials*, Springer, 1987

[2] X. L. Mao, W. T. Chan, M. Caetano, M. A. Shannon, and R. E. Russo, "Preferential vaporization and plasma shielding during nanosecond laser ablation", Applied Surface Science, 96-98, 1996, pp. 126-130

[3] Xianglei Mao and Richard E. Russo, "Observation of plasma shielding by measuring transmitted and reflected laser pulse temporal profiles", Appl. Phys. A 64, 1997, pp. 1-6

[4] A. Fernandez, X. L. Mao, W. T. Chan, M. A. Shannon, and R. E. Russo, "Correlation of spectral emission intensity in the inductively coupled plasma and the laser-induced plasma during laser ablation of solid samples", Anal. Chem, Vol. 67, No. 14, 1995, pp. 2444-2450

[5] H. Wang, A. P. Salzberg, and B. R. Weiner, "Laser ablation of aluminum at 193,248,and 351 nm", Appl. Phys. Lett., 59 (8), 1991, pp. 935-937

[6] R. W. Dreyfus, R. Kelly, and R. E. Walkup, "Laser-induced fluorescence studies of excimer laser ablation of Al_2O_3", Appl. Phys. Lett., 49(21), 1986, pp. 1478-1480

[7] I. Borthwick, C. T. J. Scott, K. W. D. Ledingham, and R. Singhal, "Velocity distributions of aluminum atoms ablated from aluminum metal" in *Laser ablation;*

mechanisms and applications II, edited by J. C. Miller and D. B. Geohegan, AIP Press, 1993, pp. 414-420

[8] D. B. Geohegan and A. A. Puretzky, "Dynamics of laser ablation plume penetration through low pressure background gases", Appl. Phys. Lett., 67(2), 1995, pp. 197-199

[9] T. Zyung, H. Kim, J. C. Postlewaite, and D. D. Dlott, "Ultrafast imaging of 0.532μm laser ablation og polymers: Time evolution of surface damage and blast wave generation", J. Appl. Phys. 65 (12) 1989, pp. 4548-4563

[10] A. Mele, A. Giardini Guidoni, R. Kelly, A. Miotello, S. Orlando, R. Teghil, and C. Flamin, "Angular distribution and expansion of laser ablation plumes measured by fast intensified charge coupled device photographs", Nuclear Instruments and Methods in Physics Research B 116, 1996, pp. 257-261

[11] A. Gupta, B. B. Braren, K. G. Casey, B. W. Hussey, and R. Kelly, "Direct imaging of the fragmants produced during excimer laser ablation of $YBa_2Cu_3O_{7-\delta}$", Appl. Phys. Lett., 59 (11), 1991, pp. 1302-1304

[12] P. E. Dyer, P. H. Key, D. Sands, H. V. Snelling, and F. X. Wagner, "Blast wave studies of excimer laser ablation of ZnS", Applied Surface Science 86, 1995, pp. 18-23

[13] P. L. G. Ventzek, R. M. Gilgenbach, C.H. Ching, and R. A. Lindley, "Schlieren and dye laser resonance absorption photographic investigations of KrF excimer laser-ablated atoms and molecules from polyimide, polyethyleneterephthalate, and aluminum", J. Appl. Phys. 72 (5) 1992, pp. 1696-1706

[14] R. M. Gilgenbach and P. L. G. Ventzek, "Dynamics of excimer laser ablated aluminum neutral atom plume measured by dye laser resonance absorption photography",

Appl. Phys. Lett., 58 (15), 1991, pp.1597-1599

[15] G. Callies, P. Berger, and H. Hugel, "Time-resolved observation of gas-dynamic discontinuities arising during excimer laser ablation and their interpretation", J. Phys. D: Appl. Phys., 28, 1995, pp. 794-806

[16] J. A. Sell, D. M. Heffelfinger, P. L. G. Ventzek, and R. M. Gilgenbach, "Photoacoustic and photothermal beam deflection as a probe of laser ablation of materials" J. Appl. Phys. 69 (3) 1991, pp. 1330-1336

[17] J. Diaci and J. Možina, "A study of blast waveforms detected simultaneously by a microphone and a laser probe during laser ablation", Appl. Phys. A 55, 1992, pp. 352-358

[18] G. E. Jamieson and G. C. Wetsel, Jr., "Optical-beam-deflection probing of blast waves near solid surfaces", 1985 IEEE Ultrasonics symposium proceedings, 1985, pp. 451-455

[19] E. Heidecker, J. H. Schafer, J. Uhlenbusch, and W. Viol, "Time-resolved study of a laser-induced plasma by means of a beam-deflection technique", J. Appl. Phys. 64 (5), 1988, pp. 2291-2297

[20] H. Guo, Q. Lou, S. C. Chen, N. H. Cheung, Z. Y. Wang, and P. K. Lin, "Beam-deflection study of shock wave formation and propagation in gas ambient during uv laser ablation of solid material", Optics Communications 98, 1993, pp. 220-224

[21] R. Pini, R. Salimbeni, M. Vannini, and G. Toci, "Probe -beam deflection diagnostics of shock waves generated during laser drilling", Appl. Phys. B 61, 1995, pp. 505-510

[22] E. Matthias, J. Siegel, S. Petzoldt, M. Reichling, H. Skurk, O. Kading, and E. Neske,

"In-situ investigation of laser ablation of thin films", Thin solid films 254, 1995, pp. 139-146

[23] D. B. Geohegan, "Imaging and blasckbody emission spectra of particulates generated in the KrF-laser ablation of BN and $YBa_2Cu_3O_{7-x}$", Appl. Phys. Lett., 62 (13), 1993, pp. 1463-1465

[24] R. Kelly, A. Miotello, B. Braren, and C. E. Otis, "On the debris phenomenon with laser-sputtered polymers", Appl. Phys. Lett 60 (24), 1992, pp. 2980-2982

[25] J. Diaci and J. Mozina, "A study of energy conversion during Nd:YAG laser ablation of metal surfaces in air by means of a laser beam deflection probe", Journal De Physique IV, Vol. 4, 1994, pp. 737-740

[26] G. Koren, "Observation of shock waves and cooling waves in the laser ablation of Kapton films in air", Appl. Phys. Lett. 51 (8), 1987, pp. 569-571

[27] H. Guo and Q. Lou, "The study of the processes of laser-induced vaporization of copper surface by time-resolved laser beam deflection technique", Optics communications, Vol. 77, No. 5-6, 1990, pp. 381-384

[28] A. M. Azzeer, A. S. Al-Dwayyan, M. S. Al-Salhi, A. M. Kamal, and M. A. Harith, "Optical probing of laser-induced shock waves in air", Appl. Phys. B, 63, 1996, pp. 307-310

[29] J. A. Sell, "Determination of position or speed of an object using pulsed laser photoacoustic beam deflection", Rev. Sci. Instrum. 63 (7), 1992, pp. 3583-3585

[30] S. H. Jeong, R. Greif, and R. E. Russo, "Laser heating of a cavity versus a plane surface for metal targets utilizing photothermal deflection measurements", J. Appl. Phys. 80 (4), 1996, pp. 1996-2002

[31] M. A. Shannon, A. A. Rostami and R. E. Russo, "Photothermal deflection measurements for monitoring heat transfer during modulated laser heating of solids", J. Appl. Phys. 71(1), 1992, pp. 53-63

[32] M. A. Shannon, B. Rubinsky, and R. E. Russo, "Detecting laser-induced phase chage at the surface of solids via latent heat of melting with a photothermal deflection technique", J. Appl. Phys. 75 (3), 1994, pp. 1473-1485

[33] S. Petzoldt, A. P. Elg, M. Reichling, J. Reif, and E. Matthias, "Surface laser damage thresholds determined by photoacoustic deflection", Appl. Phys. Lett. 53 (21), 1988, pp. 2005-2007

[34] J. A. Sell, D. M. Heffelfinger, P. L. G. Ventzek, R. M. Gilgenbach, "Laser beam deflection as a probe of laser ablation of materials", Appl. Phys. Lett. 55 (23), 1989, pp. 2435-2437

[35] E. Welsch, K. Ettrich, M. Peters, W. Ziegler, and H. Blaschke, "Application of photothermal probe beam deflection technique for ablation and damage measurements by using short UV laser pulses", Journal De Physique IV, Vol. 4, 1994, pp. 749-752

[36] C. L. Enloe, R. M. Gilgenbach, and J. S. Meachum, "Fast, sensitive laser deflection system suitable for transient plasma analysis", Rev. Sci. Instrum. 58 (9), 1987, pp. 1597-1600

[37] S. J. Lee, K. Imen, and S. D. Allen, "Shaock wave analysis of laser assisted particle removal", J. Appl. Phys, 74 (12), 1993, pp. 7044-7047

[38] P. L.G. Ventzek, R. M. Gilgenbach, J. A. Sell, and D. M. Heffelfinger, "Schlieren measurements of the hydrodynamics of excimer laser ablation of polymers in atmospheric pressure gas", J. Appl. Phys. 68 (3), 1990, pp. 965-968

[39] R. B. Hall, "Laser production of blast waves in low pressure gases", J. Appl. Phys., Vol. 40, No. 4, 1969, pp. 1941-1945

[40] G. Taylor, "The formation of a blast wave by a very intense explosion, I. Theoretical discussion", Proc. Roy. Soc. A, Vol. 201, 1950, pp. 159-174

[41] D. L. Jones, "Intermediate strength blast waves", Phys. Fluids, Vol. 11, No. 8, 1968, pp. 1664-1667

[42] L. I. Sedov, *Similarity and dimensional methods in mechanics*, 10th ed., 1993, CRC press

[43] M. Born and E. Wolf, *Principles of Optics*, 6th ed., 1980, Pergamon press

[44] R. Kelly and B. Braren, "On the direct observation of the gasdynamics of laser-pulse sputtering of polymers", Appl. Phys. B 53, 1991, pp.160-169

Chapter 5

Conclusions and discussion

To better understand laser interactions with metal targets, high power CW and pulsed laser heating of metals was studied with experimental and numerical methods. Special interest was given to the laser energy coupling with the target. Simple heating, melting, and evaporation of metals under laser irradiation with a power density mostly below the plasma shielding threshold were investigated with rigorous theoretical modelings. Experimentally, the probe beam deflection technique was employed to measure the heating of the targets with no phase change and to measure the shock wave propagation during an explosive evaporation of the target by pulsed laser heating. The parameters that affect the laser energy coupling efficiency with a target and the characteristics of the laser induced gasdynamic flow were identified.

In Chapter 2, the effects of a cylindrical cavity in a metal surface on the energy coupling of a laser beam with a solid during a CW Nd-YAG laser heating were investigated utilizing the photothermal deflection measurement and a numerical calculation of the target temperature. The amplitude and time response of the measured and computed photothermal deflection responses were examined for copper, lead, and stainless steel, and for cavities with different aspect ratios. Reflection of the heating laser beam inside the cavity was found to increase the photothermal deflection amplitude significantly and the increase becomes larger when the thermal diffusivity of the solid is

larger. Also the numerical model which was used to compute temperature and photothermal deflection predicted the experimental results more closely when reflection of the heating laser beam inside the cavity was included. The overall energy coupling between a heating laser beam and a solid is enhanced by a cavity.

Chapter 3 analyzed the unsteady vaporization of a metal target due to nanosecond pulsed laser heating with an ambient gas at finite pressure utilizing a numerical model. A one dimensional thermal evaporation model was employed for target heating with a detailed description of the vapor motion inside the Knudsen layer. The thermal model was applied to the laser heating of metals with a power density below the plasma formation regime. One dimensional compressible flow equations for inviscid fluid were solved to investigate the gasdynamic flow of the vapor with the reflection boundary condition. The results include; i) The efficiency of laser energy coupling with the target is highly dependent upon the target surface reflectivity. ii) The threshold laser fluence predicted with thermal modeling becomes much larger than the values obtained experimentally. iii) The vapor velocity at the edge of the Knudsen layer becomes sonic from the beginning of evaporation only when the ambient pressure is sufficiently small. For large ambient pressures, the vapor velocity varies during the early period of evaporation. The assumption that vapor velocity at the Knudsen layer is equal to the local sound velocity from zero time is found to be valid only for low ambient pressures. iv) The velocity of the vapor leaving the Knudsen layer is less than the local sound velocity when the laser fluence is too small, i.e. the Chapman-Jouguet condition is not satisfied.

Chapter 4 discussed the dynamics of the plume generated by excimer laser heating of aluminum target. The probe beam deflection technique was employed to determine the time-of-propagation of the shock wave and the material plume. The time-of-propagation of the laser induced shock wave was investigated with respect to laser pulse energy, ambient pressure, and the propagation distance of the shock wave. The conditions at which the measured time-of-propagation of the laser generated shock wave is consistent with the theoretically predicted behavior were obtained. The results are summarized as; i) The propagation of the laser induced shock wave near the target surface is planar rather than spherical for a relatively large laser spot size. ii) The parameters that determine whether the time-of-propagation of a laser induced shock wave is consistent with the propagation predicted from an ideal blast wave solution are the small ambient pressure and the small laser spot size. iii) The similarity solution of an ideal blast wave overpredicts the laser energy coupled to the laser induced blast wave. iv) The propagation of the gaseous material plume is observed from the deflection of the probe beam at later times. The propagation velocity of aluminum plume decreases from about 40 m/s near the target to about 20 m/s at a distance of 2 mm from the target. The density of the material plume is expected to be about 0.28-0.45 times smaller than the air density at atmospheric pressure. v) The threshold laser power density for damage for a sanded surface is approximately 1.0×10^{8} W/cm^{2} or smaller.

Owing to the advances in laser technology, lasers with various wavelengths and beam energies became currently available at relatively lower costs. High power pulsed

lasers such as excimer lasers and Nd-YAG lasers are especially interesting because with these lasers a great improvement in manufacturing processes may be possible. For example, a focused laser beam whose diameter can be as small as a few micrometers may enable to overcome the size limit of conventional techniques in microelectronics manufacturing or micromachining processes. Laser materials processing includes no mechanical contact with samples which possibly results in a damage of delicate materials. Also laser material processing is clean, fast, and highly repeatable.

With the increase of laser applications in manufacturing processes, the ability to accurately control these processes is highly required. A thorough understanding of the fundamental mechanisms in laser-material interactions is necessary to achieve accurate control of these laser material processings. Unlike the fast development of laser hardwares, the progress in understanding the fundamental mechanisms during laser-material interactions is rather slow. The extremely small characteristic time and length scales in laser-material interactions are the major obstacles to obtain reliable and consistent experimental data. Theoretical modelings of the laser-material interactions are often limited by the lack of available data for optical and thermal properties of materials at elevated temperatures. To advance the knowledge for laser-material interactions, quantitative measurement of these properties at different wavelengths of laser light is strongly required. To improve the theoretical description of the laser-material interactions, development of mathematical models for non-thermal mechanisms responsible for material removal from the target is also desired.

Appendix

Deflection of a single ray of light in a continuously changing refractive index field

When a ray of light is traveling through a field where the index of refraction varies continuously, the path of the light progressively changes from its original direction as shown in Fig. A1. The deflection of the light will comply with the following rules [1];

i) The light ray deflects towards regions of higher refractive index

ii) The relevant quantity is the rate of change of refractive index with distance

iii) Only the component of the refractive index gradient perpendicular to the ray, dn/dR where n is the refractive index of the medium and R is the radius of curvature of the light path, is operative

The radius of curvature of the light path can be represented in terms of the refractive index of the medium as

$$\frac{1}{R} = -\frac{1}{n}\frac{dn}{dR} \qquad \text{(A1)}$$

where $R=ds/d\theta$ and s is the path of the light ray and θ is the angle between the original direction and the new direction of the ray. In the Cartesian coordinate system, the radius of curvature of the beam path can be written as

$$R = \frac{\left[1+(dy/dx)^2\right]^{\frac{3}{2}}}{d^2y/dx^2} \qquad \text{(A2)}$$

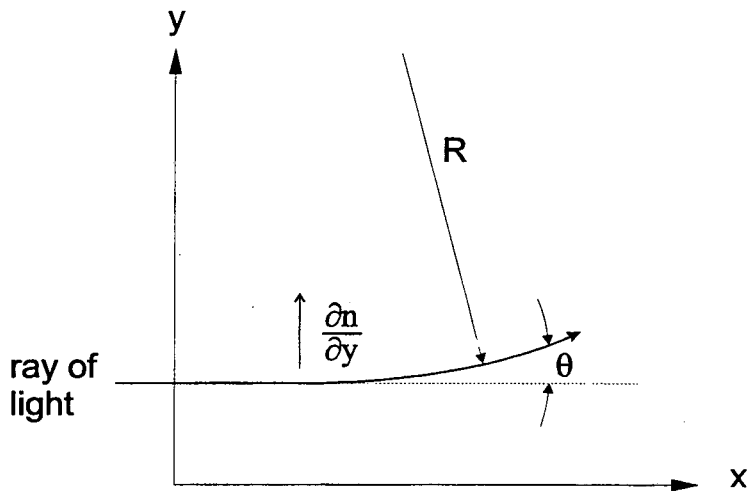

Fig. A.1 Schematic diagram of the deflection of a ray of light in a continuously changing index of refraction field

Also since $dn/dR=(-\cos\theta)dn/dy$, Eq. (A1) can be rewritten as

$$\frac{d^2y/dx^2}{\left[1+(dy/dx)^2\right]^{\frac{3}{2}}}=\frac{\cos\theta}{n}\frac{dn}{dy} \qquad \text{(A3)}$$

For a very small deflection angle θ, $\theta\approx\tan\theta=dy/dx$ and $\cos\theta\approx1$. Therefore Eq. (A3) becomes

$$\frac{d^2y}{dx^2}=\frac{1}{n}\frac{dn}{dy} \qquad \text{(A4)}$$

Assuming that the total deflection of the light ray remains small to allow that the integration of Eq. (A4) over its path can be approximated by the integration over the x axis, we can find the total deflection of the ray of light in the refractive index field by the following equation;

$$\phi = \left.\frac{dy}{dx}\right|_0^x = \int_0^x \frac{1}{n}\frac{dn}{dy}dx \qquad \text{(A5)}$$

If the deflection of the ray of light is solely due to a temperature gradient in the field, Eq. (A5) can be rewritten in the following form;

$$\phi = \frac{1}{n}\frac{dn}{dT}\int_0^x \frac{dT}{dy}dx \qquad \text{(A6)}$$

where T is the temperature of the medium.

References

[1] F. J. Weinberg, *Optics of flames*, 1963, Butterworths, London

Ernest Orlando Lawrence Berkeley National Laboratory
One Cyclotron Road | Berkeley, California 94720

Prepared for the U.S. Department of Energy under Contract No. DE-AC03-76SF00098